DOKUZ EYLÜL UNIVERSITY

GRADUATE SCHOOL OF NATURAL AND APPLIED SCIENCES

FASTENING SOLUTIONS FOR COMPOSITE STRUCTURES

by

Emre ERBİL

November, 2023

İZMİR

FASTENING SOLUTIONS FOR COMPOSITE STRUCTURES

A Thesis Submitted to the
Graduate School of Natural and Applied Sciences of Dokuz Eylül University
In Partial Fulfillment of the Requirements for the Degree of Doctor of Philosophy in Department of Mechanical Engineering, Mechanics Program

by
Emre ERBİL

November, 2023
İZMİR

Ph.D. THESIS EXAMINATION RESULT FORM

We have read the thesis entitled **"FASTENING SOLUTIONS FOR COMPOSITE STRUCTURES"** completed by **EMRE ERBİL** under supervision of **PROF.DR. RAMAZAN KARAKUZU** and we certify that in our opinion it is fully adequate, in scope and in quality, as a thesis for the degree of Doctor of Philosophy.

Prof.Dr. Ramazan KARAKUZU

Supervisor

Prof. Dr. Yusuf ARMAN

Thesis Committee Member

Assist. Prof. Dr. Bahadır UYULGAN

Thesis Committee Member

Prof. Dr. Hasan YILDIZ

Examining Committee Member

Prof. Dr. Buket OKUTAN BABA

Examining Committee Member

Prof. Dr. Okan FISTIKOĞLU

Director

Graduate School of Natural and Applied Sciences

ACKNOWLEDGMENT

First, I would like to express my gratitude to my graduate thesis advisor, Prof. Dr. Ramazan KARAKUZU, whose support, advice, and encouragement helped me overcome challenges during my studies.

The simulation studies in this Thesis use Hexagon MI/MSC Software Marc finite element program. Hexagon MI, BIAS Muhendislik (Türkiye), and especially the Deputy General Manager of BIAS Muhendislik, Mr. Ender KOC, are acknowledged for providing the Marc Finite Element software.

Finally, I would like to thank my beloved family: my father, Feridun ERBİL; my mother, Sabriye Şükran ERBİL; my sister, Ebru DEĞİRMENCİ; my aunties, Faden Suzan & Şefika Türkan KUDSİOĞLU and my beloved friends for their continuous support, patience, and encouragement through all my life.

Emre ERBİL

FASTENING SOLUTIONS FOR COMPOSITE STRUCTURES

ABSTRACT

Lightweight composite materials are continuously improving and have applications in almost every technology field, from rocket science to everyday household appliances. There are many opportunities from the design, performance, operability, and reliability standpoints. Besides these opportunities, challenging topics are open for improvement, especially in securely joining composite parts. Conventional fastening systems like rivets, welding bolts, and clinched fixings were commonly designed for sheet metals or thick construction parts, which may often be incompatible with composites or require additional work when applied to the composite materials. On the other hand, embedding fasteners into composite materials requires molding to adapt to the fastener geometry, which can provide a seamless connection between the assembly components. However, embedding unfamiliar parts may lead to design compatibility issues and inefficient processes in real-life scenarios.

In this thesis, a method was researched and analyzed to improve the load-carrying capacity of single-lap composite structures using a sleeve geometry designed to be formed by a special bolt in the assembly field. The proposed model reduced the failure indices by 16% to 54%, reducing the clamp loss ratio by 18%, and improved the damage initiation force by 8% to 40% compared to similar alternatives. The bearing response and the bearing stiffness were significantly increased with this thesis.

Keywords: Laminated composite plates, carbon fibers, finite element analysis, progressive damage, ductile damage, structural damage, single-lap, sheet-metal, bolted joint

KOMPOZİT YAPILAR İÇİN BAĞLANTI ÇÖZÜMLERİ

ÖZ

Hafif kompozit malzemeler sürekli gelişmektedir ve roket biliminden günlük ev aletlerine kadar teknolojinin hemen hemen her alanında uygulamaları vardır. Tasarım, performans, işletme ve güvenilirlik açısından önemli ölçüde fırsatlar bulunmaktadır. Bu fırsatların yanı sıra, özellikle kompozit parçaların güvenli bir şekilde birleştirilmesi alanında gelişime açık, zorlu konular da vardır. Perçinler, kaynak cıvataları ve zımbalanarak birleştirilen cıvatalar gibi geleneksel sabitleme sistemleri genellikle kompozitlerle uyumsuz olabilen veya kompozit malzemelere uygulandığında ek çalışma gerektirebilecek sac metaller veya kalın yapı parçaları için tasarlanmıştır. Öte yandan, bağlantı elemanlarının kompozit malzemelere gömülmesi, montaj bileşenleri arasında kesintisiz bir bağlantı sağlarken, bağlantı elemanı geometrisine uygun kalıplama işlemini gerektiren bir yöntemdir. Ancak, farklı türden parçaların kompozit yapıya gömülmesi tasarım uyumluluğu sorunlarına yol açabilir ve uygulama süreçlerinde verimsizliğe neden olabilir.

Bu tezde, montaj alanında özel bir cıvata ile şekillendirilmek üzere tasarlanmış bir manşon geometrisi kullanılarak tek katlı kompozit yapıların yük taşıma kapasitesini artıracak bir yöntem araştırılmış ve analiz edilmiştir. Önerilen model, hasar endekslerini %16 ile %54 oranında azaltmış, kilitleme yükü kayıp oranını %18 azaltmış ve benzer alternatiflerle karşılaştırıldığında hasar başlama kuvvetini %8 ile %40 oranında arttırmıştır. Bu tez ile rulman tepkisi ve rulman rijitliği önemli ölçüde arttırılmıştır.

Anahtar kelimeler: Tabakalı kompozit levhalar, karbon lifler, sonlu elemanlar analizi, kademeli hasar, sünek hasar, yapısal hasar, tek-bindirme, saç metal, cıvatalı bağlantı

CONTENTS

Page

LIST OF FIGURES

Page

LIST OF TABLES

Page

CHAPTER ONE
INTRODUCTION

Composite structures have several advantages as they combine the strengths of the various compounds that form themselves. They are strong, powerful, lightweight, and durable, depending on their composition. Lightweight composite materials are continuously improving and have applications in almost every technology field, from rocket science to everyday household appliances. There are many opportunities from the design, performance, operability, and reliability standpoints. Besides these opportunities, there are also challenging topics open for improvement. The cost of production, maintenance, and operation are higher and must be considered, especially for future maintenance. From a design point of view, there are also challenging topics that need to be improved, especially in securely joining or fastening composite parts. Three common types of joints are used in the industry: mechanically fastened, adhesively bonded, and hybrid (mechanical and bonded) joints. Conventional mechanical fastening systems like rivets, welding bolts, and clinched fixings were commonly designed for sheet metals or thick construction parts, which may often be incompatible with composites or require additional work when applied to the composite materials. They can generate stress concentration fields in the assembly and can cause corrosion in the assembly. On the other hand, adhesive joints can be more efficient than mechanical connections when the objective is to reduce the overall weight of the assembly. Adhesive methods can reduce the stress concentration effect by filling the physical gap between the corresponding parts in the assembly. However, this method requires precise production of adjacent faces with minimal tolerances. From the design standpoint, the non-uniform stress distribution can cause debonding in the bonding zone, where the maximum stress is dependent on the pattern of the bonded area in the joint, the thickness of the adhesive, bonding length, geometry of the joint, unbalanced adherend stiffness, the material type of composite adherents, and the adhesive response. On the other hand, hybrid-type joints consist of multiple material types in a combination of bonded and mechanically fastened joints. This connection is preferred in the aerospace industry for joining two or more different materials, like joining a metallic bolt to a composite part. For instance, embedding fasteners into composite materials requires molding to adapt to the fastener geometry,

which can provide a seamless connection between the assembly components. Integrating the composite manufacturing process with the fasteners (bolts, nuts, studs, etc.) can provide a secure and integral solution to the assembly. Various design and material combinations and plastics with metals and composites can be used. For example, a fastener unsuitable for composites can be used in the assembly. However, embedding unfamiliar parts may lead to design compatibility issues and result in inefficient processes in real-life scenarios, like weakening the composite product or increasing the thickness or weight. Similarly, the maintenance and repairability of the connection could be significantly complex and would have higher costs depending on the complexity of the assembly parts. Moreover, the interchangeability can drastically be affected and cause significant complicacy in the worst-case scenario.

Bolted joints are the most simple and reliable methods in mechanical-type joints. They are usually interchangeable, easy to mount, easy to maintain, and they have lower costs when compared with the other methods. However, there are significant challenges, especially in assembling fiber-reinforced composite parts. In a single or double-lap configuration, the composite plates are susceptible to the loads in the thickness direction where the clamping load was applied. Viscoelastic relaxation defines how much clamp load would remain in the joint depending on the mechanical boundary conditions and the preload applied. Secondary bending moment generates non-homogeneous stress distribution around the clamping area. Matrix damage occurs once the clamping load reaches the threshold value, or the secondary bending causes excessive transverse stress over the matrix and the fiber material. The fiber-matrix damage and, finally, the fiber damage results in catastrophic plate damage if the loading conditions are not properly set. On the other hand, vibration is a critical effect triggering the loosening process, resulting in the loss of clamp load in time. There are several mechanisms to eliminate or reduce the adverse impact of lateral vibrations in a bolted joint. Some of them require additional elements in the assembly, like washers, pins, and some chemical adhesives. The special washers and sometimes the bolt or the nut may have unique geometric properties like serrations to ensure geometrical locking conditions under vibrational loads. The special nuts have micro-fiber parts between the threads to compensate for micro-slips between the bolt and the nut. Similarly,

special pins can help lock the bolt and the nut, geometrically guaranteeing relative motion between the adjacent thread surfaces of the bolt and the nut.

In essence, there is no perfect joint in the industry. There are always drawbacks in design depending on the service conditions of the joint. Therefore, the method's benefits must be evaluated wisely regarding design, production, assembly, and service life.

1.1 Purpose & Scope

As discussed in the section above, there are alternatives for joining two single-lap composites. In this study, the purpose is to develop a new method using simple mechanical components to improve the durability of the joint by increasing the lateral load-carrying capability and to improve the clamp load limits by adding a sheet metal component to the assembly. The assembly component above is the sleeve material defined as a sheet metal object that can be deformed plastically during the assembly process without harming the corresponding assembly parts. MSC Marc/Mentat finite elements analysis software package is used in the mechanical analyses. A significant improvement was achieved in the durability and reliability of the joint. The loss of clamp load is significantly reduced, and the effect of secondary bending moment is also reduced.

The method was applied to a single-lap composite joint. However, this method can also be applied to combinations like single-lap to metal, double-lap to metal, single-lap to single-lap, or double-lap to single-lap composite joints. The alternatives can be increased depending on the assembly scenario.

1.2 State of the art

Bonded, mechanical, and hybrid connection technologies for composite materials are continuously advancing in several industries. One of the most common methods was using chemical adhesives to bond unfamiliar components.

Figure 1.1 Adhesively bolted connections, a) embedded, b) surface bonded, c) lean bonding (bigHead, 2023)

Three forms of use cases are shown in Figure 1.1. The embedding-type connection can provide impressive durability by carrying extreme loads compared to the composite's wall thickness. However, the process must be explicitly designed for this fastener, and it could be hard to maintain in service conditions.

In surface bonded configuration, any surface can support bolts and nuts without drilling the main body. It could be efficient, especially for thin-walled composites. However, the maintenance capability might be significantly reduced because of the chemicals applied to the surface. The lean bonding connection was a different surface-bonded connection, claiming that the joint could be used 10 seconds after the application.

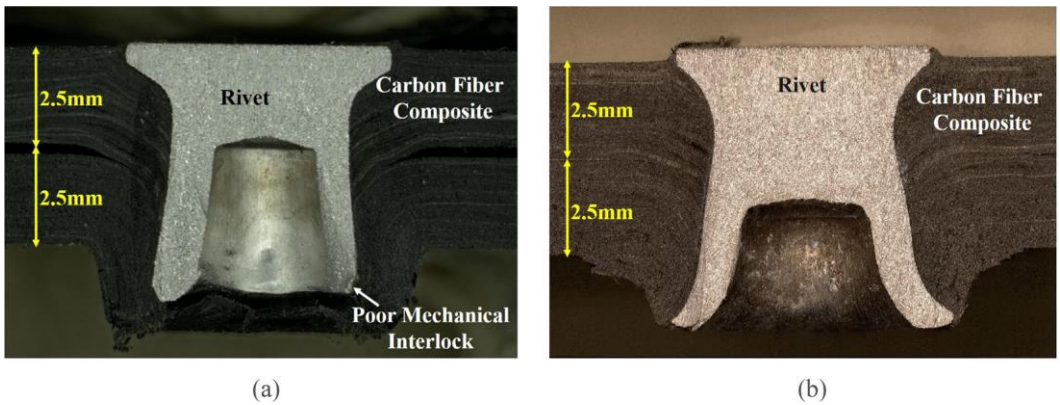

Figure 1.2 Self-piercing riveting method, a) self-piercing rivet, b) self-piercing-through riveting (Rao et al., 2020)

The mechanical joining methods were studied by (Rao et al., 2020). This method could be feasible for thick-walled composite parts.

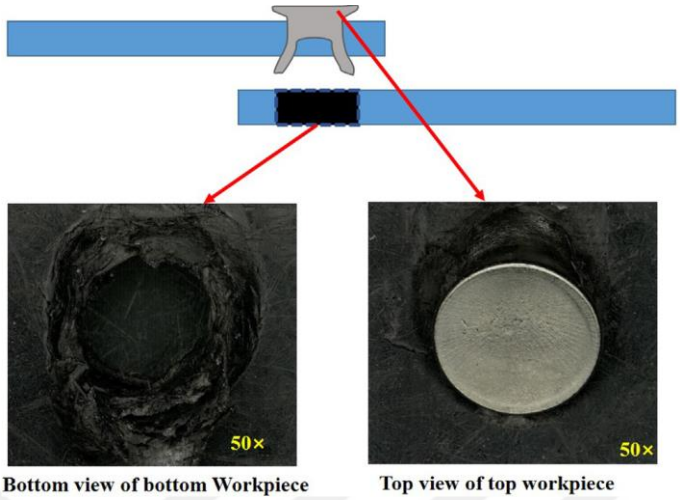

Figure 1.3 Damage around the deformation zone in the self-piercing riveting method (Rao et al., 2020)

However, this would not be beneficial for thin-walled composites because of the severe damage around the assembly region, as seen in Figure 1.2 and Figure 1.3.

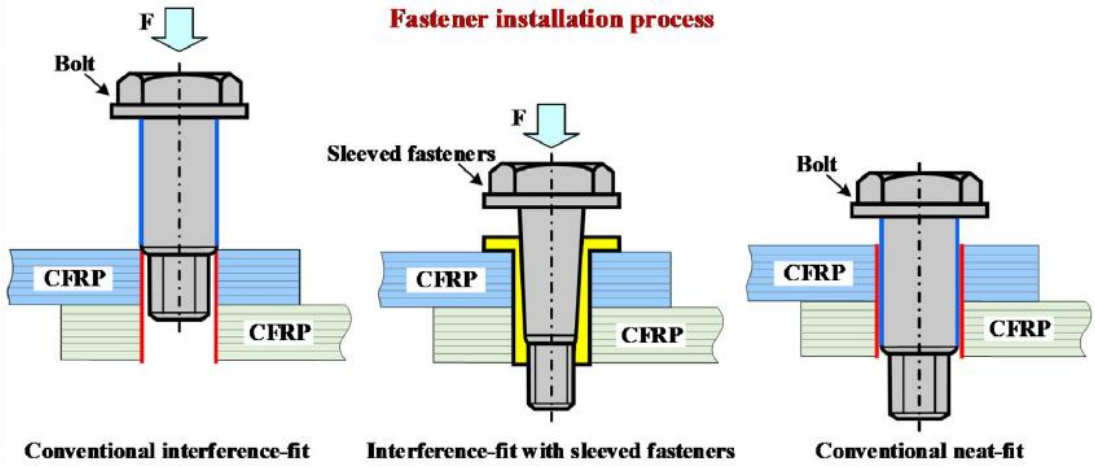

Figure 1.4 Sleeved bolted joint assembly process for single-lap composites (Xu et al., 2022)

(Xu et al., 2022) studied conical sleeve geometry with a bolt having conical shank geometry corresponding to the sleeve surface (Figure 1.4).

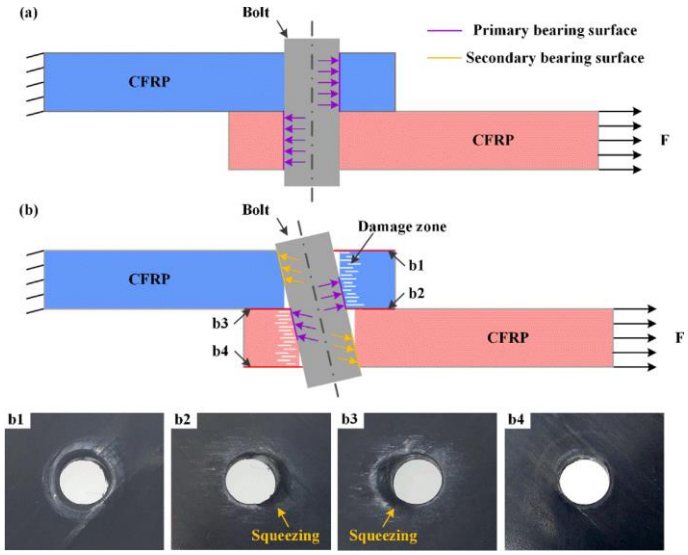

Figure 1.5 Primary and secondary bending (a) before the lateral pulling, (b) after the lateral pulling, (b2-3) surface damage caused by secondary bending (Xu et al., 2022)

The experiments in a study by (Xu et al., 2022) reveal the damaging effect of the secondary bending moment in Figure 1.5.

(Akbarpour & Hallström, 2020) was studied on bolted joints with and without sleeves. They improved the load carrying capacity by 55% using insert in the assembly.

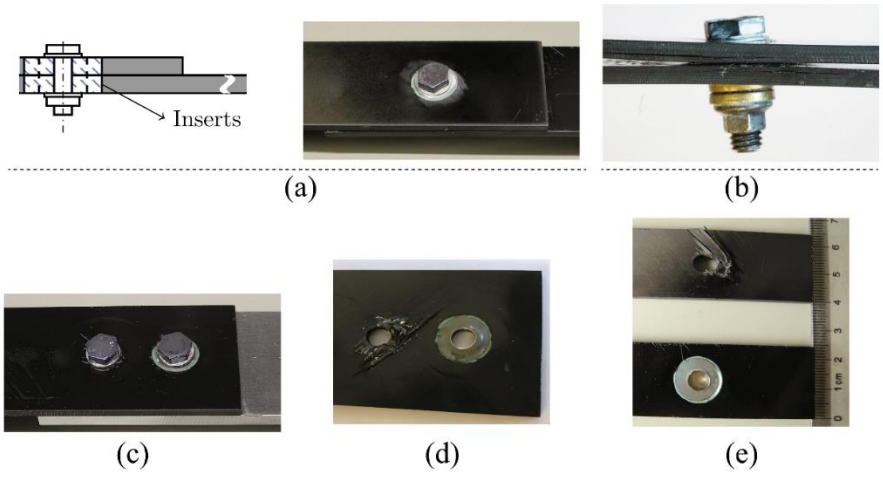

Figure 1.6 (a) Single-lap composite bolted joint with inserts, (b) damaging layers under secondary bending moment, (c) single lap, double-bolted joint, one with insert, another without insert, (d) open-hole tensile damage with/without insert (Akbarpour & Hallström, 2020)

No net shape failure was observed in their study. Fiber damage was depicted in the Figure 1.6-d.

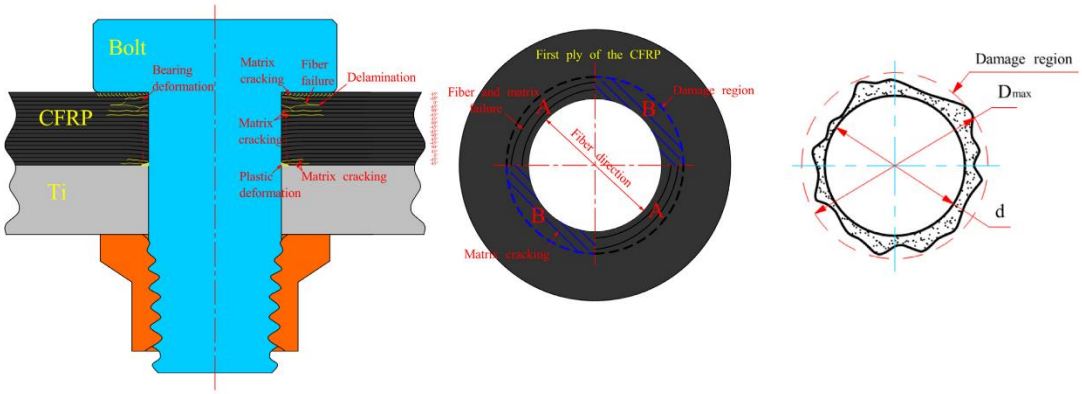

Figure 1.7 (a) Single-lap composite bolted joint, (b) bearing surface damage, (c) bearing damage region (Zuo et al., 2020)

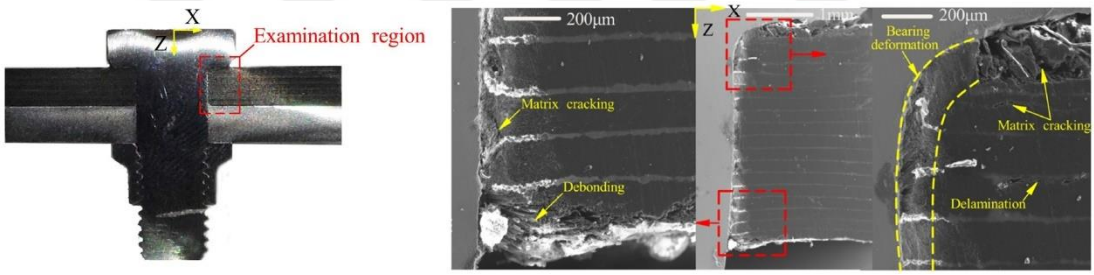

Figure 1.8 Composite damage in single-lap sleeveless bolted joint configuration (Zuo et al., 2020).

(Zuo et al., 2020) revealed the bearing deformation in Figure 1.7 and detailed the deformation zone under an electron microscope in Figure 1.8, classifying the deformation types successfully.

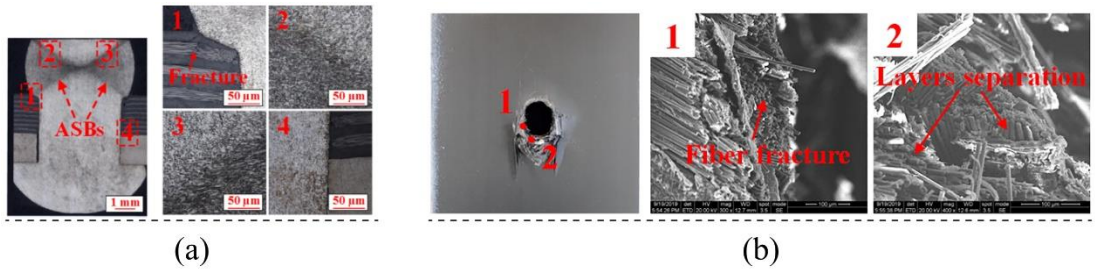

Figure 1.9 (a) Composite damage zone after riveting, (b) microscopic inspection of damage zone (Jiang et al., 2021)

(Jiang et al., 2021) tested CFRP and Al parts in a single-lap configuration, including joining by riveting and pulling in the longitudinal direction. The results show in Figure 1.9 that bulk-forming over a composite part may cause failure in the neighboring composite components.

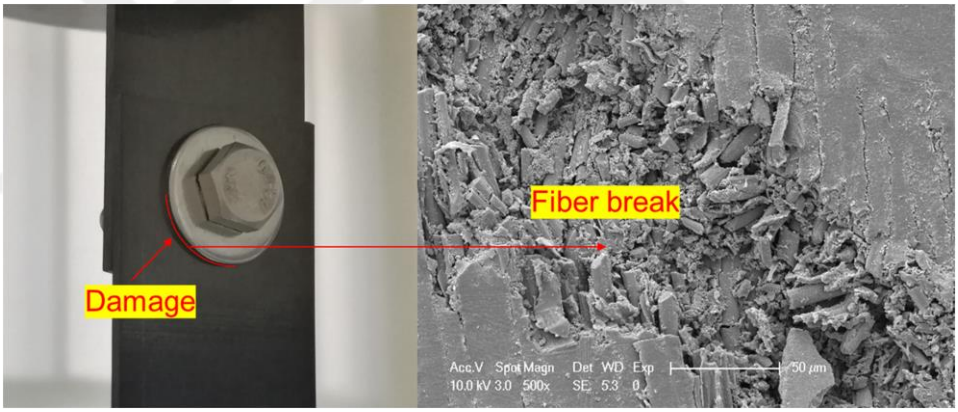

Figure 1.10 (a) Surface (fiber) damage due to excessive torque (Zhang et al., 2019)

(Zhang et al., 2019) investigated the worn-out zone under SEM on the adjacent surface with the washer and the composite surfaces (Figure 1.10), in which the damage was induced by excessive clamping torque.

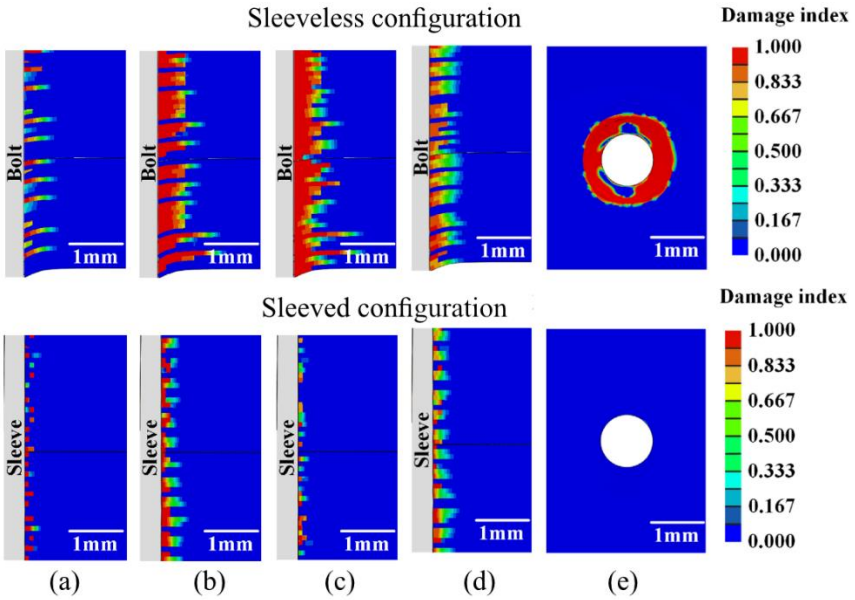

Figure 1.11 (a) Fiber failure (comp), (b) matrix failure (in-plane, comp), (c) matrix failure (out-of-plane, comp), (d) fiber-matrix shear, (e) delamination (Xu et al., 2020)

In the aerospace industry, interference-fit is gaining more attention due to its ability to improve the sealing and fatigue life of composite assemblies. However, a major challenge still remains which is the significant damage caused during installation around the hole. (Xu et al., 2020) studied on a three-dimensional anisotropic non-linear progressive damage model based on continuum damage mechanics. They revealed (

Figure 1.11) that using a sleeve can drastically reduce damage near the bolt hole and the bolt seating surface.

1.3 Previous Studies

The goal is to achieve the capability of bolted joints. However, the proposed model will be applied to a single-lap composite plate. Therefore, the literature survey was focused on the analysis procedure and the physical parameters of the joint to obtain a representative model for the numerical analyses. (Collings, 1982) experimentally revealed that tightening the bolt can provide lateral constraint where the bolt can help suppress the swelling of laminate material at the hole edge and eliminate brooming-

like premature failure. (McCarthy et al., 2002) studied the effect of bolt-hole clearance on the stiffness and strength of single-lap, single-bolted CFRP composite joints, points out that from neat fit to a certain level of clearance improves the bearing strength. However, bearing strength significantly drops down after that level. This is explained by the mechanism of failure, where the progressive damage can cause an accumulation of damaged particles around the fastener shaft. The improvement occurs when the accumulated damaged particles increase the contact area at a certain level. The joints from loose to tight-fitting configurations in the range of four tolerance degrees and two torque levels for two different head types, countersunk and protruding, were tested. As the study was focused on the aerospace industry, half of the clearance was chosen inside, and the other half was outside the aerospace tolerances. It was claimed that since the friction type was changing from static to kinetic due to the slippage, the loading pattern was changing in the protruding-head configuration. There is a relation between clearance and bearing strength in protruding-head configuration for both low-tightening and non-tightening conditions where the bearing strength decreases when the clearance increases. According to the experimental studies, the clearance effect is insignificant when the proper tightening torque is applied to the fastener. Additionally, the negative effect of clearance is so small if it is between the aerospace-standard limits. (Virupaksha & Nassar, 2008) studied the effect of preload and washer thickness for double-lap configuration, the researchers observed that bolt preload does not affect ultimate joint strength. However, it was clear to say that bearing strength increases progressively by bolt preload. Washers are the fundamental assembly elements used to have several advantages from a design perspective. It was observed that the washer size was effective in damage results, where the small washers caused more damage than the larger ones. That was the effect of the contact area generating contact stress. The washer thickness had a neglectable effect on ultimate joint strength and strain. A mathematical model proposed by (Awadhani & Bewoor, 2018) predicts the joint stiffness for single-lap bolted connections. It was observed that the increase in bolt diameter was improving the joint stiffness in unidirectional and bi-directional $[0/90]_S$ specimens. Interestingly, the loading rate significantly affected joint stiffness when the bolt diameter was larger than 6 mm. A review study by (Dawei et al., 2018) on the metal-CFRP hybrid joining process described the joining methods, adhesive bonding,

mechanical fastening, z-pin, welding, and joining by plastic deformation, respectively. The study reveals that joining by plastic deformation can be applied to titanium and niobium alloys, stainless steel, 1-2-5, and 7 series aluminum alloys. Since the FEA does not cover fiber damage or fiber deformations (Dawei et al., 2018), it was found that the hot riveting technique results in less joint stress after the joining process. Therefore, the prevailing stress around the deformation area should be considered when choosing the clinching or join-by-plastic-deformation method. (Yang et al., 2019) studied the use of shimming material between composite plates, and the research team observed that an existing physical gap between composite plates reduces the strength of the structure. On the other hand, filling the gaps with liquid shimming material improves the bending strength. (Yang et al., 2019) the bolt-hole clearance was ineffective against initial stiffness, but the load take-up stiffness. In a study by (Fotouhi et al., 2020), S-glass and IM7-carbon laminate were compared via indention test. It was observed that the glass laminate can resist higher deflections than carbon laminate to failure. However, the overall damage mechanism was the same in both. The methods for characterizing interfacial properties between the fiber and polymer matrix were reviewed. The pinning effect of a bolted composite joint was studied (Ranjan & Pandey, 2021). It was explained that the pinning effect starts when the bolt shank travels to the end of bolt-hole clearance and touches the hole edge. The proposed model is applied to the vibration-loading condition and can predict the pinning force around the hole. A method was developed by (Olmedo et al., 2014) to determine the secondary bending effect on the stiffness of single-lap composite bolted joints. According to this method, the joint stiffness can be improved by increasing the bolt torque, friction coefficient, plate width, and plate thickness. However, reducing the bolt diameter, plate thickness, and width can also decrease the joint stiffness, resulting in a higher secondary bending effect. Since the bolt-hole clearance generates a relative displacement between the shank and the plates, it also increases the secondary bending.

The friction mechanism defines the stress distribution in bolted composite connections. Therefore, it is essential to choose a proper method for numerical analyses. The friction modeling was studied by (McCarthy C. et al., 2005) using the MSC Marc finite element analysis software package to compare the continuous and discontinuous or the ‘Stick-Slip’ models. The discontinuous model matches the

experimental load-deflection curves for net fit and extensive bolt-hole clearance conditions. On the other hand, a continuous model can match the experiments by modifying the “relative sliding velocity” parameter. This parameter represents the maximum relative sliding velocity where the instability begins. According to the study by (McCarthy C. et al., 2005) the coefficient of friction (COF) between the two adjacent laminates was practically recommended between 0.40 and 0.45. It was emphasized in the studies by (McCarthy C. et al., 2005) and (Qiu et al., 2022) that the use of the “Stick-Slip” model in the FE analyses of composite bolted joints can improve the quality of the analyses by getting closer results to the real-life models. Increasing the clamping load improves joint stability. Hence, the coefficient of friction between the under-head surface area and the target surface should be minimized to obtain maximum preload from the fastening torque. In other words, the torque energy is converted into heat by under-head friction and wasted. Therefore, the wasted energy outside the thread region can be minimized by applying chemicals to the under-head surface area. Additionally, the conservation of preload is crucial in a bolted connection. In the study (Friedrich & Hubbertz, 2014) the loss of clamping force takes place immediately after the tightening is over. The loss of clamping force is usually related to the matrix material in a composite structure since important parameters like temperature can change the behavior of the matrix material. CFRP composite plates cannot withstand excessive loads perpendicular to their fiber angles. Tightening the bolts barely and recursively on the composite plate can damage the interior elements of the composite structure. On the other hand, poorly clamped or self-loosened joints can trigger more than one corrosion mechanism. Additionally, wear is another parameter to consider while designing the tightening procedure.

As mentioned above, bolt-hole clearance is an essential factor in composite bolted joints. It was revealed by (Chen et al., 2018) that the interference fit (I-F) reduces the maximum stresses compared to the tolerance fit of G7/h6 and U7/h6. However, according to (Li et al., 2015) I-F can induce failure mechanisms around the interface area. The damage usually starts with micro-voids, resulting in matrix-fiber breakage. It was observed by (Li et al., 2015) that these damaged particles can form a buffer zone to withstand the bearing load. Hence, the I-F improves bearing capacity if the I-F size is optimum. It was emphasized by (Song et al., 2015) that I-F can improve the fatigue

life of the structure. Another study by (Wei et al., 2013) verifies the benefits of a proper I-F that significantly improves fatigue life compared to a neat-fit configuration. However, improper or excessive I-F can decrease the ultimate bearing stress. (Li et al., 2015) recommends the I-F of 2.1 % to obtain the maximum tensile strength for a single-lap CFRP/Ti bolted connection. I-F must be applied wisely to avoid delamination or catastrophic damage caused by overfitting. FE results for various I-F configurations in the study by (Song et al., 2015) should be useful in that manner. Also, an analytical method was proposed by (Wu et al., 2016) to calculate the stress around the I-F region. (Song et al., 2016) revealed that the most sensitive area for I-F was the top surface of the CFRP composite layer. So, adding a metal washer to the entrance of the hole and decreasing the friction should be useful to decrease damage. It was observed by (Hu et al., 2018) that tightening the bolt after I-F should reduce delamination risk and should significantly improve bearing behavior. The study by (Hu et al., 2019) proposed a numerical approach to predict damage mechanisms based on nonlinear continuum damage mechanics. The results showed that the proposed method can properly predict fiber and matrix damage. It was observed by (Hu et al., 2020) that the matrix material softens at higher temperatures, and the joint nearly loses its resistance against external loads above the glass transition temperature. A practical rivet geometry was designed by (Liu et al., 2021) based on the join-by-plastic-deformation method. The design parameters were also optimized for maximum pull-out resistance. An exciting study by (Sajid et al., 2021) investigated the washer's role in decreasing the adverse effects of tolerance-fit configuration. The results showed that using large washers under the bolt head should improve damage resistance by providing less contact stress at the top layer and absorbing more energy caused by external forces. Single-row and staggered-row multi-bolted joints were compared by (Noroozi et al., 2014). It was concluded that the bolt spacing should be increased to avoid net-section failure. Similarly, using a large washer in such configurations may help reduce the damage initiation threshold.

Self-piercing rivets (SPR) are widely used as an alternative to bolted composite connections. An SPR geometry was proposed by (Ueda et al., 2012), which provides a one-shot connection between the two flat washers, resulting in greater joint stiffness when compared with bolted connections. With advanced simulation methods, the

clinching process using the FE method was precisely explained and revealed by (Hirsch et al., 2017). The clinching die (tool) geometry and the clinching process were optimized for metal-composite joints in the studies by (Oudjene et al., 2009), (Lambiase & Ko, 2017), and (Wang et al., 2020). A practical self-piercing-through riveting process was designed for discontinuous carbon fiber-reinforced nylon 6 composite by (Rao et al., 2020). The intra-ply failure was depicted via SEM imaging by (Canal et al., 2012) and the micro-damage mechanism could be seen in a composite structure. There are useful methods explained by (Ekh et al., 2013) and (Nerilli & Vairo, 2017) which can be used for building customized post variables in the FEA for damage visualization. A numerical study by (Choi et al., 2018) predicts failure load for two tightening torque conditions. The study by (Hu et al., 2018) comprising the progressive failure of bolted single-lap joints of woven fiber-reinforced composites, helps understanding the damage mechanism using ABAQUS commercial FEA software. Another study by (Cao et al., 2020) related to the damage progression and failure of single-lap thin-ply laminated composite bolted joints under quasi-static loading gives insights into how damage initiates and progresses and how non-linear softening ignites the catastrophic failure. A comprehensive study by (McCarthy, 2020) covering the design and failure analysis of composite bolted joints for aerospace composites should be considered a good resource for fundamental issues.

A practical study by (Qiu et al., 2022) revealing the material and damage characteristics of HTA7/6376 CFRP material predicted the maximum failure load of a single-bolt, single-lap joint by using the bearing stress and the stress distribution of the sub-laminates.

The definition of contact method and mechanism plays a significant role in the reliability of FE results. The node-to-segment method was first introduced by (Mayer & Gaul, 2007), promising more precise contact results. However, it was experienced that solution time exceeds the old method in some circumstances. A promising 3D FE model based on shell elements was proposed by (Guerrero et al., 2023) including thermal effects that could simulate large models consisting of multiple effects like contact, bolt loads, clearance, etc. An analytical method developed by (Yang et al., 2022) related to a multi-bolt spring mass method predicted the joint stiffness with a

19.8% error rate, while the FE model in this study was 12.4 %. The method could be useful when FE modeling was not possible.

Apart from the references listed above, it could be useful for researchers to review similar studies as mentioned in the text. Similar studies comprising the applications in the composite joining field and in the numerical field including composite and metal damage were published by (Lennon et al., 1999), (Barnes & Pashby, 2000), (Roux & Bouchard,2013), (Mucha, KaŠČÁK & SpiŠÁK, 2011), (Behrens et al., 2014), (Lambiase, 2015), (Han, Chrysanthou, and Young, 2007), (Abe et al., 2014), (He et al., 2015), (Min et al., 2015), (Balawender, Sadowski & Golewski, 2012), (Oudjene & Ben-Ayed, 2008), (Chen et al., 2016), (Neugebauer et al., 2008), (Nong et al., 2003), (Sun & Khaleel, 2005), (Gerstmann & Awiszus, 2014), (Hahn et al., 2014), (He, Pearson & Young, 2008), (Liu & Zhuang, 2019), (Hoang et al., 2010), (Porcaro et al., 2006), (Rispler et al., 2000), (Varis & Lepistö, 2003), (Hirsch et al., 2017), (Liu et al., 2013), (Akterskaia et al., 2019), (Garnich & Akula, 2008), (Tay et al., 2008), (Hühne et al, 2010), (Zhang et al., 2014), (Subramonian et al., 2013), (Rice et al., 1969), (Panicaud et al., 2011), (Stoughton & Yoon, 2011), (Lian, Feng & Münstermann, 2014), (Pommier et al., 2017), (Jasra et al., 2020), (Giannopoulos et al., 2017), (Khashaba et al., 2006), and (Lee et al., 2015).

In this study, a comparative analysis was carried out to understand if additional sleeve(s) can improve the capability of the connection against progressive composite damage. Marc/Mentat FE software was used in the numerical computations. Composite damage was significantly reduced under high clamping load by implementing the concept revealed in this study.

CHAPTER TWO
MATERIAL AND METHODS

This research was carried out in three stages. The first stage consists of the mechanical definitions related to the HTA/6376 CFRP composite material used in the second stage. The contact and friction parameters were defined, and the analysis model was built regarding the study led by (McCarthy M. et al., 2005). The progressive damage model was built using customized Fortran subroutine codes with the Python software development environment in MSC Marc software. In the second stage, the ductile damage parameter was obtained based on the study by (Ben Othmen et al., 2020) for AISI 304L stainless steel material. In the last stage, the proposed final model was built based on the experiences of primitive models and analyzed using the parameters obtained in the first two stages.

2.1 Progressive damage modeling for composite plates

The analyses were carried out in MSC Marc/Mentat finite elements software. Fortran and Python interpreters were used in the pre and postprocessing stages. Fortran subroutines were compiled as an executable file programmed to run simultaneously with the Marc main executables.

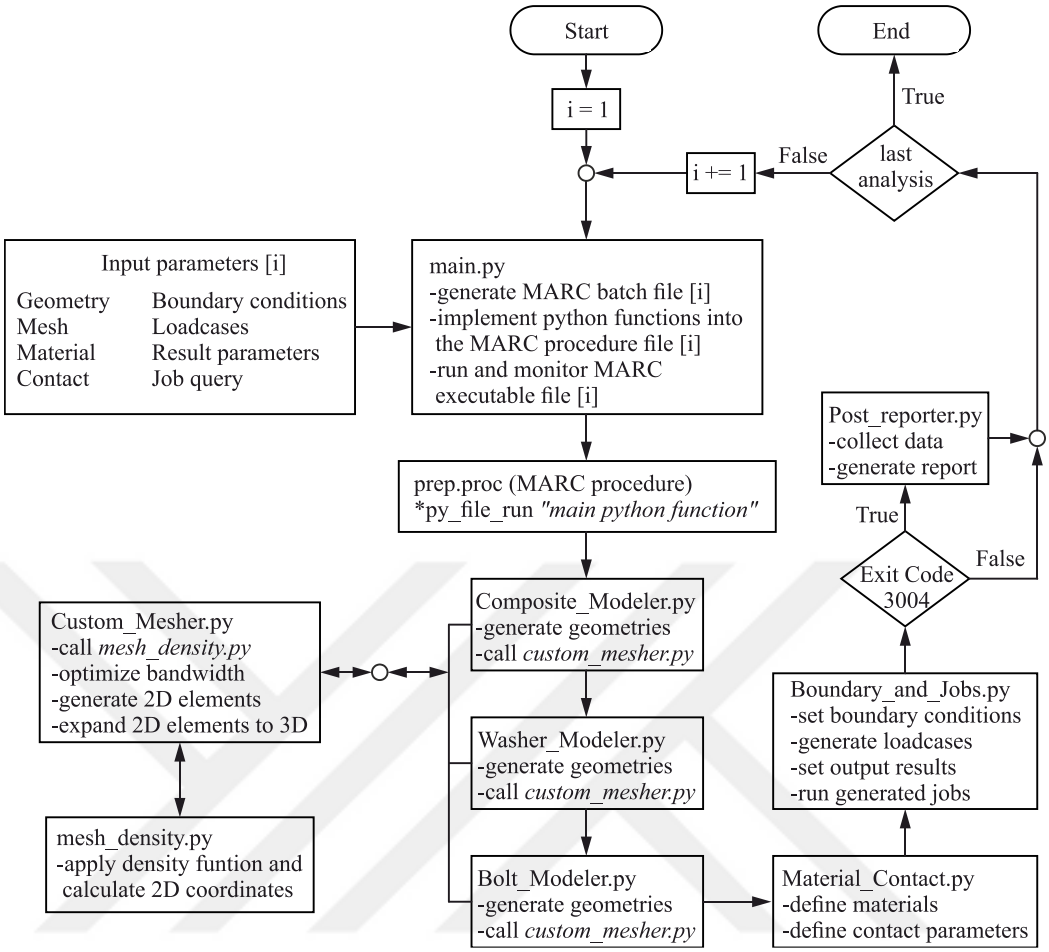

Figure 2.1 Python pre/post processor code flow chart

According to the flow chart given in Figure 2.1, the code structure was designed to run every execution cycle to compute parametric batch analysis series. The main program in the Python virtual machine was set to listen to the ports opened by Marc's executable and initiate the serial analysis when the submitted analysis was finished. Input parameters of the model were stored in a separate Python function to be executed when triggered. A fully customized mesher algorithm was developed in Python and embedded in the modeler code written for the present study. The finite element mesh was refined and optimized for composite parts according to the density function. Node and element numbers were stored in a reference file before the Marc job(s) submission for further operations like post-processing.

The nonlinear shear behavior of the composite material was embedded in the material model and linked to the damage model by a set of codes in multiple routines.

A numerical study supported by experimental results comprising a 3-D finite elements (FE) analysis of single-lap bolted joint by (McCarthy M. et al., 2005) was selected for verification. The FE model was generated related to the (McCarthy M. et al., 2005a, 2005b). The mesh algorithm was designed according to the model exposed by (Ireman, 1998). The method was implemented in Python by adding control parameters during the mesh generation process. Therefore, the default mesh algorithm in Marc was not used in the analyses.

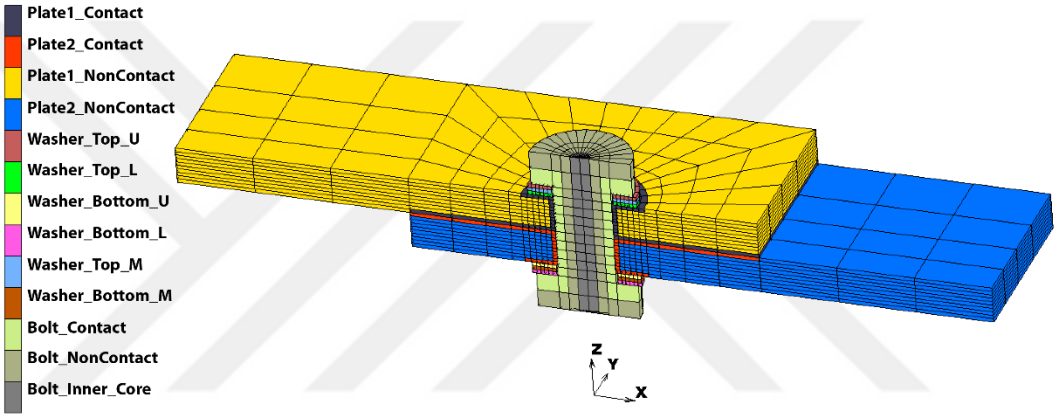

Figure 2.2 FE model revealing the contact element groups

The target surface was laid and seeded for 2D quad meshing, then expanded to the 3-D hex geometry individually in Python. The FE model is given in Figure 2.2.

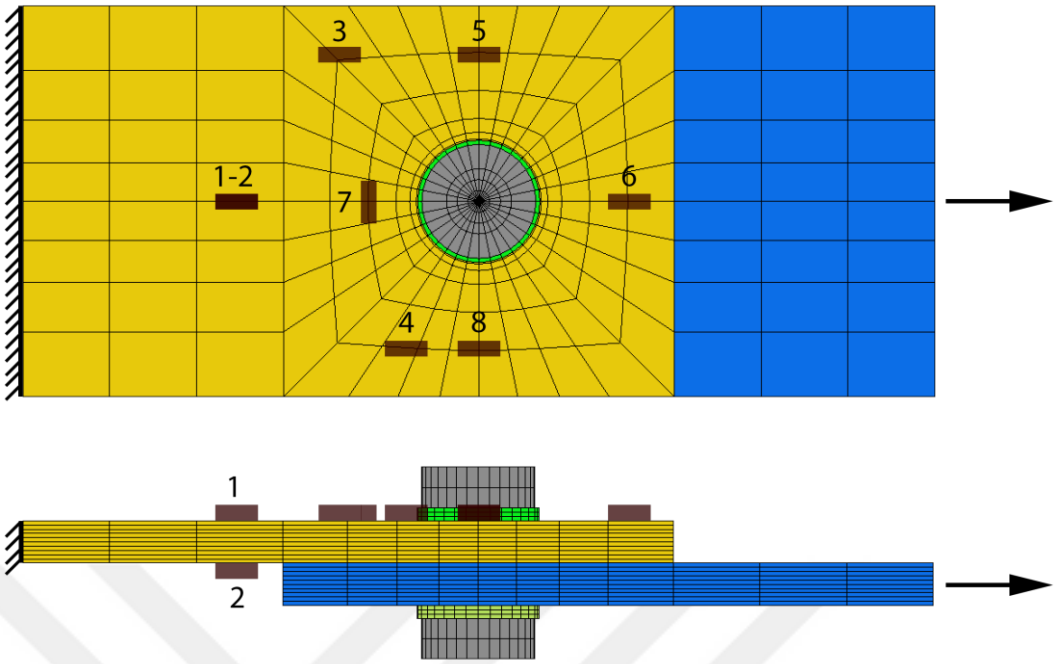

Figure 2.3 Gage locations with boundaries

The top plate is fixed at the end, and the bottom plate is pulled to 5 kN of force, gradually in the longitudinal direction, as shown with an arrow in Figure 2.3. Load and strains were read by stain gages bonded to the material, as given in Figure 2.3.

The geometrical ratios applied to the plates were w/d=6, e/d=3, d/t=1.54, where w, e, d, and t represented the plate width, distance from the bolt axis to the plate edge, the bolt hole diameter, and the plate thickness, respectively.HTA/6376 lay-up (quasi-isotropic) was used in the stacking sequence of $[45/0/-45/90]_{5s}$. The total laminate thickness was 5.2 mm after curing, and each ply had a nominal thickness of 0.13 mm. Bolt hole diameter, the washer thickness, the inner and outer diameters of the washer are 8 mm, 1.6 mm, 15 mm, and 8.4 mm, respectively. Parts were analyzed in two clearance configurations, C1=0 µm, and C4=240 µm, to verify with the literature. Bolt torque was set to 0.5 Nmm (finger-tight), providing 360 N of preload and producing 7.2 MPa of prestress over the bolt, aligning with the source study by (McCarthy M. et al., 2005). The thermal expansion coefficient of the washer was defined in the thickness direction only. Bolt and nut are merged into one geometry for the analysis. As an initial condition, external heat was applied to the nodes of the washer on top.

The purpose was to expand the bolt in the thickness direction to produce a thermally prestressed condition. The von Mises yield option was activated for elastic elements to limit the stresses not to exceed a maximum limit.

Table 2.1 Stiffness properties of materials (McCarthy M. et al., 2005) (temperature-dependent experimental data from Marc internal material database)

Unidirectional HTA/6376						Steel washers					
	GPa		GPa				GPa		GPa		
	E_{11}	140.0	G_{12}	5.2	ν_{12} 0.3		190			ν_{12}	
	E_{22}	10.0	G_{13}	5.2	ν_{13} 0.3	E	190	G	79.3	ν_{13}	0.3
	E_{33}	10.0	G_{23}	3.9	ν_{23} 0.5		190			ν_{23}	

Material specifications are given in Table 2.1. It was aimed to verify a proper friction model representing experimental conditions as closely as possible. In a study by (McCarthy C. et al., 2005) the "Stick-Slip" (Coulomb) and "Continuous" friction models were compared, and it was found that the "Stick-Slip" friction model represents the friction conditions better than the continuous model. According to the study's results by (McCarthy C. et al., 2005), the use of low friction coefficient between the laminate-laminate interface converges to the experiments. Regarding that, the kinetic coefficient of friction for washer-laminate, bolt-laminate, and laminate-laminate are chosen as 0.3, 0.1, and 0.42, respectively.

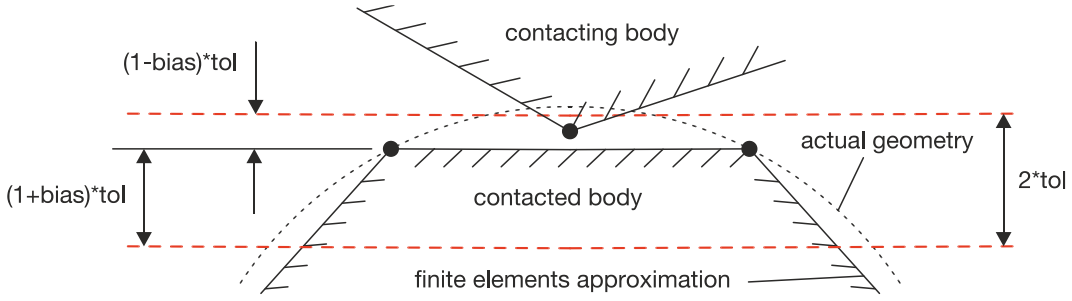

Figure 2.4 Contact bias parameters

α, β, and e are the control parameters representing the friction coefficient multiplier ($\mu_{static}/\mu_{kinetic}$), slip-to-stick transition region distance, and the convergence tolerance of friction force, respectively. The analyses took these parameters as α=1, $\beta=10^{-4,}$ and

e=0.1. The single-sided contact method is used for computing the contact that was explained in Figure 2.4. The overall contact tolerance was taken as 0.01, and the contact bias was taken as 0.9. Outside and inside contact tolerances are taken as (1-0.9)x0.01=0.001 and (1+0.9)x0.01=0.019, respectively. Contact bias parameters should be defined carefully because the correct bias can reduce the tendency toward splitting the increments. This is the convergence method, driven by the FE algorithm, when the node in the contacting body penetrates the contacted body by exceeding the tolerance value.

The "Segment-To-Segment" contact method might be used over the "Node-To-Segment." In general, the segment-to-segment method converges faster than the node-to-segment method. However, the segment-to-segment method produced nonconforming results in our case. Therefore, the node-to-segment method was used in the analyses in conjunction with the study by (McCarthy C. et al., 2005).

The continuous surface representation for 2D curves and 3D surfaces was activated in the FE software to prevent random penetrations caused by the use of discrete elements. Discrete elements can generate nonhomogeneous stress/strain distribution when another element penetrates the node, resulting in convergence issues and low-quality results. Therefore, the smooth boundary option and the C^0 Continuity parameter were activated for contact bodies. Quadratic and linear segments were replaced by coons' surfaces with this option.

An eight-node 3D composite brick element, type-149, which has 3 degrees of freedom (DOF) per node, was chosen for composite bodies. Element 149 has four integration points on each layer, representing up to 510 layers in an element. In this case, there are 20 layers exist, and each layer consists of 4 stacked laminas. There are 17200 elements in each laminate and 11440 nodes per laminate. A total of 34400 elements and 22880 nodes are used in the analyses. The minimum edge length of an element was 0.15 mm.

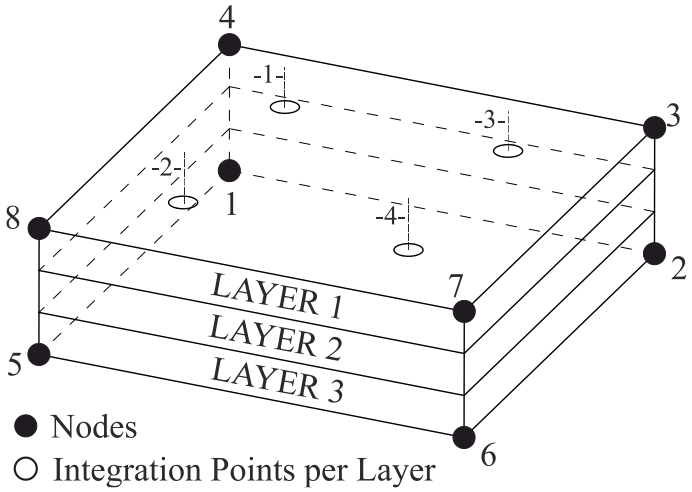

Figure 2.5 Element 149 specifications (Marc Software, 2020)

Contacted elements are grouped and re-arranged by considering the contact interaction between the components aligned with the study led by (McCarthy M. et al., 2005). An illustration of Element 149 is given in Figure 2.5.

An 8-node hexahedral element, type-7, having 3 DOF in each node with a full integration algorithm, was used for the outer elements of the bolt and nut deformable bodies. The bolt has 2560 elements and 2880 nodes; the washers total have 5760 elements and 4800 nodes in the analyses. A 6-node pentahedral element, type-136, having 3 DOF in each node with a full integration algorithm, was used for the bolt's core (inner) elements. In total, 1120 elements and 1202 nodes are generated for the inner core of the bolt. The separated contact bodies are glued if they belong to the same physical body. For example, composite plates were divided into two contract bodies per each. The contacting surfaces and the non-contacting surfaces. This method is applied to speed up contact computations. But in reality, the separated contact bodies may belong to one physical object. In that case, these separated contact bodies were glued together to protect structural integrity.

The material properties of HTA/6376 composites and the steel washers are given in Table 2.1. Poisson's ratio of υ_{31} was recalculated from υ_{13} to be used as input for Marc. The thermal expansion coefficient was defined only in the thickness direction, z, to apply the clamping force. This is the preferred method in (McCarthy M. et al.,

2005) that the thermal effects would generate a clamping effect. The X5CrNiMo18_10_h (as rolled) was chosen as a washer element property, which already exists in the Marc material database. The purpose of this selection is the presence of plastic material properties in the database, which can help remove singularities usually produced in extreme local stresses. Small plastic deformations can eliminate singularity. This material property also has an isotropic hardening rule option. The piecewise linear strain rate approximation method was chosen for stress/strain calculations. The bolt was made of Titanium material and modeled with elastic-plastic isotropic material properties. The Young's modulus and Poisson's ratio were set to 110 GPa and 0.29, respectively.

The "Non-Positive Definite" option was activated in load-case options to increase accuracy, eliminate rigid body motions, and improve the convergence capability for customized time-step options. In the longitudinal pulling case, the face load option was applied as a uniform time-dependent pressure function to reduce solution time and increase numerical stability.

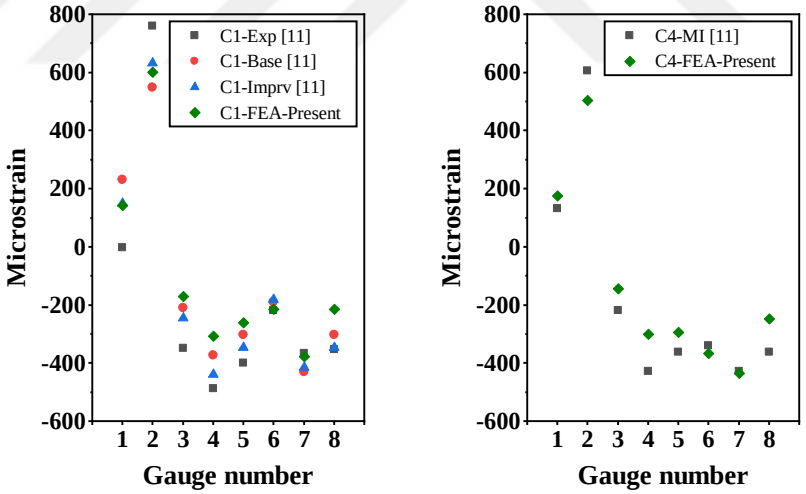

(a) (b)

Figure 2.6 FEA results of C1 (a) and C4 (b) clearances

The strain gauge locations are depicted in Figure 2.3. The FE results were compared with the readings from strain gages and plotted in Figure 2.6. The results are reasonable and can be used in further analyses.

Modeling the damage is essential for this study. However, precise accuracy is not required since the relative comparison would have been done. Damage factors will be used as indicative factors in subsequent analyses while deciding which design performs more viable and reliably using HTA/6376 material. Two studies were selected in the literature for verification study (McCarthy et al., 2010) and (Olmedo & Santiuste, 2012). The first study presented more realistic solutions for the longitudinal tensile loading scenario. An applicable model could be derived for implementing the material nonlinearity to the finite element software. Since a similar HTA/6376 material was used as in the experimental and numerical studies of (McCarthy et al., 2010), the nonlinear portion of the material model was derived from (Olmedo & Santiuste, 2012).

The studies were based on (Hahn & Tsai, 1973) and tried to reveal the relation between shear stress and strain.

$$\gamma_{12} = \frac{\tau_{12}}{G_{12}^{0}} + \alpha \tau_{12}^{3} \tag{2.1}$$

, where γ_{12}, τ_{12}, G_{12}^{0}, and α are the in-plane shear strain, in-plane shear stress, in-plane shear modulus, and the experimental coefficient, respectively. Regarding that, the equation (2.1) can give reasonable results for minor strains.

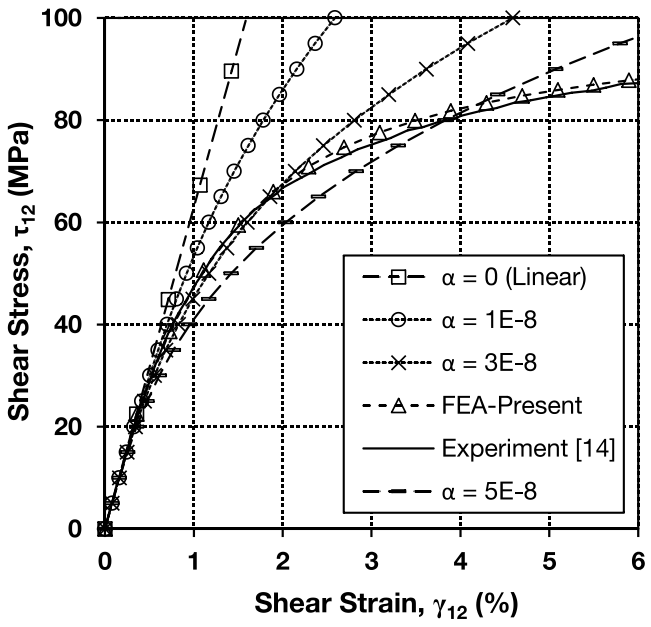

Figure 2.7 Comparison of material nonlinearity in the shear plane

However, the shear stress cannot represent the experiments for larger strain values (Figure 2.7).

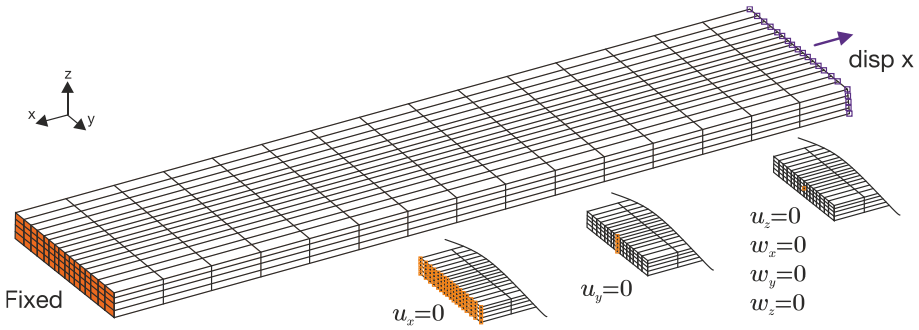

Figure 2.8 $[\pm 45]_{4s}$ pure tension constraints

(American Society for Testing and Materials International, 2013) explains the experimental setup and the calculation method of engineering shear strain. Align with this standard and the study by (McCarthy et al., 2010), 28.8 mm × 121.2 mm HTA/6376 lay-up with the stacking sequence of [±45]4s was selected for modeling by using "Element 149" as given in Figure 2.8. 4 layers or 16 plies were modeled, in which each of the layers contains of 4 laminas with the material properties shown in Table 2.2. 960 elements and 960 nodes were generated for the analyses. The minimum element edge length was taken as 1.4 mm.

Table 2.2 Material properties of HTA/6376 (McCarthy et al., 2010)

Unidirectional HTA/6376					
	GPa		GPa		
E_{11}	145.0	G_{12}	6.30	ν_{12}	0.3
E_{22}	10.3	G_{13}	6.30	ν_{13}	0.3
E_{33}	11.1	G_{23}	3.95	ν_{23}	0.5

A linear function applied the "disp x" constraint in (Figure 2.7) in the x direction. It was zero initially and equal to 10 mm one second later. The fixed end constraints were applied as three separate boundary conditions fixing the highlighted nodes in the DOF represented in Figure 2.8. This is a well-known 3-2-1 method aiming to compensate

for the stress concentration effect near the fixed region and improve the numerical accuracy. These three boundary conditions are given in Figure 2.8.

Concerning the (American Society for Testing and Materials International, 2013), equations (2.2) and (2.3) were used for the calculations to get G_{12}, which was the primary input for FE software as a material property.

$$\tau_{12,i} = \frac{P_i}{2(wh)} \tag{2.2}$$

$$\gamma_{12,i} = \varepsilon_{x,i} - \varepsilon_{y,i} \tag{2.3}$$

$$\tau_{12} = G_{12}\,\gamma_{12} \tag{2.4}$$

where $\tau_{12,i}$, P_i, w, h, $\gamma_{12,i}$, $\varepsilon_{x,i}$, $\varepsilon_{y,i}$, τ_{12}, G_{12}, and γ_{12} are shear stress at i^{th} data point, force at i^{th} data point, coupon width, coupon thickness, engineering shear strain at i^{th} data point, longitudinal normal strain at i^{th} data point, and lateral normal strain at i^{th} data point, shear stress, shear modulus, and engineering shear strain, respectively.

Marc/Mentat has advanced options to execute user-defined subroutine codes, giving the ability to change or add features to the finite element analysis that does not exist in the package. Marc can use Python and Fortran software development tools to meet this requirement. Python may have more contemporary options than Fortran, but Marc still has software components written in Fortran. The main reason for this is the speed of the Fortran language.

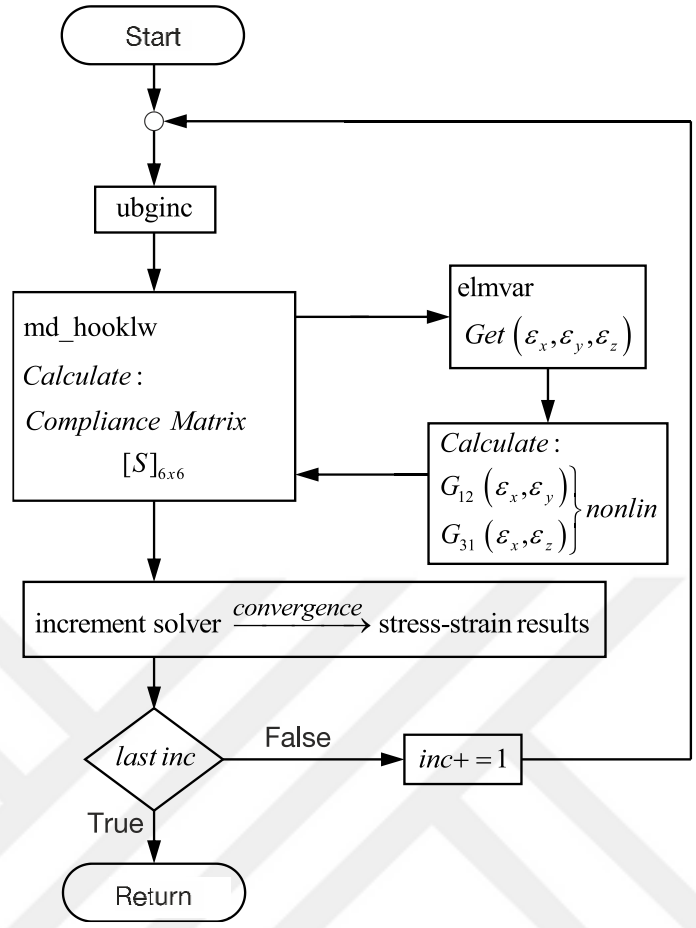

Figure 2.9 Flow chart for material nonlinearity

Therefore, the Fortran development environment was used for the material modeling studies. A small subroutine is compiled in Fortran to implement nonlinearity. A simple flow chart is given in Figure 2.9.

First, G_{12} was derived from the experiments using equation (2.4), then the curve of shear modulus - shear strain was fitted to a 4th-degree polynomial function. This polynomial function was then implemented as a software function in Fortran; then, the program was executed related to the flow chart given in Figure 2.9. In this flow chart, ubginc is the internal Fortran program starting at the beginning of each increment. If the md_hooklw option was activated in the material properties window, the ubginc calls the md_hooklw. md_hooklw allows changing or manipulating the material properties by changing the stiffness or compliance matrix of orthotropic materials. On the other hand, an internal function of elmvar allows to get elemental variables such

as strains. These variables are stored in the memory per layer and per integration point. Therefore, as mentioned, the shear modulus was changed in every increment to maintain the correlation between experimental data concerning the 4th-degree polynomial function. The 4th-degree polynomial function is tuned iteratively. The results closely fit the experimental data, as shown in Figure 2.7.

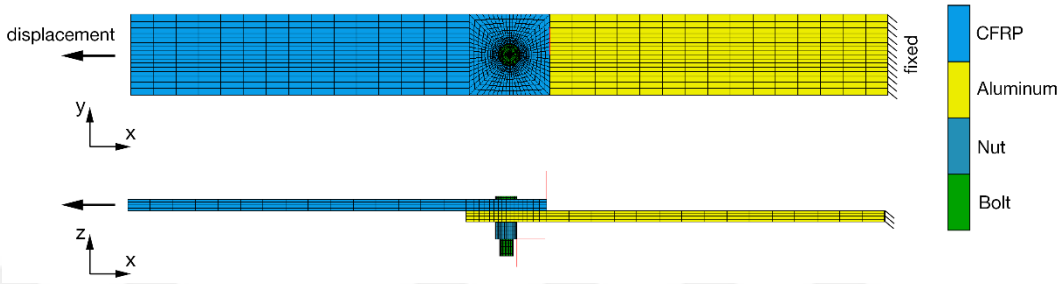

Figure 2.10 FEA model for damage verification

The main damage rules were derived from the study (Olmedo & Santiuste, 2012) for the HTA/6376 material. The FE model was designed as in Figure 2.10. The CFRP laminate and the AA7475-T76 aluminum plate were fastened by a 6Al114VSTA titanium bolt and nut couple; then, they pulled in the direction of the displacement vector shown in Figure 2.10. The stacking sequence of the CFRP was taken as $[(0/\pm45/90)_2]_s$. The coupon and the aluminum plates have a width and height of 28.8 mm and 150 mm, respectively. The diameter of the bolt hole was 4.85 mm. The aluminum plate and the composite laminate thicknesses were 4 mm and 4.16 mm, respectively. The distance from the center of the bolt hole to the closer edge was 14.4 mm.

The composite plate was designed in four layers, each consisting of 4 laminas. A total of 12480 elements were generated for this model. 5056 type-149 elements with 3163 nodes for the composite laminate, 5056 type-7 elements with 3163 nodes for aluminum plate, 1344 type-7 elements with 725 nodes for the outer bolt, 640 type-136 elements with 66 nodes for the bolt-core, and 384 type-7 elements with 449 nodes for the nut were generated in the analyses. The minimum element edge length close to the hole was measured as 0.23 mm. Friction properties were defined as explained in

previous pages. The boundary conditions in Figure 2.10 were applied, as illustrated in Figure 2.8.

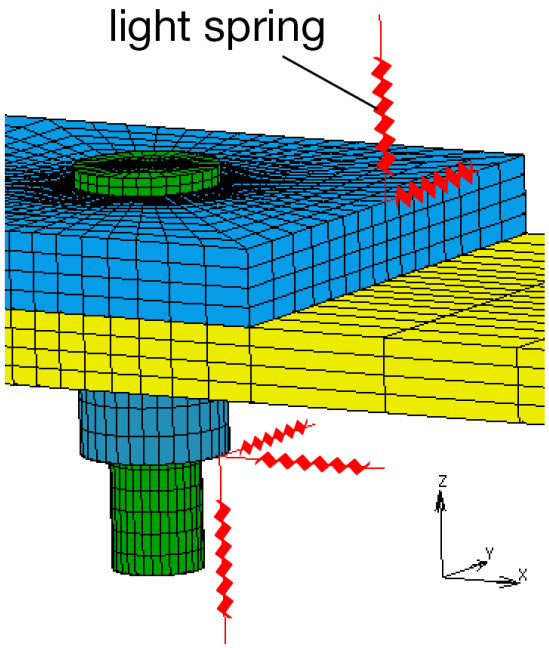

Figure 2.11 Light springs for numerical stability

Light spring elements having 10 N/mm stiffness were linked to the model to eliminate rigid-body movements (Figure 2.11). 10.4 kN preload, derived from the 10 Nm of bolt torque, was distributed to the lower-end surface area of the bolt shaft as a uniform pressure. Pressure load was applied as a linear function from zero to the max—value through the load-case. The nut was fixed in the z-direction at the bottom during preloading while the bolt moved in the -z-direction. The “Follower force” option was activated, sustaining the clamp load and its direction through the load case. The bounded elements were not released at the end of the load step. A new load case was added before the longitudinal pulling stage. In this load case, nut elements were immediately glued with the bolt elements to maintain the clamping condition and to minimize element relaxation. As a subsequent action, a linear function from zero to the maximum was applied as a lateral displacement for the longitudinal pulling case.

Table 2.3 Material properties (Olmedo & Santiuste, 2012)

HTA 7/6376 endurance limits		MPa
Longitudinal tensile strength	X_T	2250
Longitudinal compressive strength	X_C	1600
Transverse tensile strength	Y_T	64
Transverse compressive strength	Y_C	290
Longitudinal tensile strength	Z_T	50
Longitudinal compressive strength	Z_C	300
In-plane shear strength	S_{12}	120
In-plane shear strength	S_{13}	120
Out-of-plane shear strength	S_{23}	50

Metallic material properties		
	AA7475-T76	6Al114VSTA
E (GPa)	69.00	110.00
ν	0.28	0.29
Yield Stress (MPa)	451.00	1030.00

The mechanical properties of HTA 7/6376 were similar to Table 2.2, except for G_{12} and G_{13}, which were the nonlinear and strain-dependent properties as explained above. The mechanical endurance limits for the composite plate are given in Table 2.3.

The equations below were critical for the analyses as they define the limits of mechanical damage inside the material. The damage criteria and the equations were derived from the study (Olmedo & Santiuste, 2012), and are summarized as follows:

Matrix crushing failure:

$$\sigma_2 < 0 \Rightarrow \; d_{mc2} = \sqrt{\left(\frac{\sigma_2}{Y_C}\right)^2 + \left(\frac{\tau_{12}}{S_{12}}\right)^2 + \left(\frac{\tau_{23}}{S_{23}}\right)^2} \tag{2.5}$$

$$\sigma_3 < 0 \Rightarrow \; d_{mc3} = \sqrt{\left(\frac{\sigma_3}{Z_C}\right)^2 + \left(\frac{\tau_{13}}{S_{13}}\right)^2 + \left(\frac{\tau_{23}}{S_{23}}\right)^2} \tag{2.6}$$

Matrix cracking failure:

$$\sigma_2 > 0 \Rightarrow \; d_{mt2} = \sqrt{\left(\frac{\sigma_2}{Y_T}\right)^2 + \left(\frac{\tau_{12}}{S_{12}}\right)^2 + \left(\frac{\tau_{23}}{S_{23}}\right)^2} \tag{2.7}$$

$$\sigma_3 > 0 \Rightarrow \; d_{mt3} = \sqrt{\left(\frac{\sigma_3}{Z_T}\right)^2 + \left(\frac{\tau_{13}}{S_{13}}\right)^2 + \left(\frac{\tau_{23}}{S_{23}}\right)^2} \tag{2.8}$$

Fiber-matrix shearing failure:

$$\sigma_1 < 0 \Rightarrow \; d_s = \sqrt{\left(\frac{\sigma_1}{X_C}\right)^2 + \left(\frac{\tau_{12}}{S_{12}}\right)^2 + \left(\frac{\tau_{12}}{S_{12}}\right)^2} \tag{2.9}$$

Fiber failure:

$$\sigma_1 < 0 \Rightarrow \; d_{fc} = \left|\frac{\sigma_1}{X_C}\right| \tag{2.10}$$

$$\sigma_1 > 0 \Rightarrow \; d_{ft} = \sqrt{\left(\frac{\sigma_1}{X_T}\right)^2 + \left(\frac{\tau_{12}}{S_{12}}\right)^2 + \left(\frac{\tau_{13}}{S_{13}}\right)^2} \tag{2.11}$$

Table 2.4 Definition of failure indices

	f (index nr.)	Criteria	Index Value	Equation(s)
Matrix Crushing (compression)	1	$\sigma_2 < 0$ or $\sigma_3 < 0$	$\max(d_{mc2}, d_{mc3})$	2, 3
Matrix Crushing (tension)	2	$\sigma_2 > 0$ or $\sigma_3 > 0$	$\max(d_{mt2}, d_{mt3})$	4, 5
Fiber-Matrix (shear)	3	$\sigma_1 < 0$	d_s	6
Fiber (compression)	4	$\sigma_1 < 0$	d_{fc}	7
Fiber (tension)	5	$\sigma_1 > 0$	d_{ft}	8

Once one or more criteria in equations (2.5) to (2.11) were satisfied, the material would degrade and would get weakened in the corresponding direction(s). Therefore, these criteria with the equations were implemented to the ufail subroutine code in conjunction with Table 2.4. Multiple equations for matrix crushing failure induced by compression and tension were merged in one failure index per case, f_1 and f_2, respectively.

As explained in Figure 2.9, the compliance matrix could be manipulated by md_hooklw if the material option was activated. Since the shear modulus was nonlinear, and the resultant damage factors were not applied to all elasticity modulus (S_{12}, S_{13}, S_{23}), defining a compliance matrix for all elements, layers, and integration points was necessary. Therefore, the new compliance matrix must be defined as:

$$[S] = \begin{bmatrix} \frac{1}{E_1 d_1} & -\frac{\upsilon_{12}}{E_1} & -\frac{\upsilon_{13}}{E_1} & 0 & 0 & 0 \\ & \frac{1}{E_2 d_2} & -\frac{\upsilon_{23}}{E_2} & 0 & 0 & 0 \\ & & \frac{1}{E_3 d_3} & 0 & 0 & 0 \\ & & & \frac{1}{G_{12} d_4} & 0 & 0 \\ & & symmetric & & \frac{1}{G_{23} d_5} & 0 \\ & & & & & \frac{1}{G_{31} d_6} \end{bmatrix} \quad (2.12)$$

where d_1, d_2, d_3, d_4, d_5, and d_6 represent the reduction factors for material degradation.

Table 2.5 Material degradation ratios (%)

Failure mode	d_1	d_2	d_3	d_4	d_5	d_6
Fiber tension	0.14	0.40	0.40	0.25	0.25	0.20
Fiber compression	0.14	0.40	0.40	0.25	0.25	0.20
Fiber-Matrix shear				0.25	0.25	
Matrix tension		0.40	0.40			0.20
Matrix compression		0.40	0.40			0.20

These reduction factors are given in Table 2.5.

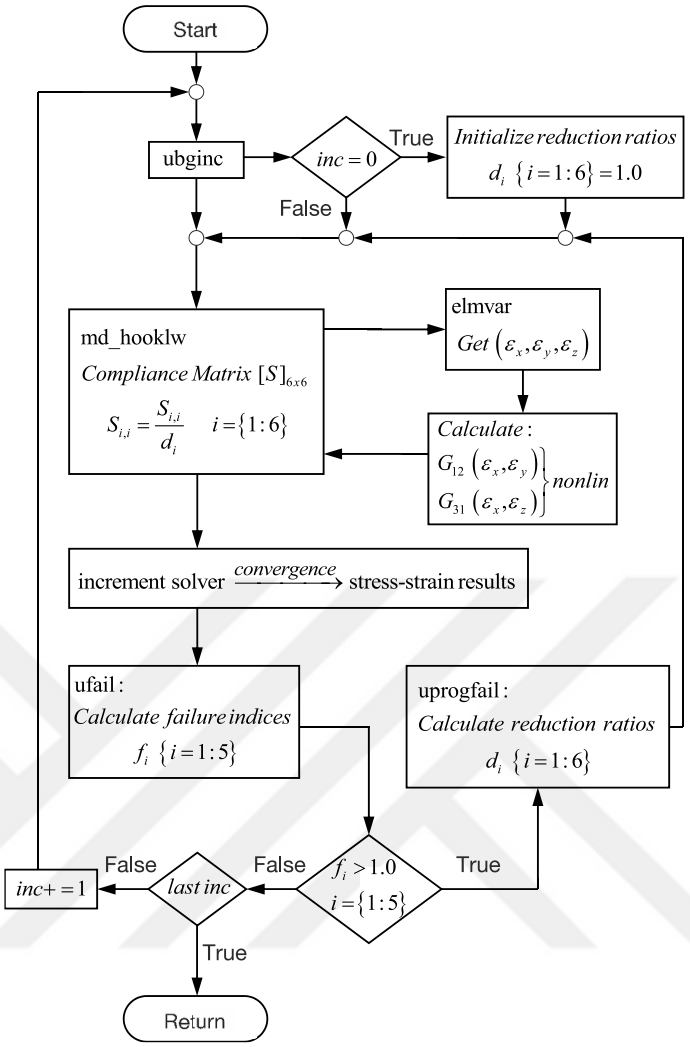

Figure 2.12 Flow chart for progressive damage with nonlinear shear stress-strain relations

Marc was programmed to execute the modules according to Figure 2.12 to utilize the method via Fortran. A limited number of internal common blocks were implemented to the code, such as concom, elemdata, dimen, array2, tbwbcs, to acquire the elemental or scalar variables, like the increment number, load case id, elemental data, variable dimensions, etc. According to this method, S_{ij} was calculated once per thread cycle. Therefore, previous calculations of d_i cannot build up on S_{ij}. However, d_i continuously decreases if one or more damage criteria are satisfied.

2.2 Ductile damage modeling

External thin-walled metal structures such as sleeves or sheet metals were widely used in the industry in bolted composite joints. These structural elements could be damaged during the assembly. In some cases, these ductile damages could degenerate the sleeve geometry and make the parts impossible to operate. In our case, thin stainless-steel material would be used as a sleeve object, which was supposed to be deformed by large strain values. To understand the damage characteristics of the sleeve, a study by (Ben Othmen et al., 2020) was selected to obtain a ductile damage threshold value for Marc as an FE input. (Ben Othmen et al., 2020) investigated the ductile fracture of AISI 304L stainless steel sheet metal by using FEA. Their experimental cupping tests were replicated in an FE environment, and their results were compared with the FE results in this thesis to verify displacement-strain and displacement-force relations. Then, the damage value calculated in the FE environment was linked to the stroke value, which the rapture began in the experiment.

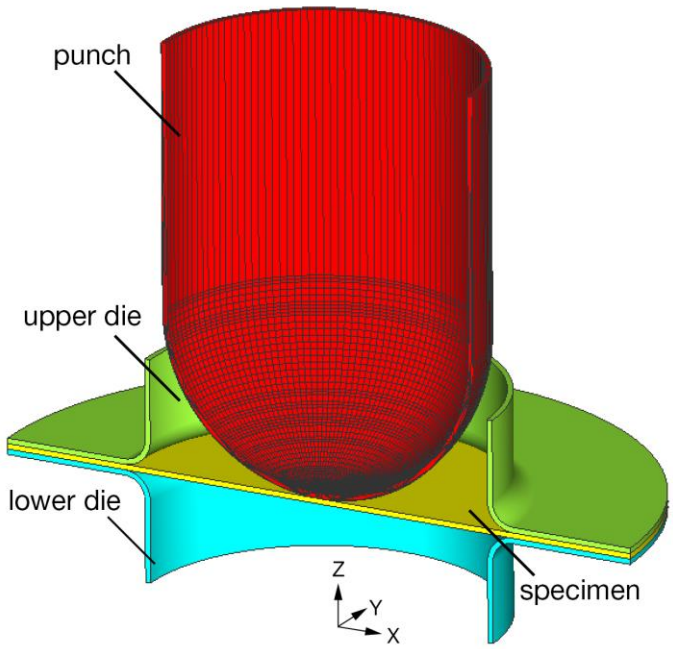

Figure 2.13 Simulation model for cupping test

A FE model representing the experimental conditions was generated in Marc/Mentat. ¼ symmetrical model was built using a stainless-steel sheet metal with

1 mm of thickness and 120 mm of diameter. A type-185 3D solid shell element with 8-node brick topology was selected by activating the enhanced assumed strain formulation for transverse normal and shear components. A circular zone of 40 mm diameter was selected, and the elements inside this diameter were refined for accuracy. The minimum element size was measured as 0.36 mm, and the total number of elements was 10732. 7 layers were used for this type of element. The FE model is given in Figure 2.13.

Even though there is a standard ruling the test geometries (International Organization for Standardization, 2014), the parameters in (Ben Othmen et al., 2020) are used for modeling and analysis. The lower and upper dies are modeled identically, where they have a 65 mm inner diameter with a 5 mm radius and a 120 mm outer diameter. The punch nose is modeled as a hemisphere having a radius of 60 mm. All three dies are modeled as rigid tools, and the sheet metal is deformable elastic-plastic as a workpiece. The friction coefficient between the punch and the workpiece is set to 0.2. The mechanical properties of AISI 304L material are set as E=200 GPa, υ=0.3, where E and υ represent the modulus of elasticity and the Poisson's ratio, respectively. The flow stress of AISI 304L material is defined in the tabular form by combining the formulation given in equation (2.13) from ε_p=0 to the necking point ε_p=0.451, and the experimental tabular data from the necking point to the rupture in (Ben Othmen et al., 2020).

$$\sigma = \sigma_0 + Q\left(1 - e^{-b\varepsilon_p}\right) \tag{2.13}$$

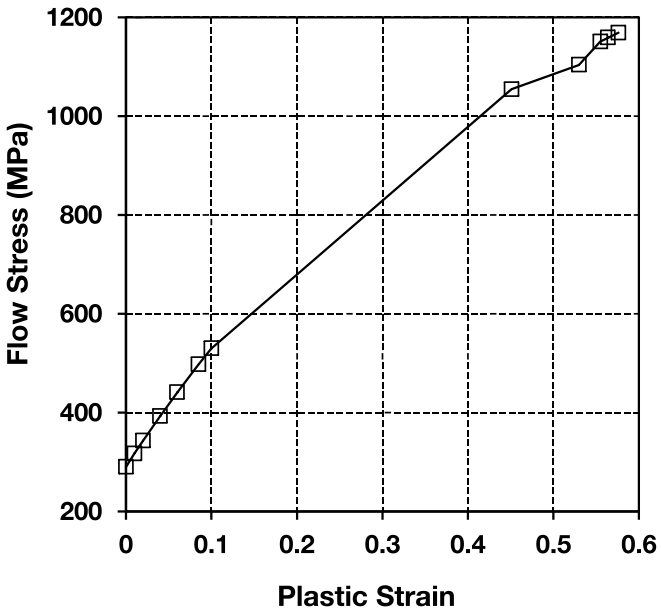

Figure 2.14 Flow stress for AISI 304L

The anisotropic material properties were taken from (Ben Othmen et al., 2020) as is and are dumped into Marc by using the Hill'48 anisotropic yield criterion (Hill, 1998).

Table 2.6 Tensile properties of the AISI 304L (Ben Othmen et al., 2020)

Angle with Rolling Direction (°)	*Yield Stress (MPa)*	*Anisotropic coefficient* r_α
0	*278*	*0.87*
45	*270*	*1.16*
90	*280*	*0.82*

The critical parameters are given in Table 2.6.

The FE process consists of two stages. In the first stage, the upper die was pressed to the specimen by 158 kN of axial force. In the second stage, the punch was moved in the -z direction for bulging the sheet metal.

$$\int \frac{\sigma_{max}}{\bar{\sigma}} \dot{\bar{\varepsilon}}\, dt \geq C \tag{2.14}$$

, where σ_{max} is the maximum principal stress, $\bar{\sigma}$ is the effective von Mises stress and $\dot{\bar{\varepsilon}}$ is the effective plastic strain rate. C is the material constant for damage.

Since Marc has an option for the Cockroft & Latham damage parameter to compute ductile damage, this model was used and matched with the rupture strain, which was different than the method used (Ben Othmen et al., 2020). The material constant C in equation (2.14) is the main input as a damage initiation threshold to indicate damage inside the material.

2.3 Primitive Models

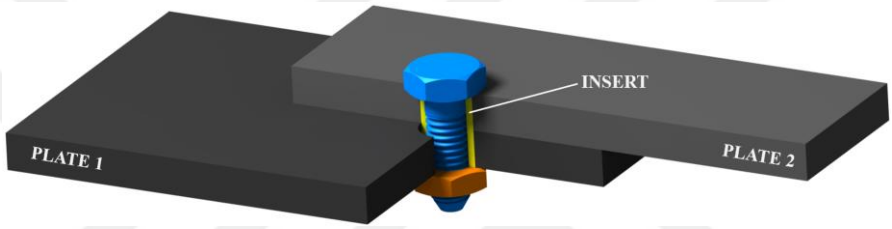

Figure 2.15 Bolted connection with a metal insert

Using one of the most common methods to fix two or more composite parts together by an insert, bolt, and nut (Figure 2.15) may have some consequences.

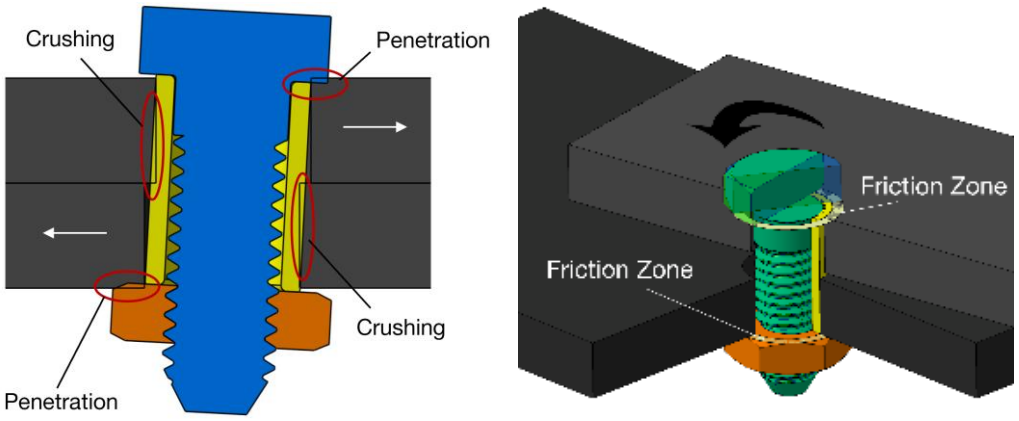

Figure 2.16 Bolted connection with a metal insert

These consequences are like local matrix crushing, penetration, and wear, as shown in Figure 2.16.

However, SPR or clinching methods have many applications in the aerospace industry. Some best-practice designs require precise hole dimensions or other special treatment in the bolt hole. Some of these methods were exemplified in the previous chapters. In this section, primitive design candidates were modeled to get the final form.

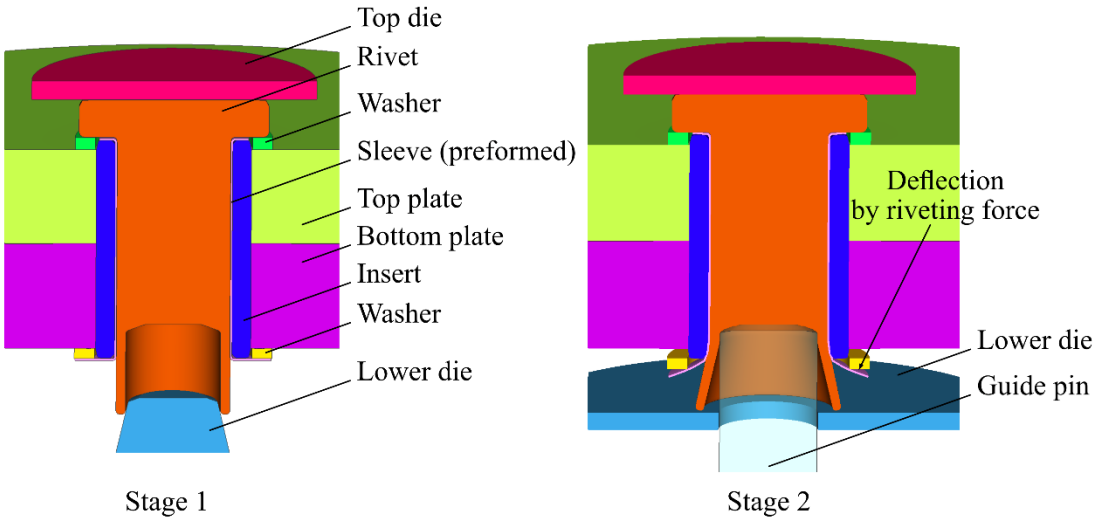

Figure 2.17 Primitive model for bulk forming

Primitive models comprised composite plates, bolt, nut, rivet washers, insert, and forming dies (Figure 2.17). The purpose of these primitive models was to obtain the final form of the sleeve geometry. Composite plates were modeled as isotropic elastic steel components to speed up the computations, and the whole model was designed as 2D-axisymmetric. Since the focus was on the topology of the sleeve geometry, composite properties were not applied to the FE models.

There were two main concepts analyzed. The first was the bulk-forming or, namely, rivet-type joint, and the other was the bolted joint with metal-forming applied. As mentioned in the previous sections, analyses were based on the 2-D and axisymmetric models. Since the focus was on the sleeve geometry, the composite plates were modeled as isotropic steel parts.

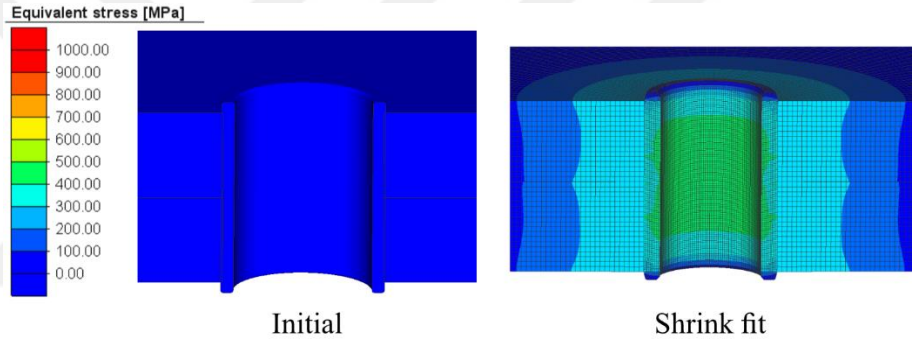

Figure 2.18 Shrink-fitting process

All models have the same insert geometry (in diameter) and an I-F ratio of 2.1%. The shrink-fitting process is exemplified in Figure 2.18.

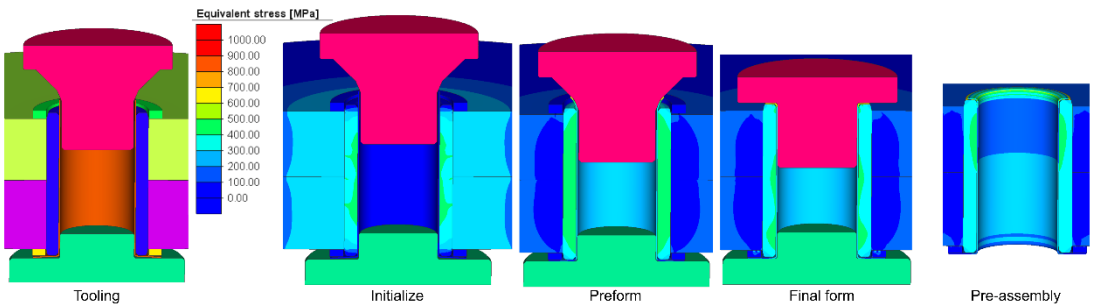

Figure 2.19 Short-sleeve (pre-assembly)

The concept in Figure 2.19 was to minimize direct contact with the insert and the bolt. Additionally, as seen in the pre-assembly module, the sleeve's lower flanged portion can help retain the washer in contact with the composite. This was supposed to reduce the secondary bending effect slightly.

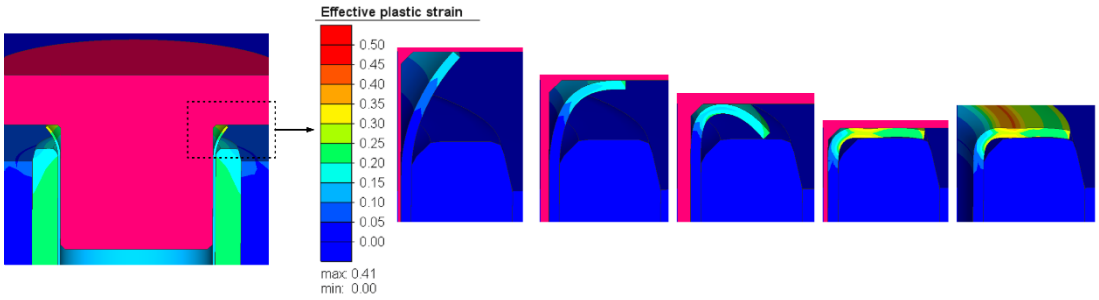

Figure 2.20 Short-sleeve plastic strain distribution

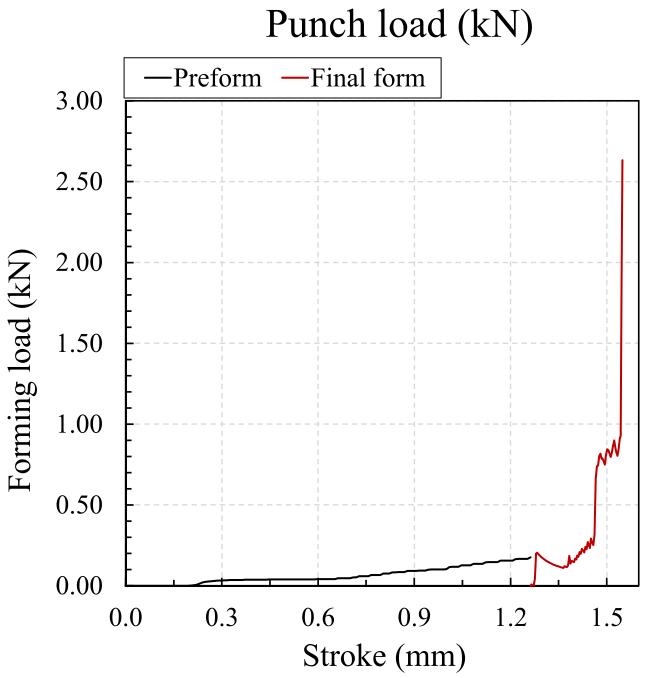

Figure 2.21 Short-sleeve forming load.

The forming force history during the process is plotted in Figure 2.21.

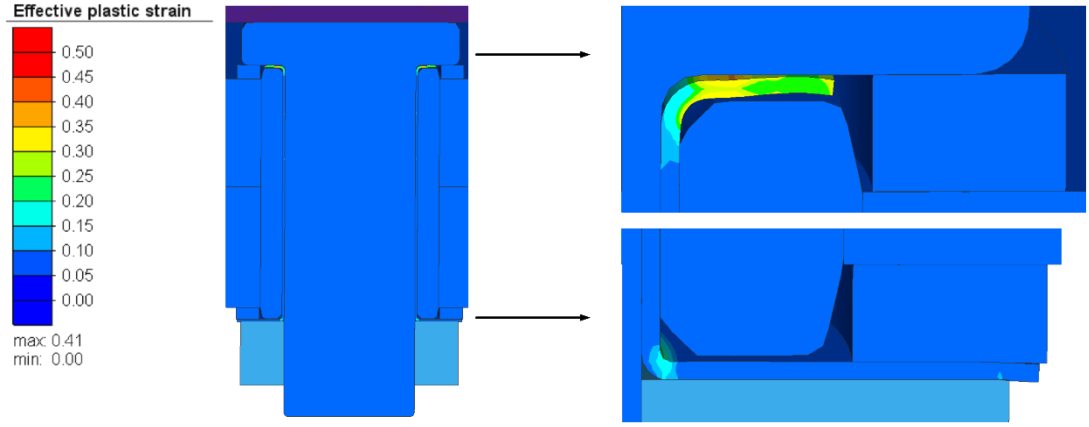

Figure 2.22 Tightening results for the short-sleeve configuration in Figure 2.20; plastic strain distribution (the clamping load is 10 kN)

The desired final assembly is given in Figure 2.22. With this design, more force can be transmitted to the composite plates. The residual plastic strains on the sleeve (Figure 2.20) may produce reaction forces during the secondary bending phase, which can help reduce the moment in the corners on the opposite side. This effect will be discussed in further sections.

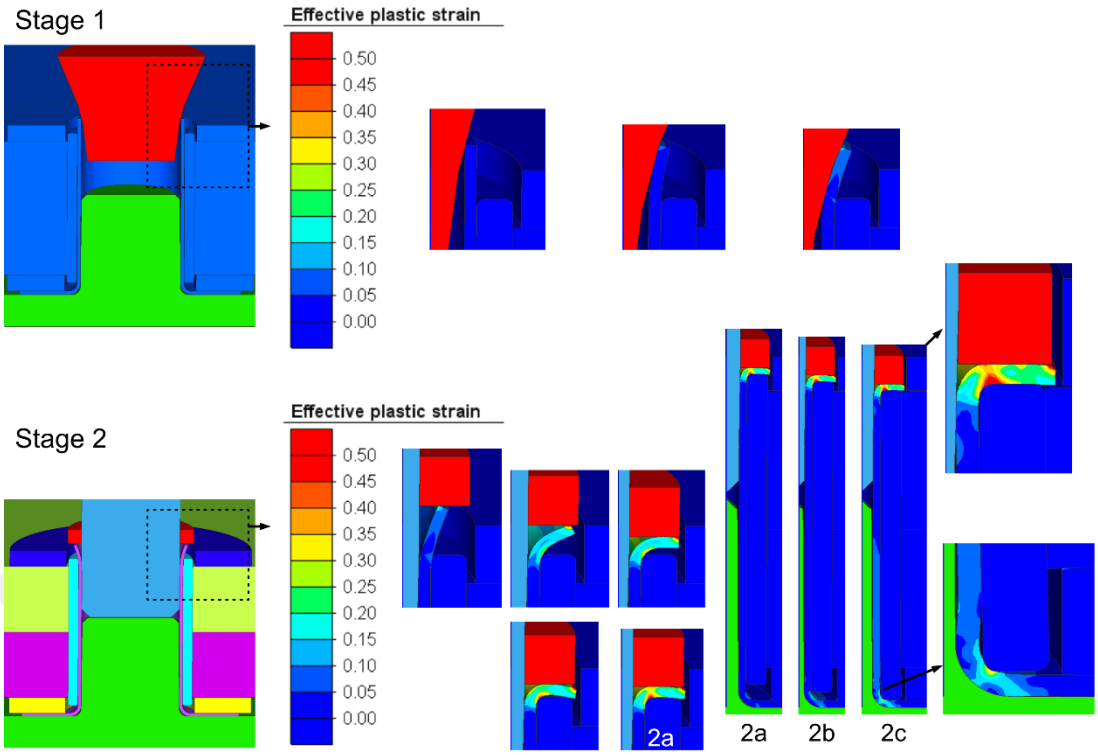

Figure 2.23 Short-sleeve, sliding-insert case plastic strain distribution

Similar to Figure 2.19 and Figure 2.20, a larger washer can reduce the contact pressure between the composite plates and the washer. It can be seen in Figure 2.23 that the sleeve can slide to the end under excessive forming load. The required forming load was computed as 6.7 kN, 7.2 kN, and 13 kN at 2a, 2b, and 2c positions, respectively.

The sliding effect generates a stress concentration; therefore, the concept did not apply to the final geometry.

The longer sleeve concept was analyzed for reducing or eliminating the relative sliding effect between the bolt and the nut. The idea was to let the washer and the sleeve move relatively but to limit the relative displacement between the bolt and nut by limiting the relative motion between the sleeve bolt and sleeve nut. However, buckling was observed in the FE analysis, as seen in Figure 2.24. The total forming was computed as 0.51 kN for the case in Figure 2.24.

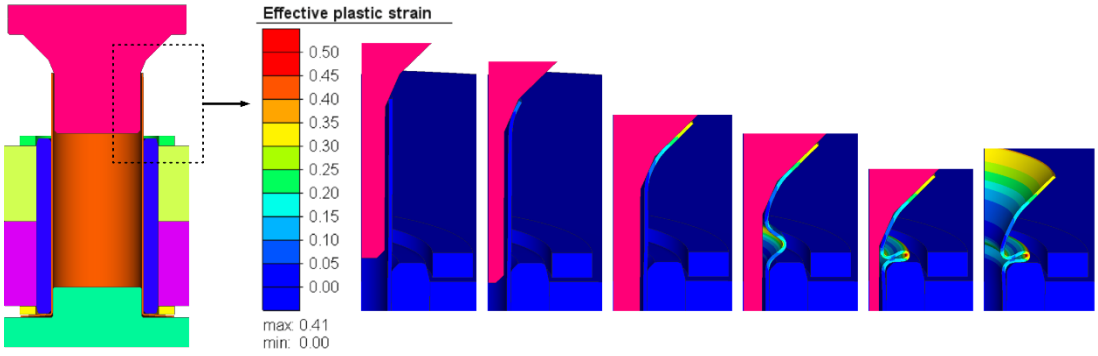

Figure 2.24 Long-sleeve plastic strain distribution

The preform geometry was optimized for the long-sleeve case, as in Figure 2.25. The forming load in Figure 2.25 was 10 kN, suitable for a composite plate, meaning that minimum damage can occur in the composite. The excessive strains and the damage factors over the damage threshold limit indicate that the sleeve would get damaged during the forming operation.

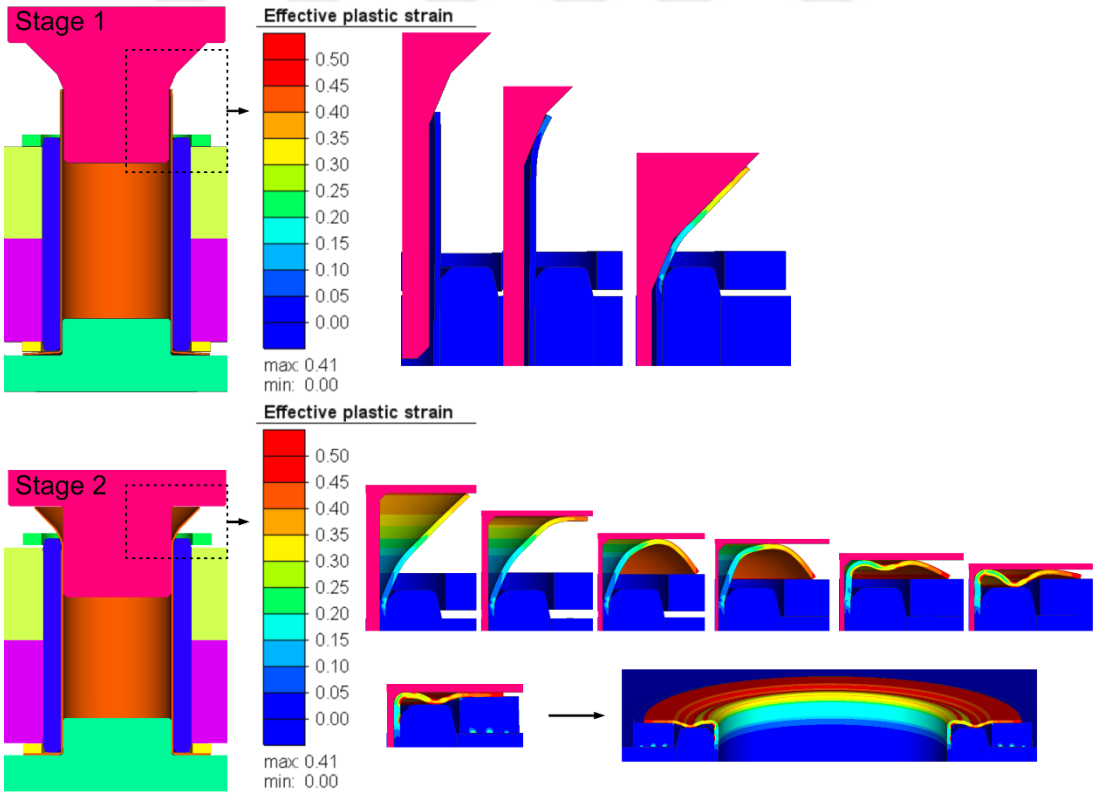

Figure 2.25 Optimized long-sleeve plastic strain distribution

Additionally, the long-sleeve method may result in buckling, as in Figure 2.24 and Figure 2.26. The supporting pin needs to have a tight tolerance to eliminate buckling risk.

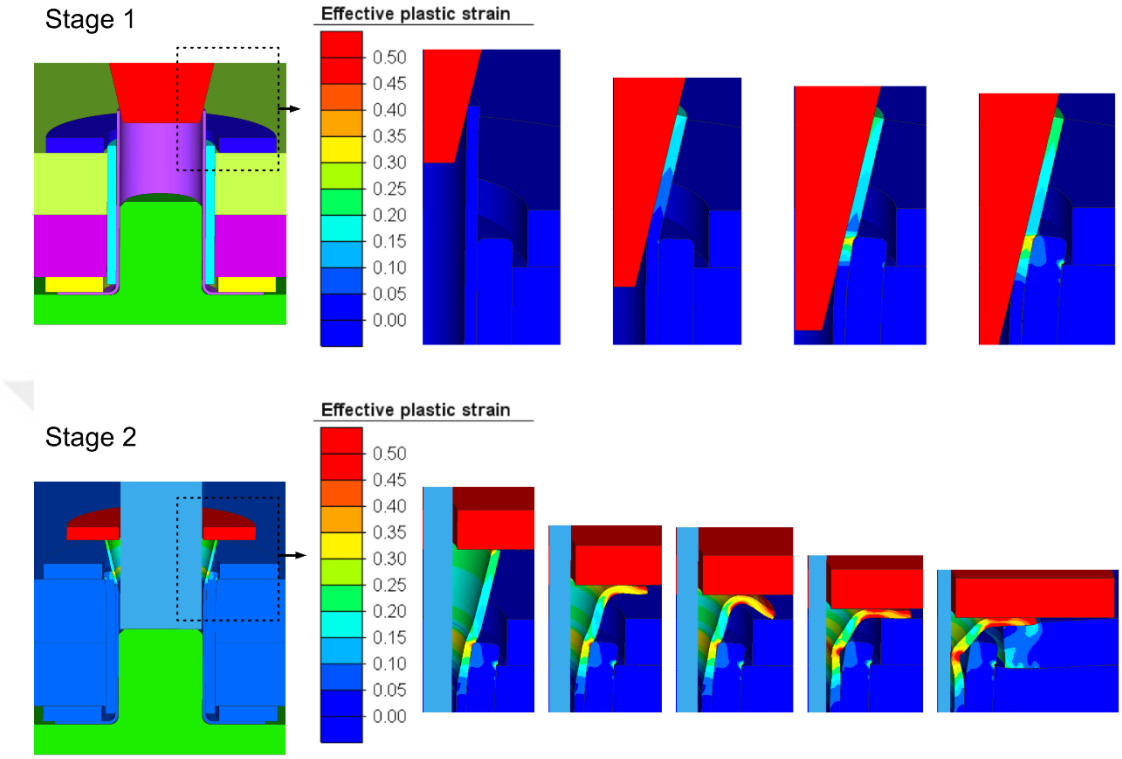

Figure 2.26 Optimized long-sleeve with method two plastic strain distribution.

The forming load in Figure 2.26 was computed as 4.52 kN on Stage 1. At stage 2, stable seating and loading conditions prevail if the clamp load is 2.37 kN. Once the threshold is exceeded, the excessive deformation hits 14.1 kN, which can trigger a catastrophic damage scenario.

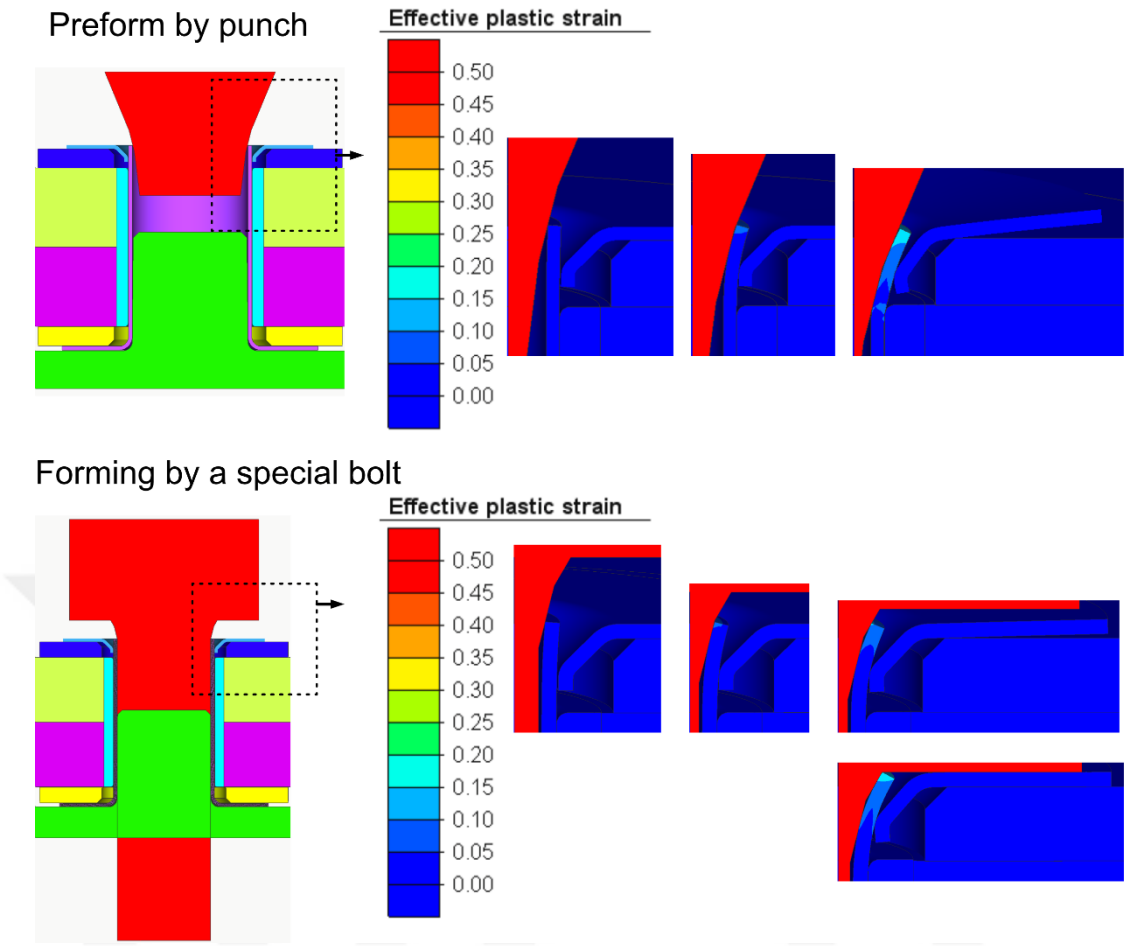

Figure 2.27 Multi-segment sleeve with a punch and a special bolt, plastic strain distribution

The sleeve material can be divided into two or more pieces. However, this would require more forming stages, adversely affecting the cost. Therefore, the forming sequence can be transferred to the bolt geometry, as in Figure 2.27, to reduce assembly time. The preform load was computed as 0.77 kN, and the final load was predicted as 2kN by a special bolt (Figure 2.27). Assembly force can be redefined depending on the clamping force.

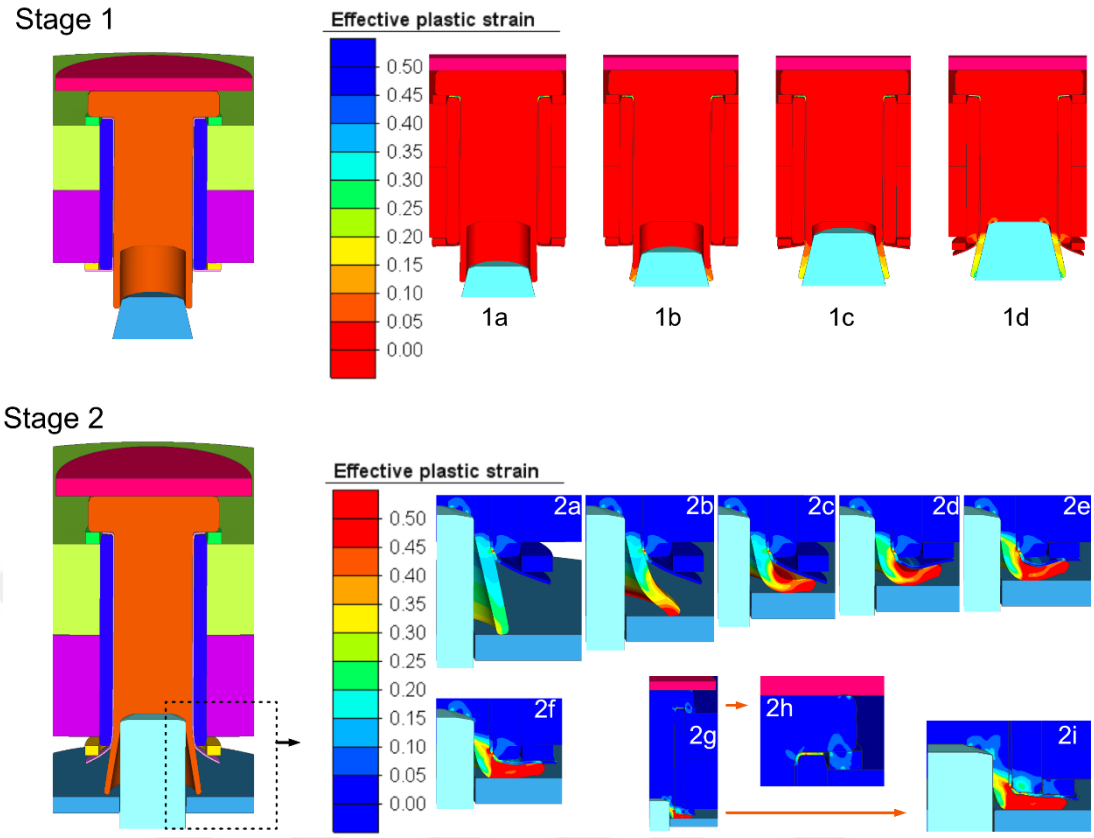

Figure 2.28 Bulk-forming, plastic strain distribution

The bulk forging case was simulated in Figure 2.28. The forming load at 1d moment was computed as 13.7 kN in Figure 2.28. However, it was 5 kN at the 1c moment. Therefore, the forming load can be reduced to 5 kN for the first stage. At the 2e moment, the forming load was calculated as 10 kN, which was applied to the composites. However, the forming force could advance up to 39.7 kN to cause complete damage in the joint area.

2.4 Final Model

This thesis proposed a wide-spectrum model for net-fit and press-fit conditions. The method consists of six primary geometries. The first geometrical body is the insert, which is a direct fit to the hole; the second and third are the top and bottom washers; the fourth is the sleeve that covers the washers; the fifth and the sixth are the bolt and

the nut which are coupled together to ensure the clamping load. Additionally, an O-ring can be applied between the washer-insert-sleeve interfaces for sealing. The sleeve was separated into two segments to understand whether or not the proposed benefits explained further could be achieved. The analyses were planned with and without the sleeve(s) for benchmarking.

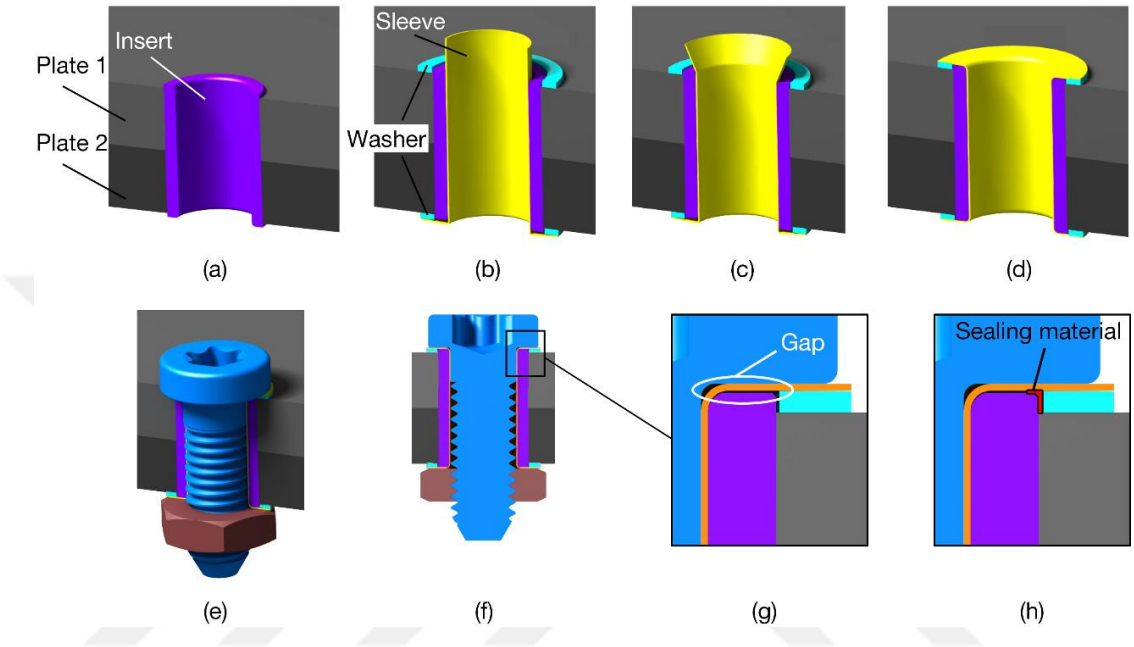

Figure 2.29 Proposed model, assembly components: insert (a), washers and sleeve (b), pre-forming sleeve (c), formed sleeve (d), bolt-nut configuration over the assembly (e), the cross-section of final assembly (f), detailed view of bolt seating region (g), an optional sealing material (h)

Direct contact between the bolt under-head form and the bolt shank with the composite parts can cause severe damage around the contact area, which was experimentally exposed (Zuo et al., 2020). Therefore, the main principle of the proposed model in Figure 2.29 was to reduce or eliminate the geometrical bonding effect between the composite structure and the main load-carrying body (the bolt-nut couple). Separating the insert and bolt bodies using a sleeve (as an isolator) reduces the matrix damage around the radially prestressed area carrying some portion of bending moment under lateral loads and positively improves the damage resistance on higher clamping force values. Additionally, using a washer can help obtain homogeneous stress distribution and avoid direct contact of the bolt and nut to the

composite surface. Moreover, it can help apply more clamping load or more torque to the bolt without damaging the composite laminate if the outer diameter of the washer is wide enough. However, increasing the washer size excessively may decrease the bearing strength of the connection if the clamping load is not set correctly. The proposed model in Figure 2.29-g provides more robust bearing durability. The clamping force is directly transferred to the washer since there is a gap between the insert and the sleeve.

The COF on the bolt-to-composite and nut-to-composite interface layers would be higher than on the interface layers between the bolt and nut threads if there are not any washers used in the connection. Therefore, it would have a higher probability of losing clamping force over time, in addition to the wear on the composite surface. However, using a washer can decrease the wear between the washer-laminate interface and reduce the loosening rate. Since the COF between steel-composite is higher than steel-steel, bolt-nut couple slips, and the washer sticks on both sides. Hence, the bolt-nut couple becomes more susceptible to micro-slips, resulting in the loss of clamping load. This is an issue of vibrational loading situations. To eliminate this problem, a sleeve body is added to the model, as shown in Figure 2.29. The separated sleeve acts as a sticker body that sticks to the bolt and nut but slips over the washer. So, the relative motion between the bolt and the nut can be minimized. For an exact solution to this problem, it should be considered to use special chemicals or a serrated under-head pattern on the bolt to ensure tightening.

The other main advantage of using the proposed sleeve model in Figure 2.29 is that the residual stresses after the plastic deformation of the sleeve material (Figure 2.29-c, d) provide additional resistance to the assembly, preventing separation of the adjacent composite plates. The residual stress on the sleeve material can carry bending moments perpendicular to the bolt axis, reducing excessive pressure over the composite surface.

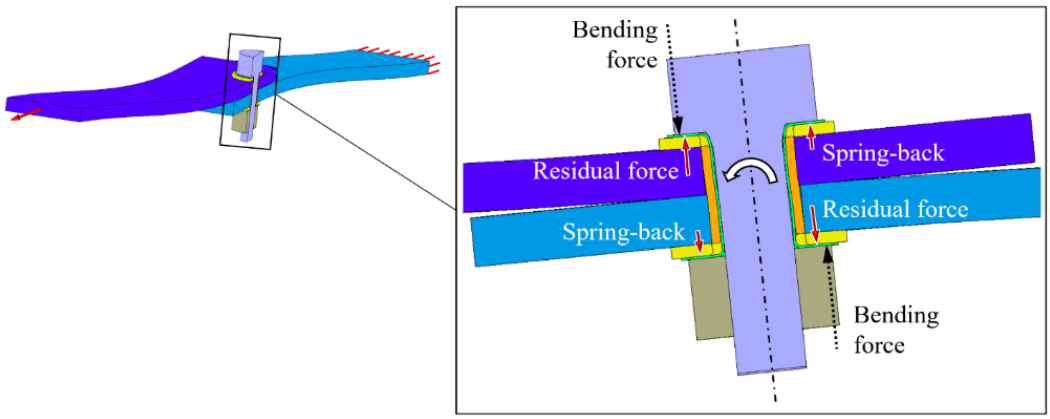

Figure 2.30 Residual forces coming from post-plastic-metal

The plastic deformation improves the yield stress of the sleeve because of the strain-hardening effect. As shown in Figure 2.30, residual forces reduce the bending force, resulting in less stress concentration on the composite surface. On the other hand, the spring-back effect, which is the resultant elastic stress of the metal forming process (Figure 2.29-b, c), can provide additional force to help maintain the friction between the sleeve and the bolt bodies. The principal was to bind the bolt and the nut to a single body (the sleeve). Therefore, with the spring-back and the residual forces combined, bending would cause significantly less relative motion between the bolt and the nut. So, the anti-loosening capability of the connection is improved.

The sleeve can also carry additional clamping force as compressive stress without transferring it to the composite body. Therefore, more clamping force can be applied to the bolt without damaging the composite surface, improving the stability of the bolt-nut couple under laterally vibrating loads. Another alternative to the bolt-nut couple is to use a rivet. However, this solution will remove the flexibility advantage of the design because detaching a rivet is not practical for maintenance. Additionally, riveting can damage the composite (Jiang et al., 2021). Essentially, the model introduced here aims to support and ensure a reliable and maintenance-friendly connection between one or more composite laminates.

According to the main design concept, the sleeve and insert materials were made of stainless steel. The outer diameter of the insert material was slightly greater than the

diameter of the hole, providing an interference-fit condition. The outer diameter of the sleeve was smaller than the inner diameter of the insert. The inner diameter of the finished sleeve (Figure 2.29-d) was equal to or slightly smaller than the bolt shaft diameter. Therefore, the clinching process produces plastic deformations around the sleeve-bolt interface, providing a sticking condition between the sleeve and the bolt. Since the nut seats on the same sleeve body, the relative sliding effect between the bolt and the does not become minimal.

Before starting the full model analyses, simplified rough models were built up to make proper guesses in sleeve height. The model was described as 2D axisymmetric. Therefore, all geometric components were cylindrical parts. The geometrical dimensions are defined below:

Each plate had 4.16 mm of thickness, and the inner diameter was 8 mm. Washers had an 8 mm inner diameter and 15 mm outer diameter with 1 mm thickness. Insert material had a 6 mm inner diameter with 0.2 mm wall thickness and 9.32 mm height. The sleeve flange diameter was 12.72 mm, and there was 0.02 mm clearance between the insert and the sleeve shaft. The wall thickness of the sleeve was 0.2 mm. The lower die shaft feature was 0.02 mm thinner than the sleeve inner diameter with 0.5 degrees of taper angle from the bottom up. The height of the sleeve started from 12.9 mm and decreased gradually depending on the forming and ductile damage results.

The 2D axisymmetric analysis method was chosen to reduce computational cost while calculating the optimum sleeve geometry. The 2D analyses comprised two rigid bodies (punch, lower die), four elastic bodies (insert, top and bottom plates with washers), and an elastic-plastic sleeve material. Since the composite plates were not being analyzed, the material of the top and bottom plates was chosen as isotropic steel, having Young's modulus of 0.1 GPa and Poisson's ratio of 0.3. All thermal effects were neglected in the finite elements analyses. The sleeve material parameters were taken from (Erbil & Karakuzu, 2023) including the anisotropy and the damage properties. The washer materials were chosen as AISI 312 stainless steel, and the insert material was selected as Ti6-4. All elastic and elastic-plastic elements meshed with 10-nodes Quad elements using an advancing fronting quad mesher. The element size

for the sleeve material was 0.05 mm. The total element size was varying between 5500 and 5000.

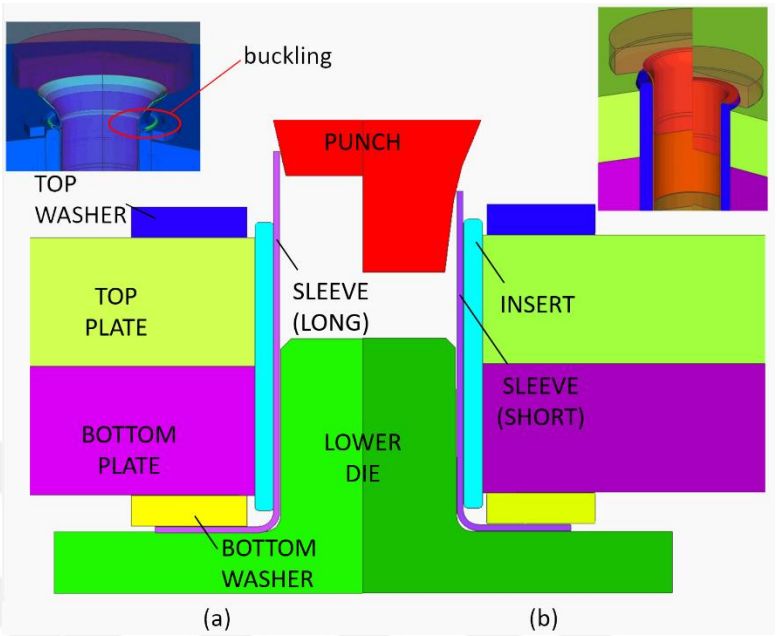

Figure 2.31 Simplified 2D pre-mature model (sleeve height optimization, a: long sleeve, b: short sleeve configuration)

According to the 2D analyses, lapping and buckling (Figure 2.31-a) with excessive damage problems (Figure 2.31-b) were observed in designs. Therefore, it was considered to form the final sleeve geometry in two stages.

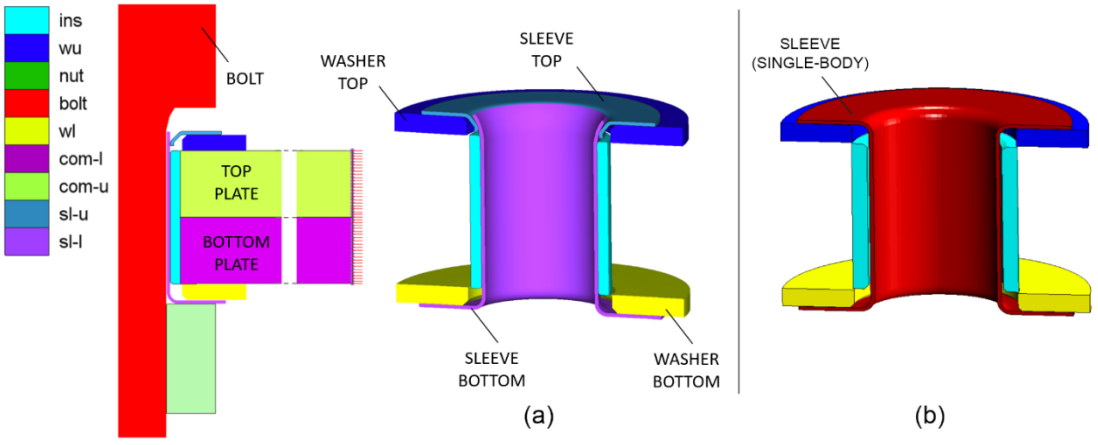

Figure 2.32 Final geometry for composite modeling (a: multi body sleeve, b: single body sleeve)

Finally, two separate models were designed. In the first design, sleeve geometry was divided into two parts, as given in Figure 2.32-a. In the second design, regardless of forming difficulties, it was assumed that a specific toolset perfectly did the plastic deformation of the sleeve geometry, and the final form was provided a complete closed form as in Figure 2.32-b.

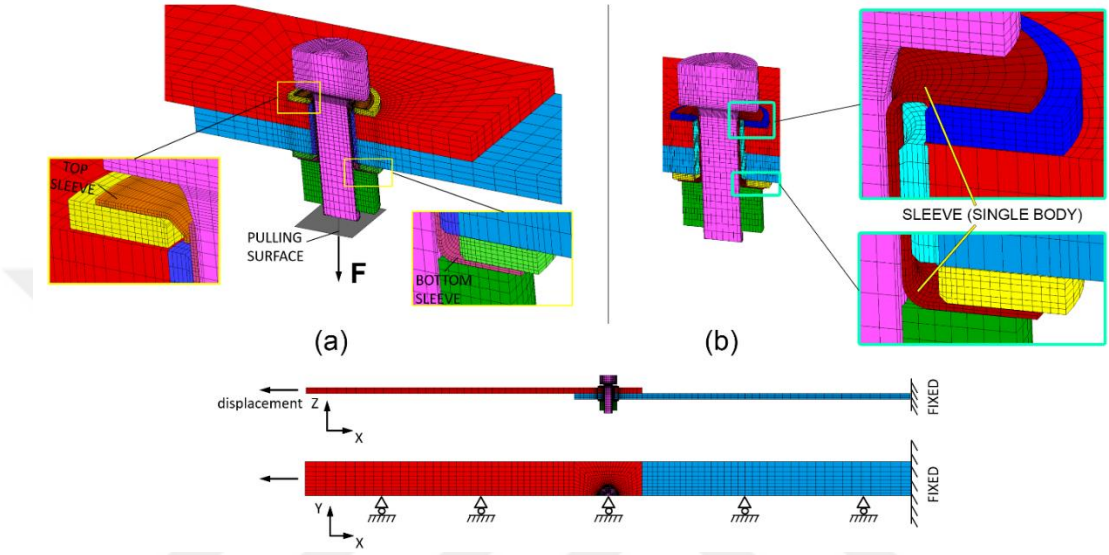

Figure 2.33 FE model of the final assembly

The full model analyses were computationally demanding. Therefore, the FE model was considered symmetrical and 3-D (Figure 2.33). All thermal effects were neglected. The model parameters are described in (Erbil & Karakuzu, 2023).

Table 2.7 Geometrical dimensions of composite plates

I-F	d (mm)	D (mm)	e/d	w/d	T (mm)	L (mm)
0.0%	8.08	8.08	3	6	4.16	243
2.1%	7.91	8.08	3	6	4.16	243

The geometrical properties of the composite plates are given in Table 2.7, where the I-F is the interference fit ratio, d is the hole diameter, D is the insert diameter, e/d is the edge distance to hole diameter, w/d is the width to hole diameter, t is the total plate thickness, and L is the full length of each plate. The analyses were carried out in

two configurations. The first is the high interference fit (2.1%) configuration, and the other is the no interference fit configuration.

Quasi-isotropic HTA/6376 lay-up was used in stacking sequence of $[(0/\pm45/90)_2]_s$. Each ply has a nominal 0.26 mm thickness. Therefore, the total thickness of each plate was 4.16 mm. Ti6-4 material was chosen for the insert material. The outer diameter of the insert was defined by Table 2.7.

Table 2.8 Tensile properties of the AISI 304L (Erbil & Karakuzu, 2023)

Angle with Rolling Direction (°)	Yield Stress (MPa)	Anisotropic coefficient r_α
0	278	0.87
45	270	1.16
90	280	0.82

The wall thickness of the insert was 0.75 mm. 0.2x45 mm chamfers were added to the insert to ease the forming operation. Materials for the top and the bottom sleeves were chosen as AISI 304L, from which the mechanical and damage parameters were taken (Erbil & Karakuzu, 2023) and (Ben Othmen et al., 2020) (Table 2.8). The Cockcroft & Latham critical damage parameter was taken as 0.52. The outer diameters of both sleeves were 13 mm. The inner diameter of the top sleeve was 6.38 mm.

Ti 6Al-4V Grade 5 Hex Head Bolt M6 x 1.0mm x 20mm was simplified and modeled without threads and head form details. The bolt was selected to be in the 6g tolerance grade and paired with a 6H M6 x 1.0mm nut. The assembly components were coupled to a 10.4 kN preload value. Therefore, 5.2 kN force was applied to the pulling surface body in Figure 2.33 FE model of the final assembly before the displacement was applied in the same figure. The tightening torque can be calculated using the equation below:

$$T = \frac{F_i\, d_m}{2}\left(\frac{1/(\pi\, d_m) + f\sec(\alpha)}{1 - f\,(1/(\pi\, d_m))\sec(\alpha)}\right) + \frac{F_i\, f_c\, d_c}{2} \tag{2.15}$$

where dm is the average of minor and major diameters of the threads, α is the half of the thread angle, fc is the friction coefficient under the bearing surface, d is the

nominal thread diameter, Fi is the preload or clamp load, f is the friction coefficient between the threads, and T is the tightening torque.

The required torque was calculated as 9.29 Nm using the equation (2.15), and 1 Nm was added for the metal-forming process of the sleeve component. Hence, the required torque would be 10.29 Nm. This value was close to the max-torque limit for the Ti6-4 Grade 5 bolt.

The material properties of HTA/6376 are given in (Table 2.1). The material nonlinearity of HTA/6376 in the shear planes was implemented to Marc via subroutine code in the md_hooklw module as explained in (Erbil & Karakuzu, 2023) (Figure 2.9). The endurance limits of CFRP material were used in the material model, as given in Table 2.3. Damage criteria were taken from the equations (2.5) to (2.11). If any of the criteria defined in equations from (2.5) to (2.11) is satisfied, the material will degrade in the corresponding direction(s). Therefore, these criteria are defined in $ufail$ subroutine code by Table 2.4. Multiple equations of matrix crushing failure for compression and tension cases are combined in one failure index per case, $f1$, and $f2$, respectively.

The compliance matrix can be changed by md_hooklw when necessary. The nonlinearity of the shear modulus was applied using a compliance matrix regarding the methods explained above in the previous sections. The reduction factors were taken from (Table 2.5) for material degradation.

The Fortran flow chart in Figure 2.12 reveals the execution procedure of the method in Marc. The composite plates were assumed to have four layers each, while each layer had four laminas. A total of 40422 elements were generated. 8928 type-149 elements with 12110 nodes for composite plates, 3456 type-7 elements with 4403 nodes for insert, 11910 type-7 elements with 13803 nodes for bolt, 2520 type-7 elements with 3256 nodes for nut, 6912 type-7 elements with 8806 nodes for both washers, 2952 type-7 elements with 4662 nodes for top sleeve, 3744 type-7 elements with 5883 nodes for bottom sleeve were used in the analyses.

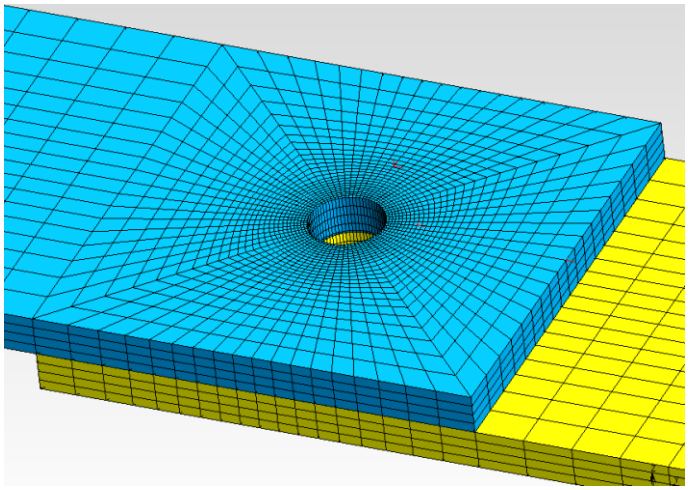

Figure 2.34 Mesh density of composite plates

The minimum element edge length around the hole was measured as 0.026 mm in the smallest radius of the top sleeve. Mesh densities of the plates are given in Figure 2.34.

Since the Stick-Slip method was not converged in the process, apart from (Erbil & Karakuzu, 2023) bilinear (Coulomb) friction was used for simulating the friction behavior. The friction force tolerance value was set to 0.1. Single-sided contact was used in the analyses. The contact tolerance was set to 0.01, and a 0.9 bias factor was activated.

In the post-processor stage, a unique code was implemented to store the minimum values of reduction ratios for each sublayer of every element, which was calculated per integration point, as shown in Figure 2.12. A total of 6 reduction ratios representing the reduction in E_{11}, E_{22}, E_{33}, G_{12}, G_{23}, and G_{31}, respectively, stored in the user-defined post variable, “v.” The seventh and the last post variable stores the minimum value of all other 6-reduction ratios, indicating the weakest link in any of the stress components.

In this chapter, fundamental concepts for the final model were revealed. The methods and post-processing procedures were developed for the subsequent chapters. Brief information was provided regarding the sleeve geometrical form. It was concluded that the multi-stage configuration might apply to further analyses.

CHAPTER THREE
RESULTS AND DISCUSSION

3.1 Progressive damage results for the composite model

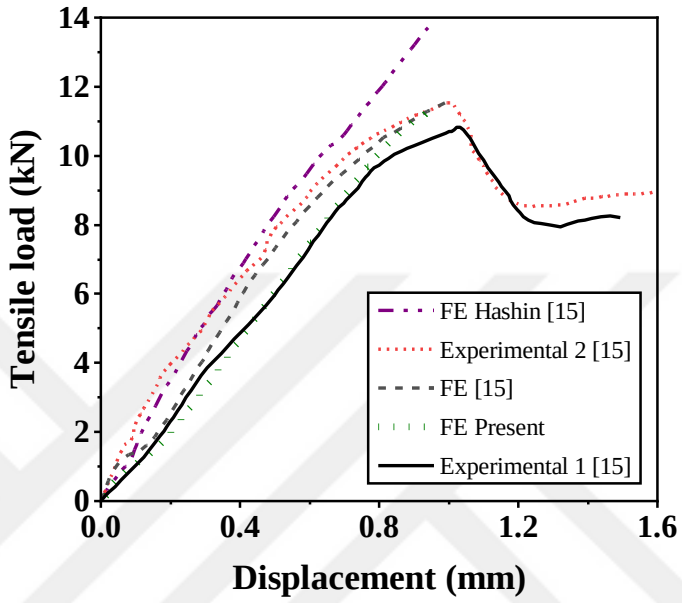

Figure 3.1 Bolted composite plate force-displacement results

The results of load-displacement curves in Figure 3.1 show that present FE results represent the worst-case scenario for damage initiation. This could be beneficial for safety reasons.

Advanced PLOTV function was used to assist with Python in the postprocessing stage. Conventionally, Marc can plot only one layer at a time if one element consists of two or more elements. Therefore, the visual is limited to the actual number of elements in the analysis. In other words, sub-elements are not plotted, or existing elements are not divided into two or more elements to plot every sublayer simultaneously. With the subroutine code, it was possible to monitor sublayer damages by transferring data to Python and process in another environment. Eventually, each failure indices plotted in Figure 2.25 layer-by-layer, where each element consisted of

multiple layers in different orientation angles. For example, the simulation model has four layers for composite ply. However, the plotted results have 16 layers in total.

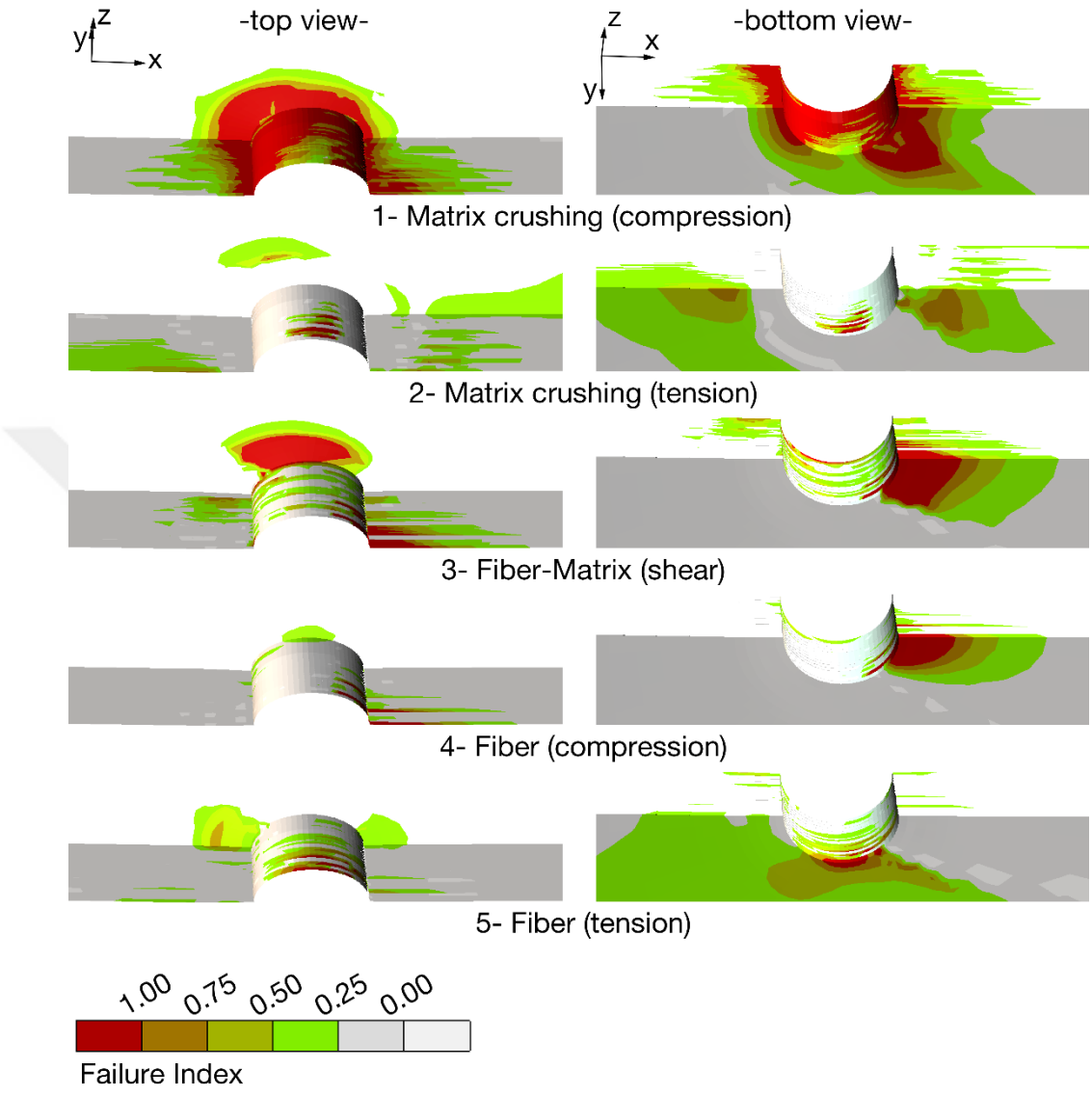

Figure 3.2 Damage results for composite plate

Damage results were computed according to Table 2.4, and the damage results were plotted in Figure 3.2.

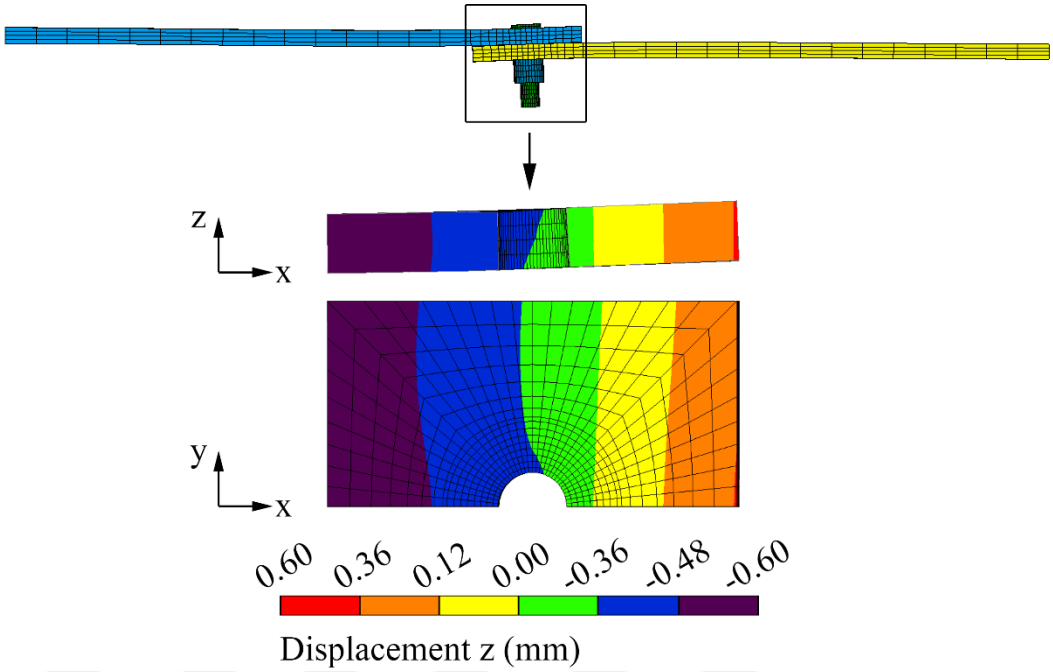

Figure 3.3 Displacement in the thickness direction at complete failure

The initiation of the secondary bending effect can also be seen in Figure 3.3. The effect improves once the lateral displacement increases.

This section evaluated and verified the composite model's progressive damage results. The results are in good agreement with the literature.

3.2 Ductile damage results for the sleeve part

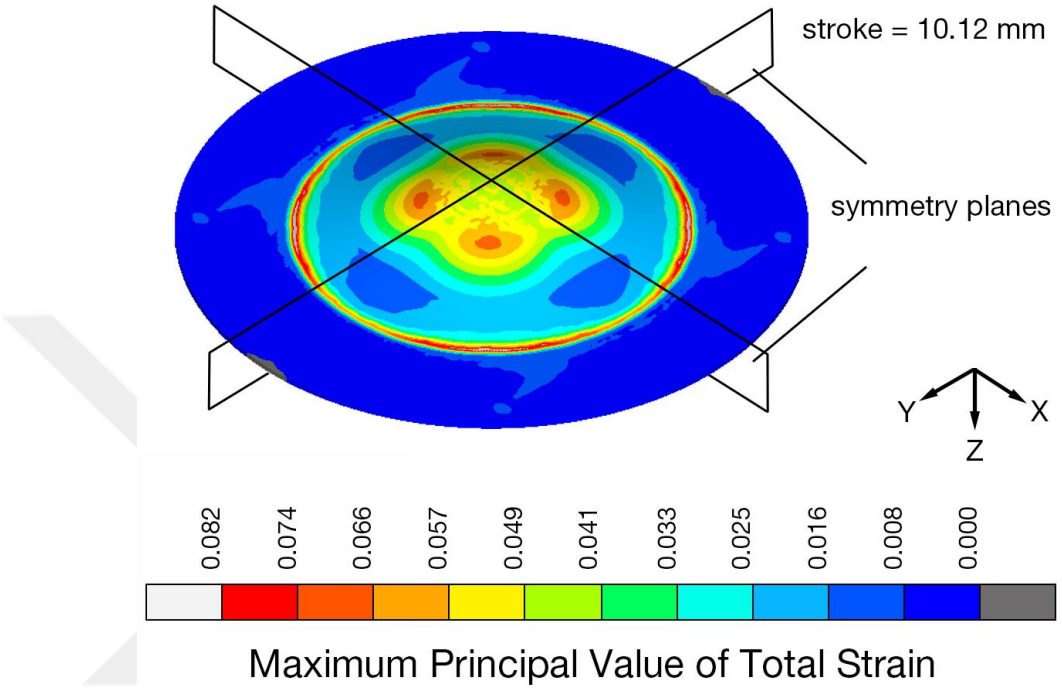

Figure 3.4 Strain distribution of the ¼ symmetrical model

Since the re-meshing strategy was not the same as in (Ben Othmen et al., 2020), slightly coarser mesh finally caused radially non-homogeneous strain distribution near symmetry planes in the resulting plot Figure 3.4. However, the whole model is perfectly compatible with a 2-D and axisymmetric type of analysis. Moreover, it is computationally more efficient and gives smoother result plots.

Hence, the verification model was converted to a 2D axially symmetric model. The axisymmetric 2-D model, “Element 10”, a 4-node quadrilateral element with 2 DOF in the z and r directions per node, is used. 1753 and 2077 nodes were used in the analysis.

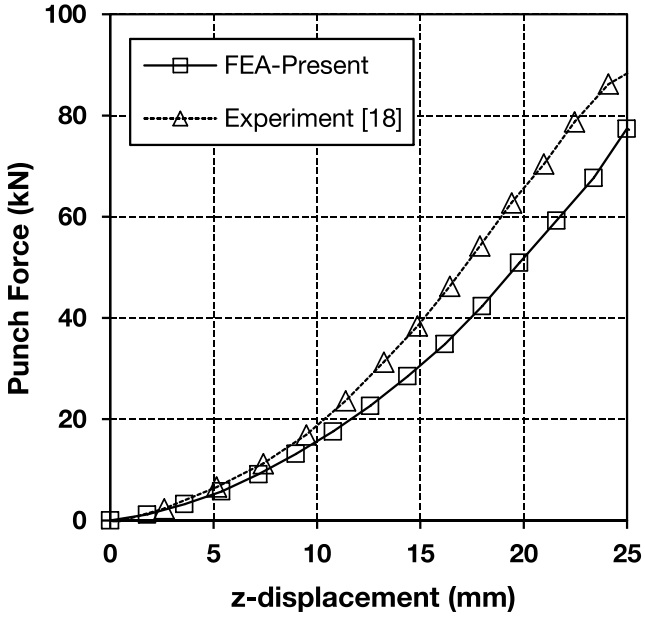

Figure 3.5 Cupping force-displacement history

The punch force vs displacement curve in Figure 3.5 is close to the experiment.

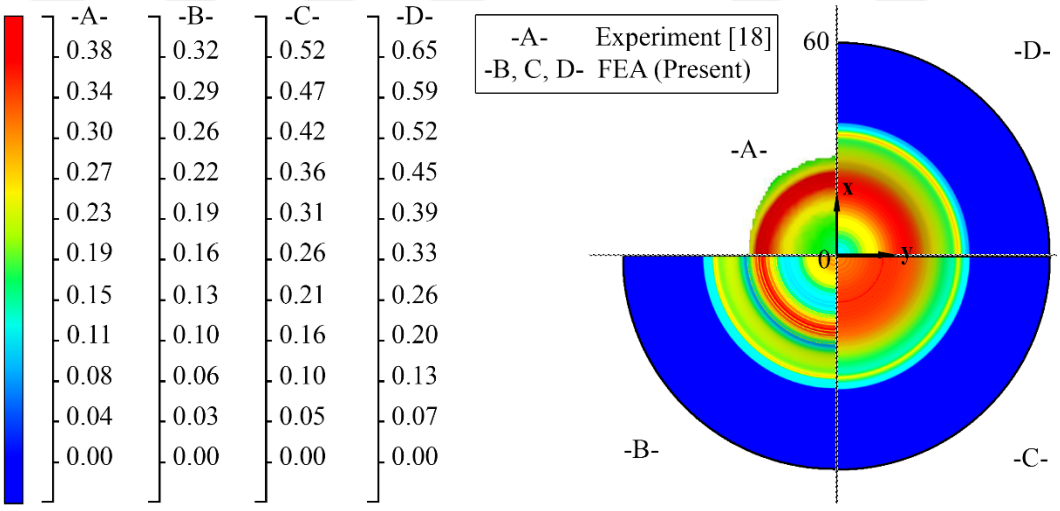

Figure 3.6 Scalar results of Erichsen cupping test, total strain (A), major strain (B, glued), Cockroft-Latham damage index (C, glued), and maximum principal strain (D, glued) at the rupture stoke, 25 mm

The maximum principal stress result of the experiment and the finite element analysis was overlapped and reasonably conforming in Figure 3.6. The results in

Figure 3.6 agree with (Ben Othmen et al., 2020). Marc FEA results of max. Principal total strain reaches up to 0.38 Figure 3.6 when the rupture begins.

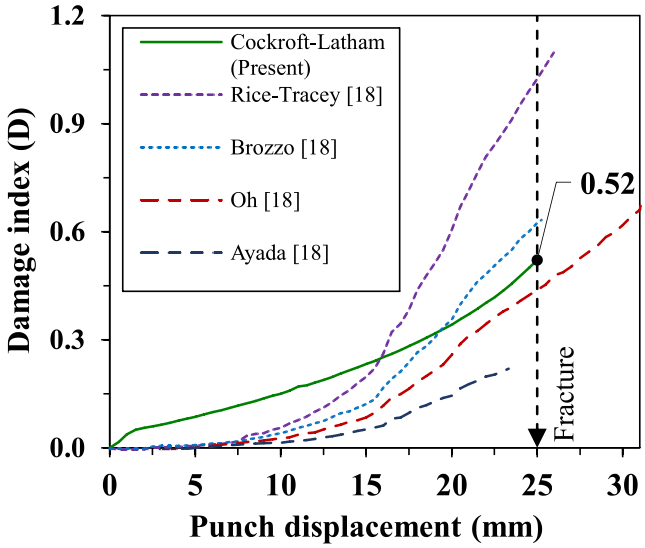

Figure 3.7 Damage indices of Cockroft & Latham (present, glued), Rice-Tracey, Brozzo, Oh, and Ayada (combined with data in (Ben Othmen et al., 2020))

The Cockroft & Latham damage parameter at the rupture stroke is 0.52. The damage parameters for the other models are extracted from (Ben Othmen et al., 2020) and replotted in Figure 3.7.

This section computed the Cockroft-Latham threshold damage index value for AISI 304L sheet metal material using FEA. Numerical and experimental sources in literature verified the results of the analyses. The material models and the simulation parameters could be used in subsequent design studies.

3.3 Results for the final model

Table 3.1 FE analysis configuration plan

Config. #	Code	I-F (%)	Clamp load (kN)	Clamp grade	Sleeve configuration: Multi body (M)	Sleeve configuration: Single body (S)	Sleeve configuration: No sleeve (N)
1	00N-Low	0.00	10.31	Low			X
2	00M-Low	0.00	10.45	Low	X		
3	21N-Low	2.10	10.40	Low			X
4	21M-Low	2.10	10.44	Low	X		
5	21N-Med	2.10	13.68	Medium			X
6	21S-High	2.10	15.81	High		X	

** Coding: I-F percent x 10 (00-21) + sleeve configuration (M-S-N) + clamp grade (Low-Med-High)*

To understand the effects of sleeve configurations mentioned above, analysis models were set as given in Table 3.1. In this table, the clamp load indicates the exact retaining clamping load after removing the pulling surface in Figure 2.33.

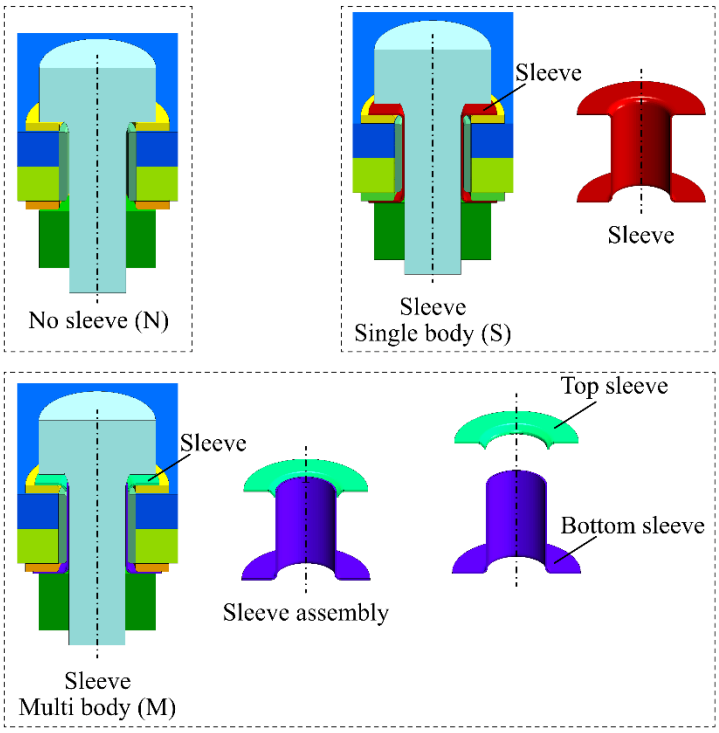

Figure 3.8 Sleeve configurations (see Figure 2.32 for details)

The codes related to the configuration numbers in Table 3.1 are explained in the Figure 3.8.

There was expected to be a decrease in clamp load due to the elastic back-stresses once the pulling surface was disconnected. Hence, an additional load step was added for one second to control the glue condition between the nut and the bolt to ensure the stability of the clamp load. Therefore, the resultant clamp load values are not exactly the same as in the FE load-case setup.

21N-Med was planned to have the same clamping load as 21S-High in Table 3.1. However, it was observed in the results that the critical damage limit was already exceeded in 21N-Med. Then, it was decided not to increase the clamp load more for comparison.

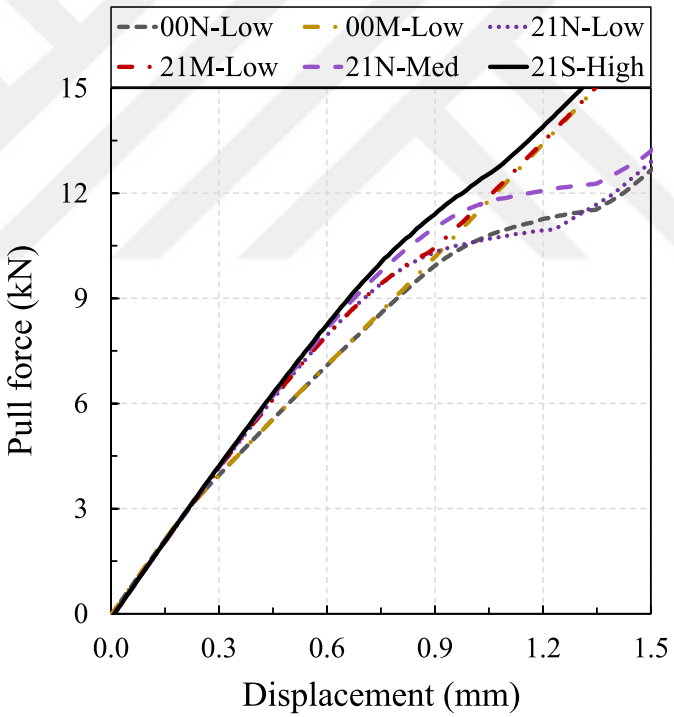

Figure 3.9 Bearing response of configurations under lateral pull-force

Analyses were evaluated up to 12 kN of lateral pull force value (Figure 2.33, displacement in the -x direction) to avoid the effects of catastrophic damage mechanism (Figure 3.9).

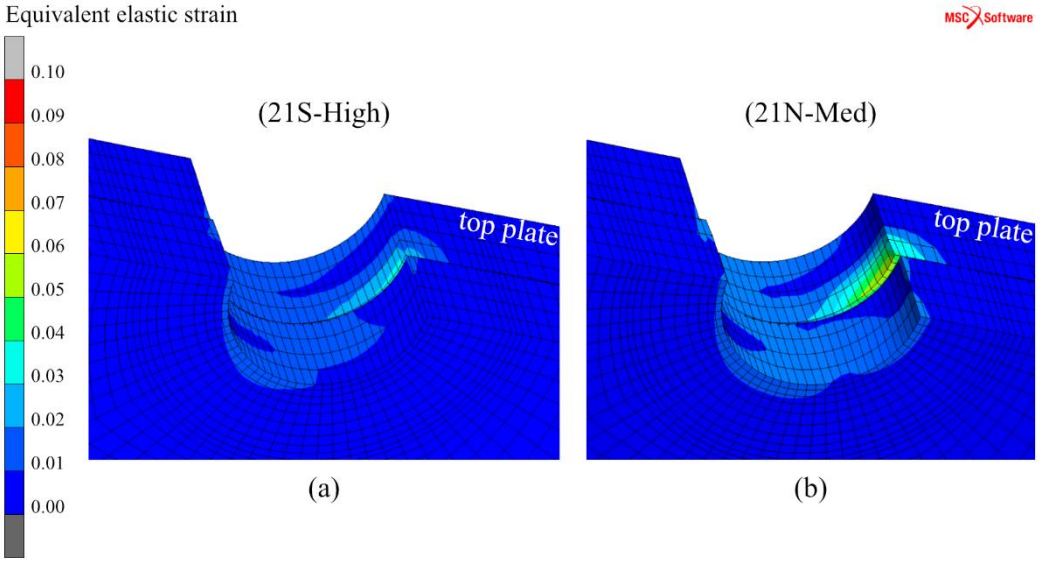

Figure 3.10 Distribution of the equivalent elastic strains at 12 kN of lateral pull force: (a) single body sleeve 21S-High, (b) no sleeve 21N-Med

Before detailing the results, it was observed in the analysis that the elastic strains in the region of contact between the top plate and the insert were approximately two times higher in 21N-Med than in 21S-High (Figure 3.10). The reason for this can be explained in Figure 2.30.

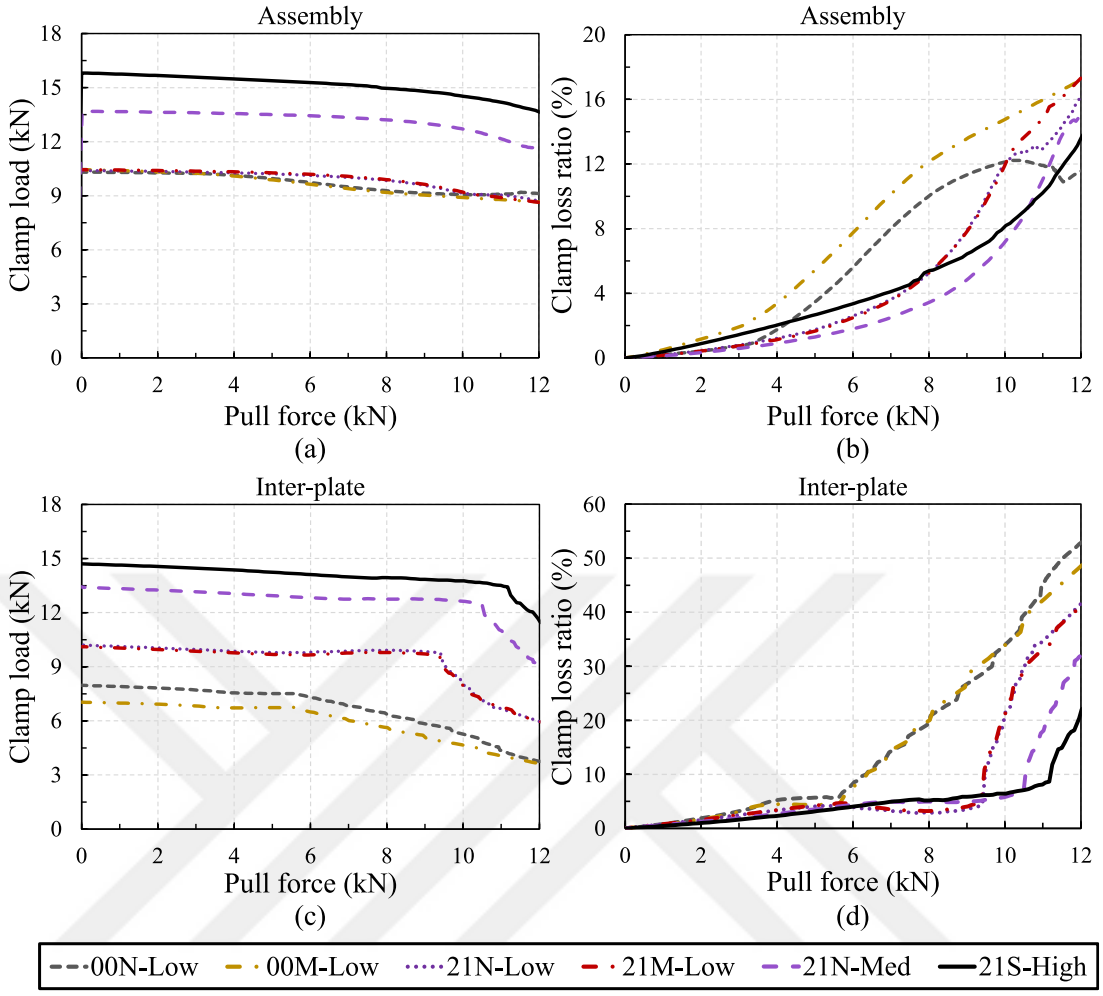

Figure 3.11 (a) Assembly clamp load, (b) assembly clamp loss, (c) inter-plate clamp load, (c) inter-plate clamp loss changes under lateral pull force.

Preserving the clamp load is crucial for the stability of joint design. The clamp load is calculated based on the normal force action on the bolt and the nut. However, because of the bending moment and the frictional or shear forces, the clamping force may travel inside the composite material in lateral directions. Therefore, regarding the Figure 3.11, the neat clamp force reacting on the contact normal surfaces of the adjacent composite plates may provide more reliable measures.

Table 3.2 Assembly and inter-plate clamp loss of assembly configurations

	Assembly			Inter-Plate		
Code	Clamp Load (kN)	Clamp Loss (%)	Improvement	Clamp Load (kN)	Clamp Loss (%)	Improvement
00N-Low	10.31	11.59	33%	7.97	53.02	0%
00M-Low	10.45	17.22	0%	7.04	48.66	8%
21N-Low	10.40	16.19	6%	10.22	41.68	21%
21M-Low	10.44	17.24	0%	10.12	40.84	23%
21N-Med	13.68	15.01	13%	13.41	31.98	40%
21S-High	15.81	13.69	21%	14.70	22.04	58%

According to Table 3.2 and Figure 3.3 results, the applied clamp force is not transferred directly to the composite parts. Because of the interaction between assembly components, some load was transferred to other members besides the composite plates. Align with this statement; it was observed that the increase in clamping load provides more load to share with adjacent composite plates. As in Table 3.2, adding multi-body or single-body sleeves can improve the stability of the inter-plate clamping load. Consequently, the inter-plate clamping load improved by 58 % compared with the net fit without sleeves.

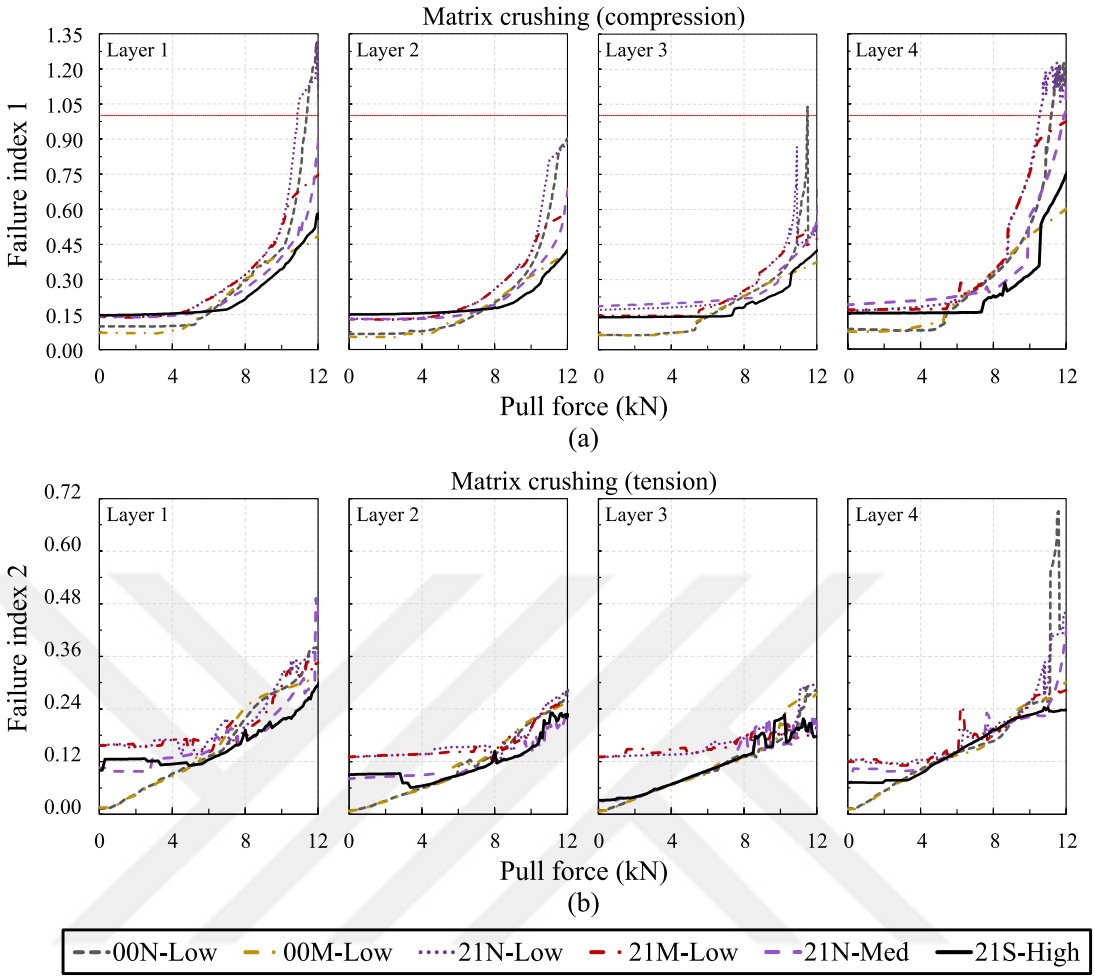

Figure 3.12 Matrix damage under pull force: (a) compression, (b) tension

The matrix damage results are plotted in Figure 3.12. Since the plots focused on the localized damage values, damage initiation in configuration 6 (21S-High) could be seen as starting earlier, but 21S-High withstands higher pull force until the catastrophic damage limit. It can be seen in Figure 3.12 that some minor matrix damages occur in several layers during the interference fitting operation before the lateral pulling process. The effects of high interference between the insert and the composite parts can explain this. Besides that, it was known in the literature that minor localized damages may improve joint stiffness, as described in the introduction.

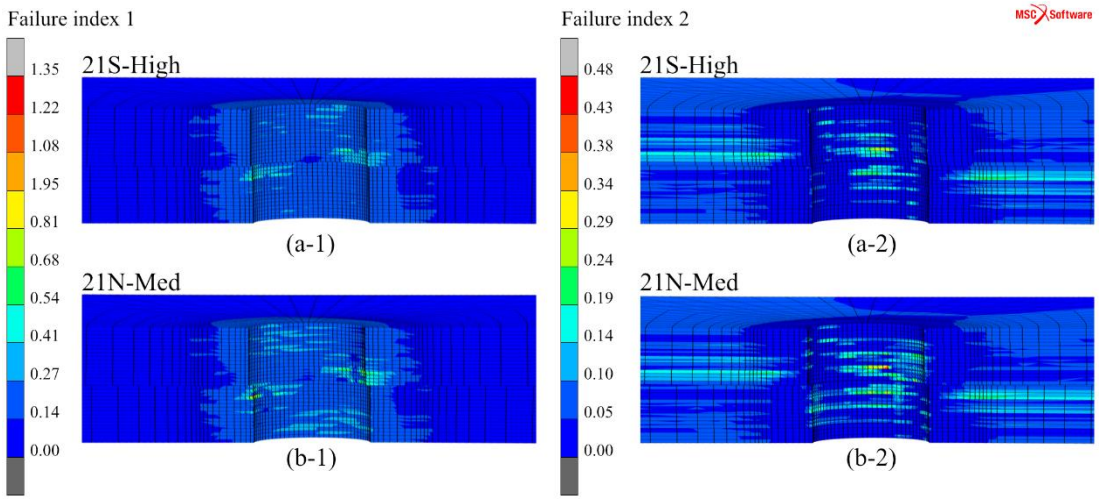

Figure 3.13 Failure indices 1 (a-1, b-1) and 2 (b-1, b-2) represent the matrix crushing compression and tension, respectively

The layer-by-layer results showed in Figure 3.13 that the damage pattern in 21S-High was similar to the 21N-Med. However, it can be seen that the single-body sleeve in 21S-High reduces the bearing damage by providing a stable inter-plate clamping force.

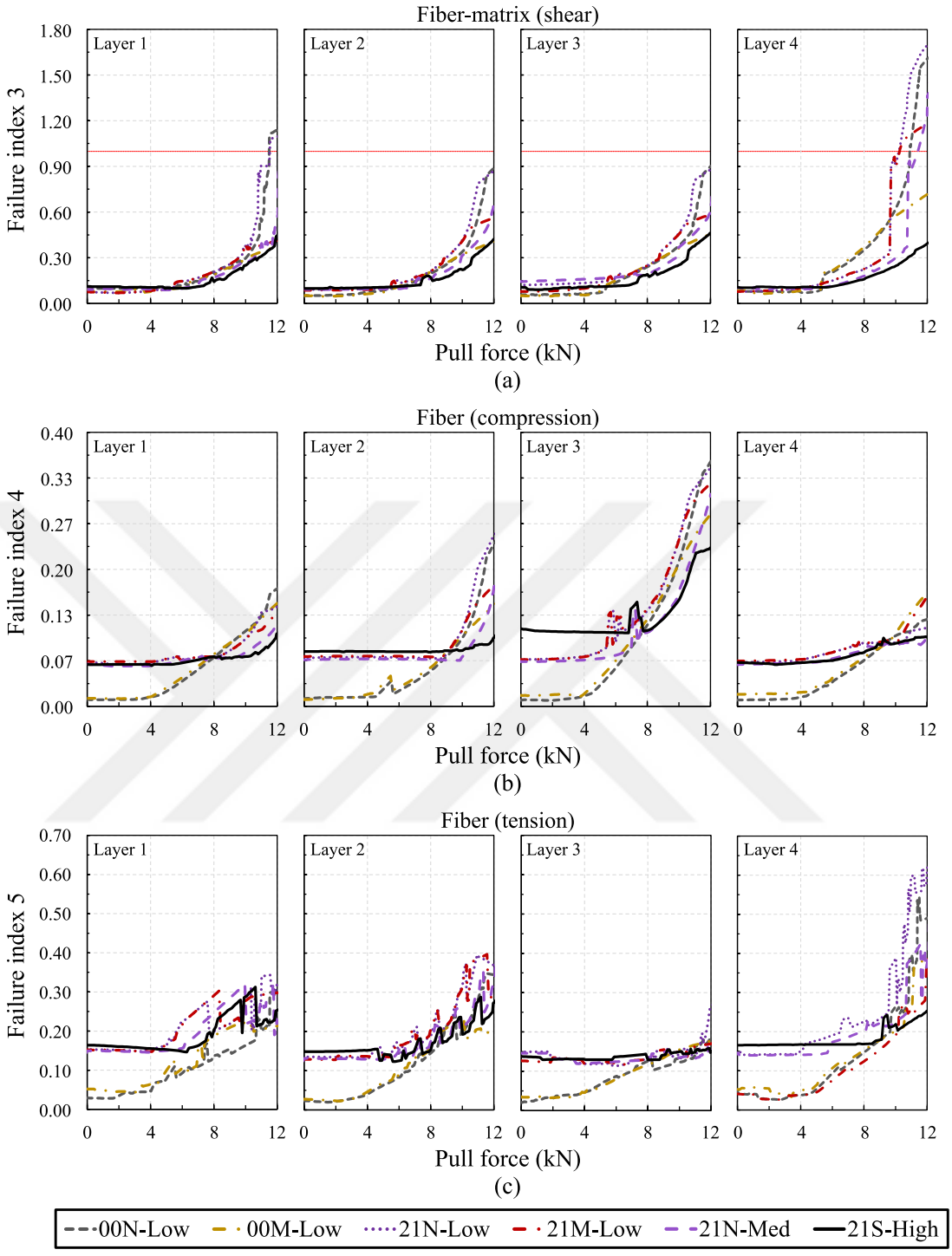

Figure 3.14 Fiber damage under pull force: (a) shear, (b) compression, (c) tension

The fiber failure indices in Figure 3.14 show that layer 4 fails because of fiber-matrix shear damage in most configurations except for the 21S-High and the 00M-Low. As expected, the initial compressive fiber damage values were higher in

interference fit configurations than in neat fit configurations. Some of the benefits related to these minor damages were explained above.

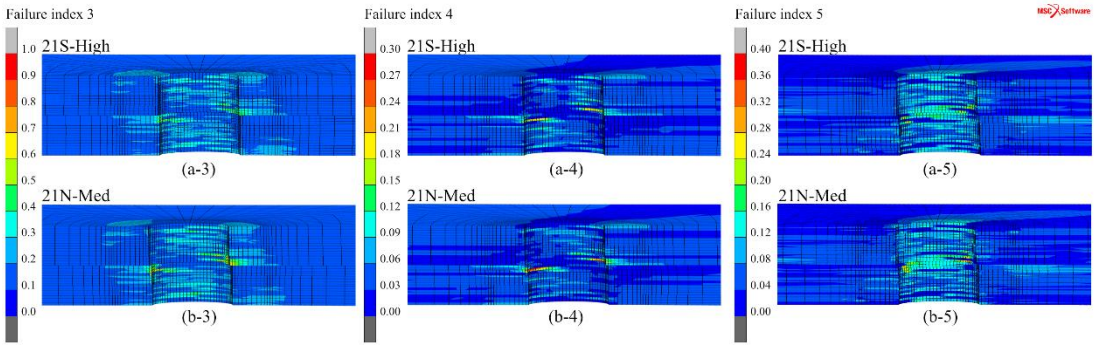

Figure 3.15 Failure indices 3 (a-3, b-3), 4 (a-4, b-4), and 5 (b-5, b-5) represent the fiber-matrix (shear), fiber (compression), and fiber (tension), respectively

Figure 3.15 (b-4) shows major damage values near the top/bottom plates and the insert interface region.

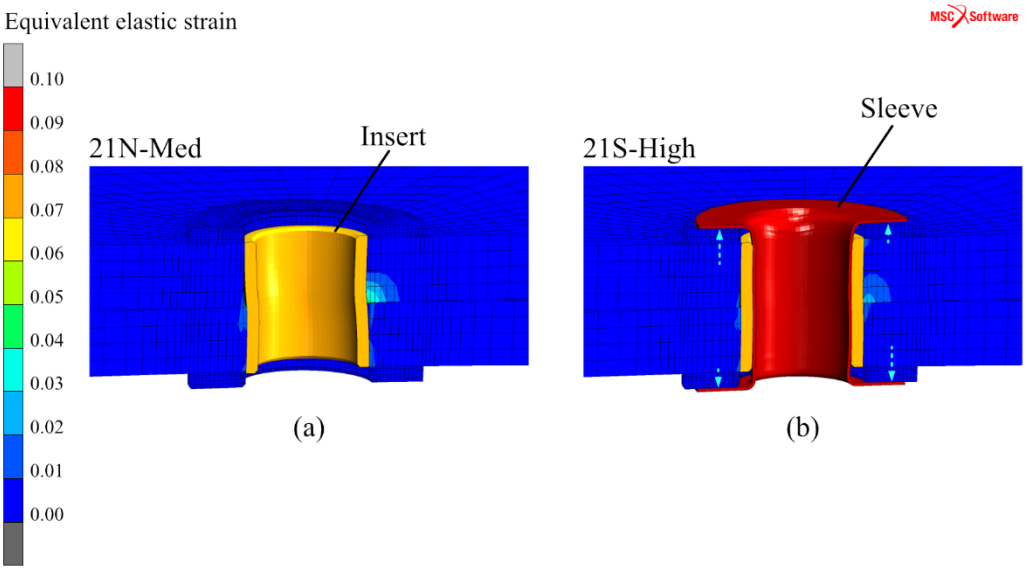

Figure 3.16 Equivalent elastic strain concentration at 12 kN of lateral pull load

The claim in Figure 2.30 was supported in Figure 3.15 and Figure 3.16 that the residual stresses on the sleeve help stabilize nonuniform stress distribution during

bending conditions. It was also observed that the 21S-High configuration doesn't exceed the critical damage limit.

Table 3.3 Assembly and inter-plate clamp loss of assembly configurations.

	Maximum damage indices for all 4 layers									
	Matrix Crushing (compression)		Matrix Crushing (tension)		Fiber-Matrix (shear)		Fiber (compression)		Fiber (tension)	
Code	Failure Index 1	Improvement	Failure Index 2	Improvement	Failure Index 3	Improvement	Failure Index 4	Improvement	Failure Index 5	Improvement
00N-Low	1.22	0%	0.43	10%	1.61	5%	0.36	0%	0.49	21%
00M-Low	0.60	51%	0.31	34%	0.72	57%	0.28	21%	0.39	37%
21N-Low	1.18	3%	0.46	3%	1.69	0%	0.35	3%	0.62	0%
21M-Low	0.97	20%	0.34	27%	1.17	31%	0.32	9%	0.38	39%
21N-Med	1.14	7%	0.47	0%	1.37	19%	0.31	13%	0.38	40%
21S-High	0.75	38%	0.30	37%	0.46	73%	0.23	35%	0.27	56%

The failure indices were concluded in Table 3.3 by taking the maximum damage values of all layers for each failure index. It can be seen in Table 3.3 that the damage was significantly reduced in the 21S-High configuration.

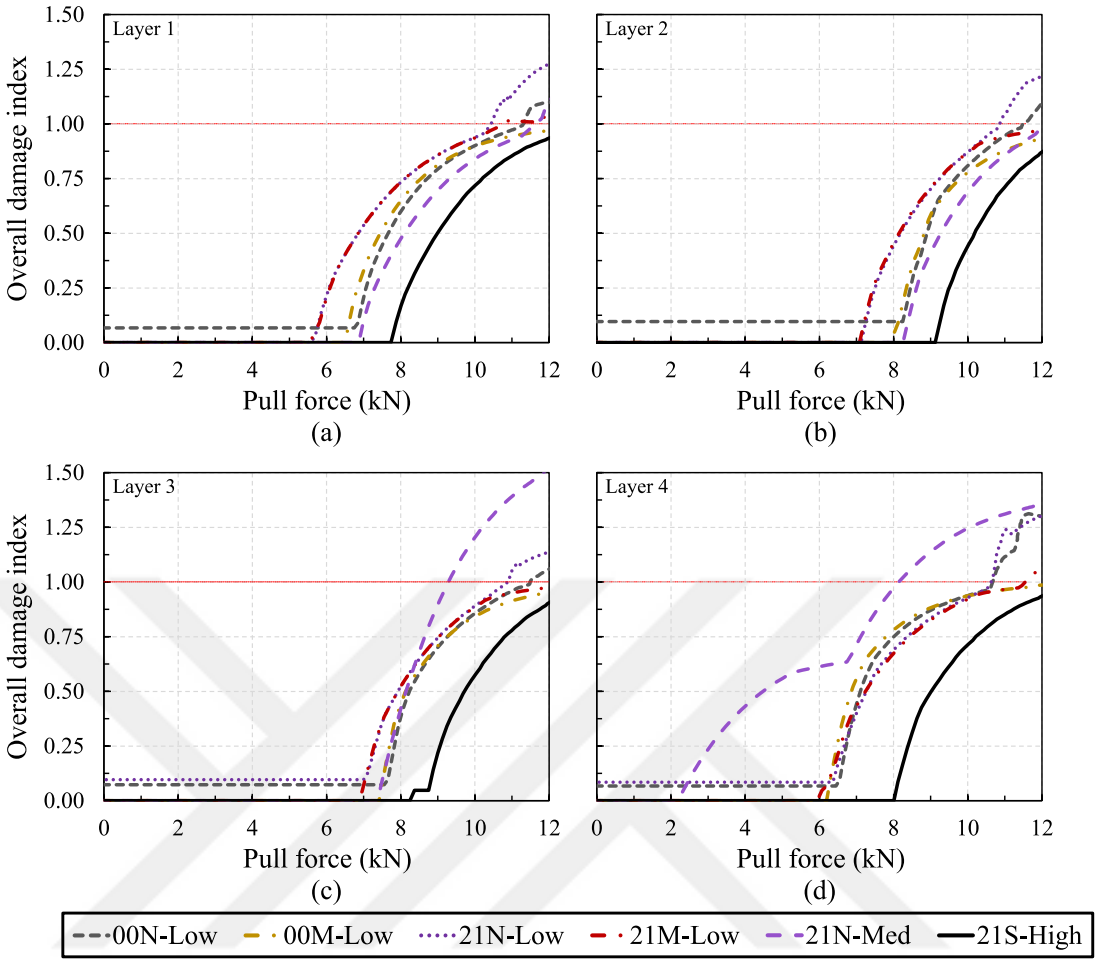

Figure 3.17 Overall damage indices under 12 kN pull force at layers 1 to 4 (a to d)

The overall damage values are plotted in Figure 3.17. It can be seen that the catastrophic damage event starts after 10 kN of lateral load.

Severe bearing damage at layer 4 occurs in the 21N-Med configuration after 6 kN of lateral load. The damage starts at the lower lateral pull force for the 21N-Med configuration.

Table 3.4 Effects of assembly configuration on damage initiation force and max. damage.

	Layer 1				Layer 2				Layer 3				Layer 4			
Code	Initiation (F-kN)	Improvement	Max Damage	Improvement	Initiation (F-kN)	Improvement	Max Damage	Improvement	Initiation (F-kN)	Improvement	Max Damage	Improvement	Initiation (F-kN)	Improvement	Max Damage	Improvement
00N-Low	6.60	18%	1.07	3%	8.10	16%	1.11	1%	7.50	7%	1.07	29%	6.40	178%	1.07	21%
00M-Low	6.40	14%	0.99	10%	8.00	14%	0.98	13%	7.50	7%	0.99	35%	6.20	170%	0.99	27%
21N-Low	5.60	0%	1.10	0%	7.00	0%	1.13	0%	7.10	1%	1.07	29%	6.20	170%	1.30	4%
21M-Low	5.60	0%	1.05	4%	7.00	0%	0.98	13%	7.00	0%	0.98	36%	5.90	157%	1.06	21%
21N-Med	7.00	25%	1.10	0%	8.20	17%	0.97	14%	7.50	7%	1.52	0%	2.30	0%	1.35	0%
21S-High	7.70	38%	0.94	15%	9.10	30%	0.87	22%	8.20	17%	0.91	40%	8.00	248%	0.94	31%

The results in Table 3.4 show that the overall damage initiation force was significantly improved in the 21S-High configuration. The Layer 4 damage resistance has the capability of all other configurations.

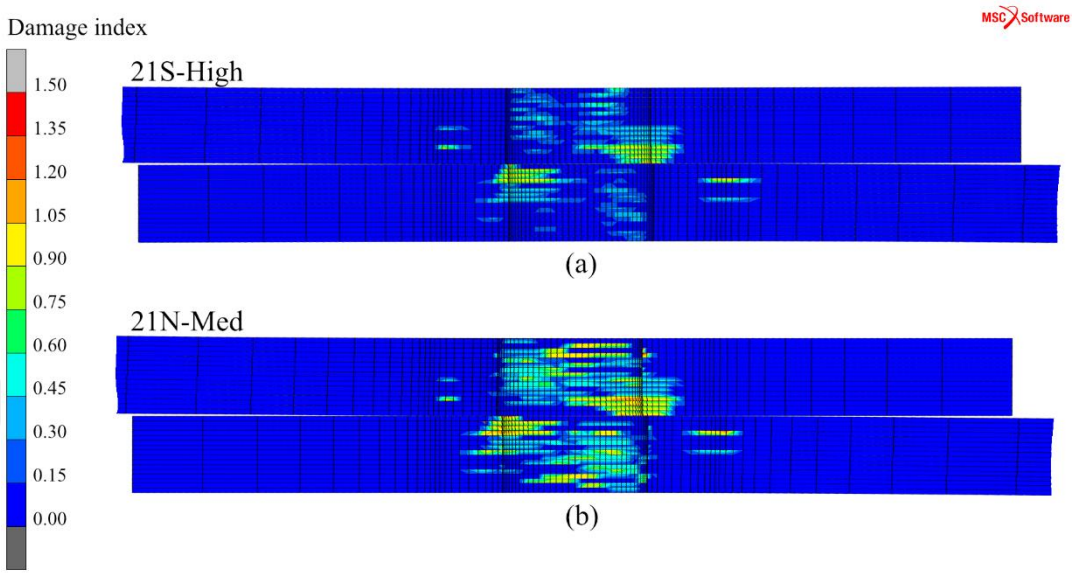

Figure 3.18 Overall damage under 12 kN pull force: (a) 21S-High, (b) 21N-Med

The layer-by-layer damage plots are given in Figure 3.18. The damage pattern at the bearing surface of 21S-High has a less concentrated distribution than the 21N-Med configuration.

CHAPTER FOUR
CONCLUSION

This thesis describes the fundamental analyses of single-lap bolted composite joints using the aerospace industry's common materials. Case-specific codes were developed in this thesis using Fortran and Python for batch modeling. These pseudo-codes could be used for autonomous parametric modeling purposes in further studies. The postprocessing ability of Marc was improved for damage visualization. The threshold value of the Cockroft–Latham damage index was obtained for AISI 304L sheet metal material.

The proposed model was analyzed with and without sleeve geometry. It was shown that the residual stresses, which are the products of in-situ plastic deformation on sleeve material, can help reduce the effect of bending moment in all directions.

In the single-body 21S-High configuration, the remaining residual stresses after the metal forming operation significantly improved the clamp load capability of the joint. Similarly, the 21S-High configuration maintained the clamp load at high uniaxial loads up to 12 kN.

A single-body sleeve significantly reduced inter-plate contact stresses, especially near the bolt-hole region, compared to a sleeveless joint.

In the 21S-High configuration, the failure indices were reduced by 16% to 54%, the damage initiation force was improved by 8% to 40%, and the inter-plate clamp loss was reduced by 18% compared to the most similar configuration, 21N-Med. The bearing response and stiffness significantly increased with the proposed model.

REFERENCES

Abe, Y., Kato, T., Mori, K.-i., & Nishino, S. (2014). Mechanical clinching of ultra-high strength steel sheets and strength of joints. *Journal of Materials Processing Technology*, *214*(10), 2112-2118. https://doi.org/10.1016/j.jmatprotec.2014.03.003

Akbarpour, S., & Hallström, S. (2020). Strength improvement of bolted joints in composite materials by use of patched metal inserts. *Composite Structures, 252*, 112628. https://doi.org/10.1016/j.compstruct.2020.112628

Akterskaia, M., Camanho, P. P., Jansen, E., Arteiro, A., & Rolfes, R. (2019). Progressive delamination analysis through two-way global-local coupling approach preserving energy dissipation for single-mode and mixed-mode loading. *Composite Structures, 223*, 110892. https://doi.org/10.1016/j.compstruct.2019.110892

American Society for Testing and Materials International. (2013). *Standard Test Method for In-Plane Shear Response of Polymer Matrix Composite Materials by Tensile Test of a ±45° Laminate, ASTM D3518/D3518M-13*. American Society for Testing and Materials International. https://doi.org/10.1520/D3518_D3518M-13

Awadhani, L., & Bewoor, A. (2018). Parametric study of composite bolted joint under compressive loading. *Procedia Manufacturing, 22*, 186-195. https://doi.org/10.1016/j.promfg.2018.03.029

Balawender, T., Sadowski, T., & Golewski, P. (2012). Numerical analysis and experiments of the clinch-bonded joint subjected to uniaxial tension. *Computational Materials Science, 64*, 270-272. https://doi.org/10.1016/j.commatsci.2012.05.014

Barnes, T. A., & Pashby, I. R. (2000). Joining techniques for aluminium spaceframes used in automobiles: Part II — adhesive bonding and mechanical fasteners. *Journal of Materials Processing Technology, 99*(1–3), 72-79. https://doi.org/10.1016/S0924-0136(99)00361-1

Behrens, B. A., Rolfes, R., Vucetic, M., Reinoso, J., Vogler, M., & Grbic, N. (2014). Material Modelling of Short Fiber Reinforced Thermoplastic for the FEA of a

Clinching Test. *Procedia CIRP, 18*, 250-255. https://doi.org/http://dx.doi.org/10.1016/j.procir.2014.06.140

Ben Othmen, K., Haddar, N., Jegat, A., Manach, P.-Y., & Elleuch, K. (2020). Ductile fracture of AISI 304L stainless steel sheet in stretching. *International Journal of Mechanical Sciences, 172*, 105404. https://doi.org/10.1016/j.ijmecsci.2019.105404

bigHead, C. (2023, 8 1). *Using bigHeads with composite materials*. bigHead: https://www.bighead.co.uk/bighead-fastening-solutions/bighead-core-range-of-products/

Canal, L., González, C., Segurado, J., & Llorca, J. (2012). Intraply fracture of fiber-reinforced composites: Microscopic mechanisms and modeling. *Composites Science and Technology, 72*(11), 1223-1232. https://doi.org/10.1016/j.compscitech.2012.04.008

Cao, Y., Cao, Z., Zhao, Y., Zuo, D., & Tay, T. (2020). Damage progression and failure of single-lap thin-ply laminated composite bolted joints under quasi-static loading. *International Journal of Mechanical Sciences, 170*, 105360. https://doi.org/10.1016/j.ijmecsci.2019.105360

Chen, C., Zhao, S., Han, X., Cui, M., & Fan, S. (2016). Optimization of a reshaping rivet to reduce the protrusion height and increase the strength of clinched joints. *Journal of Materials Processing Technology, 234*, 1-9. https://doi.org/10.1016/j.jmatprotec.2016.03.006

Chen, C., Hu, D., Liu, Q., & Han, X. (2018). Evaluation on the interval values of tolerance fit for the composite bolted joint. *Composite Structures, 206*, 628-636. https://doi.org/10.1016/j.compstruct.2018.08.062

Choi, J.-I., Hasheminia, S., Chun, H.-J., Park, J.-C., & Chang, H. (2018). Failure load prediction of composite bolted joint with clamping force. *Composite Structures, 189*, 247-255. https://doi.org/10.1016/j.compstruct.2018.01.037

Collings, T. A. (1982). On the bearing strengths of CFRP laminates. *13*(3), 241-252. https://doi.org/10.1016/0010-4361(82)90006-4

Dawei, Z., Qi, Z., Xiaoguang, F., & Shengdun, Z. (2018). Review on Joining Process of Carbon Fiber-Reinforced Polymer and Metal: Methods and Joining Process. *Rare Metal Materials and Engineering, 47*(12), 3686-3696. https://doi.org/10.1016/S1875-5372(19)30018-9

Ekh, J., Schön, J., & Zenkert, D. (2013). Simple and efficient prediction of bearing failure in single shear, composite lap joints. *Composite Structures, 105*, 35-44. https://doi.org/10.1016/j.compstruct.2013.04.038

Erbil, E., & Ince, U. (2011, 8). *Turkey Patent No. TR 2011 08124 A2.*

Erbil, E., & Karakuzu, R. (2023). Fastening solutions on composite structures: model and verifications of contact with friction, progressive composite damage, and ductile metal damage. *Modelling and Simulation in Materials Science and Engineering, 31*(5), 55007. https://doi.org/10.1088/1361-651X/acd70d

Fotouhi, M., Damghani, M., Leong, M., Fotouhi, S., Jalalvand, M., & Wisnom, M. (2020). A comparative study on glass and carbon fibre reinforced laminated composites in scaled quasi-static indentation tests. *Composite Structures, 245*, 112327. https://doi.org/10.1016/j.compstruct.2020.112327

Friedrich, C., & Hubbertz, H. (2014). Friction behavior and preload relaxation of fastening systems with composite structures. *Composite Structures, 110,* 335-341. https://doi.org/10.1016/j.compstruct.2013.11.024

Garnich, M. R., & Akula, V. M. K. (2008). Review of Degradation Models for Progressive Failure Analysis of Fiber Reinforced Polymer Composites. *Applied Mechanics Reviews, 62*(1). https://doi.org/10.1115/1.3013822

Gerstmann, T., & Awiszus, B. (2014). Recent developments in flat-clinching. *Computational Materials Science, 81*, 39-44. https://doi.org/10.1016/j.commatsci.2013.07.013

Giannopoulos, I. K., Doroni-Dawes, D., Kourousis, K. I., & Yasaee, M. (2017). Effects of bolt torque tightening on the strength and fatigue life of airframe FRP laminate

bolted joints. *Composites Part B: Engineering*, *125*, 19-26. https://doi.org/10.1016/j.compositesb.2017.05.059

Guerrero, J., Sasikumar, A., Llobet, J., & Costa, J. (2023). A computationally efficient methodology to simulate hybrid bolted joints including thermal effects. *Mechanics of Advanced Materials and Structures, 30*(1), 48-66. https://doi.org/10.1080/15376494.2021.2007555

Hahn, H., & Tsai, S. (1973, 1). Nonlinear Elastic Behavior of Unidirectional Composite Laminae. *Journal of Composite Materials, 7*(1), 102-118. https://doi.org/10.1177/002199837300700l

Hahn, O., Meschut, G., Bergau, M., & Matzke, M. (2014). Self-pierce Riveting and Hybrid Joining of Boron Steels in Multi-material and Multi-sheet Joints. *Procedia CIRP*, *18*, 192-196. https://doi.org/http://dx.doi.org/10.1016/j.procir.2014.06.130

He, X., Pearson, I., & Young, K. (2008). Self-pierce riveting for sheet materials: State of the art. *Journal of Materials Processing Technology*, *199*(1–3), 27-36. https://doi.org/10.1016/j.jmatprotec.2007.10.071

He, X., Zhang, Y., Xing, B., Gu, F., & Ball, A. (2015). Mechanical properties of extensible die clinched joints in titanium sheet materials. *Materials & Design*, *71*, 26-35. https://doi.org/10.1016/j.matdes.2015.01.005

Hill, R. (1998). *The Mathematical Theory of Plasticity.* Clarendon Press.

Hirsch, F., Müller, S., Machens, M., Staschko, R., Fuchs, N., & Kästner, M. (2017). Simulation of self-piercing rivetting processes in fibre reinforced polymers: Material modelling and parameter identification. *Journal of Materials Processing Technology*, *241*, 164-177. https://doi.org/10.1016/j.jmatprotec.2016.10.010

Han, L., Chrysanthou, A., & Young, K. W. (2007). Mechanical behaviour of self-piercing riveted multi-layer joints under different specimen configurations. *Materials & Design, 28*(7), 2024-2033. https://doi.org/10.1016/j.matdes.2006.06.015

Hoang, N. H., Porcaro, R., Langseth, M., & Hanssen, A. G. (2010). Self-piercing riveting connections using aluminium rivets. *International Journal of Solids and Structures*, *47*(3–4), 427-439. https://doi.org/10.1016/j.ijsolstr.2009.10.009

Hu, J., Zhang, K., Cheng, H., & Zou, P. (2020). Modeling on mechanical behavior and damage evolution of single-lap bolted composite interference-fit joints under thermal effects. *Chinese Journal of Aeronautics*. https://doi.org/10.1016/j.cja.2020.09.023

Hu, J., Zhang, K., Xu, Y., Cheng, H., Xu, G., & Li, H. (2019). Modeling on bearing behavior and damage evolution of single-lap bolted composite interference-fit joints. *Composite Structures*, *212*, 452-464. https://doi.org/10.1016/j.compstruct.2019.01.044

Hu, J., Zhang, K., Yang, Q., Cheng, H., Liu, P., & Yang, Y. (2018). An experimental study on mechanical response of single-lap bolted CFRP composite interference-fit joints. *Composite Structures*, *196*, 76-88. https://doi.org/10.1016/j.compstruct.2018.05.016

Hu, X., Haris, A., Ridha, M., Tan, V., & Tay, T. (2018). Progressive failure of bolted single-lap joints of woven fibre-reinforced composites. *Composite Structures, 189*, 443-454. https://doi.org/10.1016/j.compstruct.2018.01.104

Huang, S., Fu, Q., Yan, L., & Kasal, B. (2021). Characterization of Interfacial Properties between Fibre and Polymer Matrix in Composite Materials - A Critical Review. *Journal of Materials Research and Technology*. https://doi.org/10.1016/j.jmrt.2021.05.076

Hühne, C., Zerbst, A. K., Kuhlmann, G., Steenbock, C., & Rolfes, R. (2010). Progressive damage analysis of composite bolted joints with liquid shim layers using constant and continuous degradation models. *Composite Structures*, *92*(2), 189-200. https://doi.org/10.1016/j.compstruct.2009.05.011

International Organization for Standardization. (2014). *(ISO Standard Metallic materials - Sheet and strip - Erichsen cupping test (ISO 20482:2013); German*

version EN ISO 20482:2013. American Society for Testing and Materials International. https://doi.org/10.31030/2081283

Ireman, T. (1998). Three-dimensional stress analysis of bolted single-lap composite joints. *Composite Structures, 43*(3), 195-216. https://doi.org/10.1016/S0263-8223(98)00103-2

Jasra, Y., Singhal, S., Upman, R., & Saxena, R. K. (2020). Finite element simulation of stress corrosion cracking in austenitic stainless steel using modified Lemaitre damage model. *Materials Today: Proceedings*, *26*, 2314-2322. https://doi.org/10.1016/j.matpr.2020.02.499

Jiang, H., Zeng, C., Li, G., & Cui, J. (2021). Effect of locking mode on mechanical properties and failure behavior of CFRP/Al electromagnetic riveted joint. *Composite Structures, 257*, 113162. https://doi.org/10.1016/j.compstruct.2020.113162

Khashaba, U. A., Sallam, H. E. M., Al-Shorbagy, A. E., & Seif, M. A. (2006). Effect of washer size and tightening torque on the performance of bolted joints in composite structures. *Composite Structures, 73*(3), 310-317. https://doi.org/10.1016/j.compstruct.2005.02.004

Lambiase, F. (2015). Mechanical behaviour of polymer–metal hybrid joints produced by clinching using different tools. *Materials & Design*, *87*, 606-618. https://doi.org/10.1016/j.matdes.2015.08.037

Lambiase, F., & Ko, D.-C. (2017). Two-steps clinching of aluminum and Carbon Fiber Reinforced Polymer sheets. *Composite Structures, 164*, 180-188. https://doi.org/10.1016/j.compstruct.2016.12.072

Lee, C.-S., Kim, J.-H., Kim, S.-k., Ryu, D.-M., & Lee, J.-M. (2015). Initial and progressive failure analyses for composite laminates using Puck failure criterion and damage-coupled finite element method. *Composite Structures, 121*, 406-419. https://doi.org/10.1016/j.compstruct.2014.11.011

Lennon, R., Pedreschi, R., & Sinha, B. P. (1999). Comparative study of some mechanical connections in cold formed steel. *Construction and Building Materials, 13*(3), 109-116. https://doi.org/10.1016/S0950-0618(99)00018-5

Lian, J., Feng, Y., & Münstermann, S. (2014). A Modified Lemaitre Damage Model Phenomenologically Accounting for the Lode Angle Effect on Ductile Fracture. *Procedia Materials Science, 3,* 1841-1847. https://doi.org/10.1016/j.mspro.2014.06.297

Liu, Y., Zhang, L., Liu, W., & Wang, P. C. (2013). Single-sided piercing riveting for adhesive bonding in vehicle body assembly. *Journal of Manufacturing Systems, 32*(3), 498-504. https://doi.org/10.1016/j.jmsy.2013.04.005

Li, J., Li, Y., Zhang, K., Liu, P., & Zou, P. (2015). Interface damage behaviour during interference-fit bolt installation process for CFRP/Ti alloy joining structure. *Fatigue & Fracture of Engineering Materials & Structures, 38*(11), 1359-1371. https://doi.org/10.1111/ffe.12313

Liu, Y., & Zhuang, W. (2019). Self-piercing riveted-bonded hybrid joining of carbon fibre reinforced polymers and aluminium alloy sheets. *Thin-Walled Structures, 144*, 106340. https://doi.org/10.1016/j.tws.2019.106340

Liu, Y., Li, M., Lu, X., Li, Q., & Zhu, X. (2021). Pull-out performance and optimization of a novel Interference-fit rivet for composite joints. *Composite Structures, 269*, 114041. https://doi.org/10.1016/j.compstruct.2021.114041

Mayer, M. H., & Gaul, L. (2007). Segment-to-segment contact elements for modelling joint interfaces in finite element analysis. *21*(2), 724-734. https://doi.org/10.1016/j.ymssp.2005.10.006

McCarthy, C., & McCarthy, M. (2020). 12 - Design and failure analysis of composite bolted joints for aerospace composites. (P. Irving, & C. Soutis, Eds.) *Polymer Composites in the Aerospace Industry (Second Edition)*, 331-369. https://doi.org/10.1016/B978-0-08-102679-3.00012-5

McCarthy, C., McCarthy, M., Stanley, W., & Lawlor, V. (2005). Experiences with Modeling Friction in Composite Bolted Joints. *Journal of Composite Materials, 39*(21), 1881-1908. https://doi.org/10.1177/002199830505180

McCarthy, C., O'Higgins, R., & Frizzell, R. (2010). A cubic spline implementation of non-linear shear behaviour in three-dimensional progressive damage models for composite laminates. *Composite Structures, 92*(1), 173-181. https://doi.org/10.1016/j.compstruct.2009.07.025

McCarthy, M., Lawlor, V., Stanley, W., & McCarthy, C. (2002). Bolt-hole clearance effects and strength criteria in single-bolt, single-lap, composite bolted joints. *Composites Science and Technology, 62*(10-11), 1415-1431. https://doi.org/10.1016/S0266-3538(02)00088-X

McCarthy, M., McCarthy, C., Lawlor, V., & Stanley, W. (2005). Three-dimensional finite element analysis of single-bolt, single-lap composite bolted joints: part I—model development and validation. *Composite Structures, 71*(2), 140-158. https://doi.org/10.1016/j.compstruct.2004.09.024

Min, J., Li, Y., Carlson, B. E., Hu, S. J., Li, J., & Lin, J. (2015). A new single-sided blind riveting method for joining dissimilar materials. *CIRP Annals - Manufacturing Technology, 64*(1), 13-16. https://doi.org/10.1016/j.cirp.2015.04.047

Mucha, J., KaŠČÁK, L., & SpiŠÁK, E. (2011). Joining the car-body sheets using clinching process with various thickness and mechanical property arrangements. *Archives of Civil and Mechanical Engineering, 11*(1), 135-148. https://doi.org/10.1016/S1644-9665(12)60179-4

Nerilli, F., & Vairo, G. (2017). Progressive damage in composite bolted joints via a computational micromechanical approach. *Composites Part B: Engineering, 111*, 357-371. https://doi.org/10.1016/j.compositesb.2016.11.056

Neugebauer, R., Todtermuschke, M., Mauermann, R., & Riedel, F. (2008). Overview on the state of development and the application potential of dieless mechanical

joining processes. *Archives of Civil and Mechanical Engineering*, *8*(4), 51-60. https://doi.org/10.1016/S1644-9665(12)60121-6

Nong, N., Keju, O., Yu, Z., Zhiyuan, Q., Changcheng, T., & Feipeng, L. (2003). Research on press joining technology for automotive metallic sheets. *Journal of Materials Processing Technology*, *137*(1–3), 159-163. https://doi.org/10.1016/S0924-0136(02)01083-X

Noroozi, S., Sewell, P., & Vinney, J. (2014). Investigation of Bolt Group Configurations on Load Distribution and Joint Failure. *Mechanics of Advanced Materials and Structures*, *21*(5), 422-432. https://doi.org/10.1080/15376494.2012.697604

Olmedo, Á., & Santiuste, C. (2012). On the prediction of bolted single-lap composite joints. *Composite Structures*, *94*(6), 2110-2117. https://doi.org/10.1016/j.compstruct.2012.01.016

Olmedo, A., Santiuste, C., & Barbero, E. (2014). An analytical model for the secondary bending prediction in single-lap composite bolted-joints. *Composite Structures, 111*, 354-361. https://doi.org/10.1016/j.compstruct.2014.01.015

Oudjene, M., & Ben-Ayed, L. (2008). On the parametrical study of clinch joining of metallic sheets using the Taguchi method. *Engineering Structures*, *30*(6), 1782-1788. https://doi.org/10.1016/j.engstruct.2007.10.017

Oudjene, M., Ben-Ayed, L., Delamézière, A., & Batoz, J. (2009). Shape optimization of clinching tools using the response surface methodology with Moving Least-Square approximation. *Journal of Materials Processing Technology*, *209*(1), 289-296. https://doi.org/10.1016/j.jmatprotec.2008.02.030

Qiu, C., Guan, Z., & Du, S. (2022). An improved characteristic length method for predicting the single bolt joint bearing strength considering secondary bending effect. *Mechanics of Advanced Materials and Structures*, *29*(10), 1405-1417. https://doi.org/10.1080/15376494.2020.1821265

Panicaud, B., Saanouni, K., Baczmański, A., François, M., Cauvin, L., & Le Joncour, L. (2011). Theoretical modelling of ductile damage in duplex stainless steels – Comparison between two micro-mechanical elasto-plastic approaches. *Computational Materials Science, 50*(6), 1908-1916. https://doi.org/10.1016/j.commatsci.2011.01.038

Pommier, H., Busso, E. P., Morgeneyer, T. F., & Pineau, A. (2017). Local approach to stress relaxation cracking in a AISI 316L-type austenitic stainless steel: Tomography damage quantification and FE simulations. *Engineering Fracture Mechanics, 183*, 170-179. https://doi.org/10.1016/j.engfracmech.2017.03.050

Porcaro, R., Hanssen, A. G., Langseth, M., & Aalberg, A. (2006). Self-piercing riveting process: An experimental and numerical investigation. *Journal of Materials Processing Technology, 171*(1), 10-20. https://doi.org/10.1016/j.jmatprotec.2005.05.048

Ranjan, P., & Pandey, A. (2021). Modeling of pinning phenomenon in Iwan model for bolted joint. *Tribology International, 161*, 107071. https://doi.org/10.1016/j.triboint.2021.107071

Rao, Z., Ou, L., Wang, Y., & Wang, P.-C. (2020). A self-piercing-through riveting method for joining of discontinuous carbon fiber reinforced nylon 6 composite. *Composite Structures, 237*, 111841. https://doi.org/10.1016/j.compstruct.2019.111841

Rice, J. R., & Tracey, D. M. (1969). On the ductile enlargement of voids in triaxial stress fields∗. *Journal of the Mechanics and Physics of Solids, 17*(3), 201-217. https://doi.org/10.1016/0022-5096(69)90033-7

Rispler, A. R., Tong, L., P. Steven, G., & Wisnom, M. R. (2000). Shape optimisation of adhesive fillets. *International Journal of Adhesion and Adhesives, 20*(3), 221-231. https://doi.org/10.1016/S0143-7496(99)00047-0

Roux, E., & Bouchard, P. O. (2013). Kriging metamodel global optimization of clinching joining processes accounting for ductile damage. *Journal of Materials*

Processing Technology, *213*(7), 1038-1047. https://doi.org/10.1016/j.jmatprotec.2013.01.018

Sajid, Z., Karuppanan, S., Sallih, N., Kee, K., & Shah, S. (2021). Role of washer size in mitigating adverse effects of bolt-hole clearance in a single-lap, single-bolt basalt composite joint. *Composite Structures*, *266*, 113802. https://doi.org/10.1016/j.compstruct.2021.113802

Software, M. (2020). Marc Volume B: Element Library. MSC MARC Corporation.

Song, D., Li, Y., Zhang, K., Cheng, H., Liu, P., & Hu, J. (2016). Micromechanical analysis for microscopic damage initiation in fiber/epoxy composite during interference-fit pin installation. *Materials & Design*, *89*, 36-49. https://doi.org/10.1016/j.matdes.2015.09.118

Song, D., Li, Y., Zhang, K., Liu, P., Cheng, H., & Wu, T. (2015). Stress distribution modeling for interference-fit area of each individual layer around composite laminates joint. *Composites Part B: Engineering*, *78*, 469-479. https://doi.org/10.1016/j.compositesb.2015.04.013

Stoughton, T. B., & Yoon, J. W. (2011). A new approach for failure criterion for sheet metals. *International Journal of Plasticity*, *27*(3), 440-459. https://doi.org/10.1016/j.ijplas.2010.07.004

Subramonian, S., Altan, T., Ciocirlan, B., & Campbell, C. (2013). Optimum selection of variable punch-die clearance to improve tool life in blanking non-symmetric shapes. *International Journal of Machine Tools and Manufacture*, *75*, 63-71. https://doi.org/10.1016/j.ijmachtools.2013.09.004

Sun, X., & Khaleel, M. A. (2005). Performance Optimization of Self-Piercing Rivets Through Analytical Rivet Strength Estimation. *Journal of Manufacturing Processes*, *7*(1), 83-93. https://doi.org/http://dx.doi.org/10.1016/S1526-6125(05)70085-2

Tay, T. E., Liu, G., Tan, V. B. C., Sun, X. S., & Pham, D. C. (2008). Progressive Failure Analysis of Composites. *Journal of Composite Materials, 42*(18), 1921-1966. https://doi.org/10.1177/0021998308093912

Ueda, M., Miyake, S., Hasegawa, H., & Hirano, Y. (2012). Instantaneous mechanical fastening of quasi-isotropic CFRP laminates by a self-piercing rivet. *Composite Structures, 94*(11), 3388-3393. https://doi.org/10.1016/j.compstruct.2012.04.027

Varis, J. P., & Lepistö, J. (2003). A simple testing-based procedure and simulation of the clinching process using finite element analysis for establishing clinching parameters. *Thin-Walled Structures, 41*(8), 691-709. https://doi.org/10.1016/S0263-8231(03)00026-0

Virupaksha, V., & Nassar, S. (2008). Effect of Washers and Bolt Tension on the Behavior of Double-Lap S2-Glass Fabric Epoxy Composite Joints. *ASME 2008 Pressure Vessels and Piping Conference*, 607-616. https://doi.org/10.1115/PVP2008-61727

Wang, J., Yu, Y., Fu, C., Xiao, H., Wang, H., & Zheng, X. (2020). Experimental investigation of clinching CFRP/aluminum alloy sheet with prepreg sandwich structure. *Journal of Materials Processing Technology, 277*, 116422. https://doi.org/10.1016/j.jmatprotec.2019.116422

Wei, J., Jiao, G., Jia, P., & Huang, T. (2013). The effect of interference fit size on the fatigue life of bolted joints in composite laminates. *Composites Part B: Engineering, 53*, 62-68. https://doi.org/10.1016/j.compositesb.2013.04.048

Wu, T., Zhang, K., Cheng, H., Liu, P., Song, D., & Li, Y. (2016). Analytical modeling for stress distribution around interference fit holes on pinned composite plates under tensile load. *Composites Part B: Engineering, 100*, 176-185. https://doi.org/10.1016/j.compositesb.2016.06.011

Xu, G., Cheng, H., Zhang, K., Liang, B., Cheng, Y., Hu, J., & Liu, C. (2020). Modeling of damage behavior of carbon fiber reinforced plastic composites interference bolting with sleeve. *Materials & Design, 194*, 108904. https://doi.org/10.1016/j.matdes.2020.108904

Xu, G., Zhang, K., Cheng, H., Luo, B., Liang, B., Cheng, Y., & Li, H. (2022). An experimental study on mechanical behavior and failure mechanism of sleeved fasteners and conventional bolt for composite interference-fit joints. *Thin-Walled Structures, 170*, 108537. https://doi.org/10.1016/j.tws.2021.108537

Yang, Y., Bao, Y., Wang, J., & Du, F. (2022). Extended spring–mass method for joint stiffness prediction of single-lap multi-bolt composite joints considering assembly gap and gap shimming. *Mechanics of Advanced Materials and Structures, 29*(27), 5911-5922. https://doi.org/10.1080/15376494.2021.1968551

Yang, Y., Wang, Y.-Q., Liu, X., Gao, H., & Bao, Y. (2019). The effect of shimming material on flexural behavior for composite joints with assembly gap. *Composite Structures, 209*, 375-382. https://doi.org/10.1016/j.compstruct.2018.10.086

Zhang, J., Liu, F., Zhao, L., Chen, Y., & Fei, B. (2014). A progressive damage analysis based characteristic length method for multi-bolt composite joints. *Composite Structures, 108*, 915-923. https://doi.org/10.1016/j.compstruct.2013.10.026

Zhang, Z., Xiao, Y., Xie, Y., & Su, Z. (2019). Effects of contact between rough surfaces on the dynamic responses of bolted composite joints: Multiscale modeling and numerical simulation. *Composite Structures, 211*, 13-23. https://doi.org/10.1016/j.compstruct.2018.12.019

Zuo, Y., Cao, Z., Zheng, G., & Zhang, Q. (2020). Damage behavior investigation of CFRP/Ti bolted joint during interference fit bolt dynamic installation progress. *Engineering Failure Analysis, 111*, 104454. https://doi.org/10.1016/j.engfailanal.2020.104454